THE UNIVERSITY OF
SYDNEY

CONTACT AND NON-CONTACT NON-DESTRUCTIVE DETECTION OF DEBONDING OF TILES

Yu ZHAO

Supervisor: Li Chang, Qing Li

A thesis submitted in fulfilment of the requirements for the degree of
Doctor of Philosophy

School of Aerospace, Mechanical and Mechatronic Engineering Faculty of
Engineering
The University of Sydney

April 2026

Declaration

I declare the work present in this thesis was original and the best of my knowledge for fulfilling the requirement of degree of Doctor of Philosophy at the University of Sydney. The work has not been submitted for any degree at any institution.

Abstract

Debonding of tiles in high-rise buildings has become an increasingly critical issue due to rapid urbanisation. Falling tiles pose a safety threat to pedestrians, vehicles, and other equipment. Reliable non-destructive inspection (NDI) methods are essential for detecting debonding. This study systematically investigates both contact and non-contact acoustic NDI methods for inspecting tile debonding or loose fixings. It elaborates on the mechanisms of these acoustic inspection methods and outlines the step-by-step procedures for defect detection. The study also provides valuable algorithms for developing efficient inspection procedures that can be more easily applied in practice, such as identifying loose slot wedges in the stator of a hydropower generator.

After a brief review of recent developments in non-destructive inspection (NDI) methods for detecting structural defects, the thesis begins by investigating tile debonding on walls using non-contact acoustic inspection method to improve inspection efficiency and safety. This part of the study establishes a non-contact acoustic approach that utilises a directional sound source and a Laser Doppler Vibrometer (LDV) to inspect the debonding areas. An effective numerical model is integrated into the study to simulate the acoustic interaction between the sound waves and the tile. Tiles with typical debonding patterns are characterised and analysed using this method. A full-field numerical model is then employed to simulate and reconstruct the vibration signals generated by the tile. In both experimental and numerical setups, a directional sound source generates acoustic waves across a sweeping frequency band. Vibration signals at multiple inspection points on the tile surface are recorded and processed, with the vibration amplitudes at the resonance frequency of debonding conditions being specifically noted. The debonding area is identified by plotting the out-of-surface velocity map based on the vibration amplitudes. The numerical simulations align well with the experimental results, confirming the accuracy of the method. These findings demonstrate that debonding areas of varying shapes beneath the tile can be

clearly identified, proving the effectiveness of the proposed non-contact acoustic approach.

To further enhance the inspection efficiency of the non-contact acoustic approach, a deep learning (DL) network method is proposed. Signals from individual inspection points are processed using continuous wavelet transform (CWT), which converts them into time-frequency scalograms. A database is then created containing the characteristic signatures extracted from these scalograms. This study establishes and trains two DL networks using these signatures for all inspection points in the database. The first DL network is designed to classify debonding types based on predefined geometries, while the second DL network further evaluates the bonding conditions to support more specific debonding analysis. The results show that a single time-frequency scalogram, collected from a random inspection point, can achieve 100% classification accuracy with the first DL network. The second DL network can effectively identify the unknown debonding shape of a tile, with errors ranging from 1% to 31% for most typical cases. This two-stage method, utilising both DL networks, provides a fast and effective solution for tile debonding detection, offering a novel approach for engineering applications.

Then, the non-contact acoustic approach is extended to inspect the fixation condition of slot wedges within a hydropower generator. During long-term operation of a hydropower station, the loosening of any slot wedge within the generator can pose significant risks to its safe operation. In this study, typical engineering slot wedge components are examined and classified into three conditions: loose, intermediate, and normal, based on assessments by an experienced technician, as commonly practised in the field. A directional sound source generates an acoustic wave with a sweeping frequency band, which propagates to the slot wedges. The vibration signals induced on the surface of the slot wedges by the acoustic waves are collected and processed. The fixation conditions of the slot wedges are determined by analysing the frequency peaks within the frequency band of 900–2100 Hz. The classification results demonstrate that the identification accuracy for both the loose and normal fixation conditions is 100%. With the help of a DL network, the identification accuracy for all three conditions reaches 100%. Compared to traditional contact-based inspection methods, this non-contact acoustic approach offers the advantage of a shorter operation time, while maintaining accuracy that is comparable to conventional techniques.

Finally, a contact inspection method is applied to detect the tile debonding. Tile debonding is detected by analysing vibration signals triggered by the impact force, where a hammer excites the tile and a microphone captures the vibro-acoustic signals, mimicking human hearing. The study finds that the debonded and undebonded areas of the tile produce different acoustic waveforms when activated. Accordingly, a method is developed to differentiate the debonded and normal conditions, enabling precise identification of the debonding area. A data processing approach based on Fast Fourier Transform (FFT) is applied to identify resonance frequencies. Bonding conditions are determined using frequency band signatures, and the debonded area is identified through an algorithm based on the Digital Damage Fingerprints (DDF) method. Compared to traditional methods that rely on the trained ears of experienced workers, this approach eliminates human subjectivity, yielding more reliable assessment results.

Acknowledgements

It is not only a milestone of my twenty-year journey for study, but also a new beginning in the lifelong study of engineering. This is the genuine feeling that has resonated strongly in my heart at present as the summary of my experience during my PhD journey.

First and foremost, I would like to express my most profound gratitude to my former supervisor, Professor Lin Ye, and my current supervisor, Dr. Li Chang. Their patient guidance, intellectual inspiration, and unwavering support have been fundamental to the completion of this thesis. They not only rigorously corrected my research mistakes and guided my academic direction but also broadened my horizons consistently. More importantly, during the times when I struggled emotionally, their kindness and wisdom helped me regain my strength and focus. This thesis would have been far more difficult without their dedication.

I would also like to give my sincere thanks to Dr. Yuan Chen, who taught me the foundation of scientific research: attention to detail, patience to study, and pursuing every question until the truth is revealed. His influence has profoundly shaped my approach to challenges in both research and beyond.

My sincere thanks go to my senior colleagues, Dr. Xiaoyu Cui and Dr. Andy Wang, for their immense assistance during my experimental work. Their expertise and willingness to help were invaluable.

I would also like to extend my gratitude to my dear friends—Zhi Han, Xiaochong Wang, Feihong Lu, Wei Li, Xiaobo Sun, Yafei Xu, and others—for their encouragement and companionship through difficult times. Their belief in me gave me the motivation to keep moving forward.

I owe my gratitude to the University of Sydney. This research reported in this thesis was supported by the award of a Faculty of Engineering Research Scholarship to the PhD Candidate.

Most deeply, I owe everything to my family. Their endless love, understanding, and emotional support were my anchor during moments of despair. Their presence carried me through the lowest points and enabled me to complete this dissertation.

Finally, I dedicate this work to the memory of my beloved grandmother, who passed away during the writing of this thesis. I will forever cherish her love and carry her spirit with me.

Statement of originality

This is to certify that the content of this thesis is my own work. This thesis has not been submitted for any other degree or purpose.

I certify that the intellectual content of this thesis is the product of my own work, and that all assistance received in preparing this thesis and all sources have been acknowledged.

Yu Zhao
03/10/2025

Authorship attribution statement

Chapter 3 & 4 of this thesis has been published as [**Y. Zhao**, Y. Chen, and L. Ye, A non-contact inspection method of tile debonding using tuned acoustic wave and laser doppler vibrometer. Journal of Sound and Vibration, 2023. 564: p. 117875. DOI: https://doi.org/10.1016/j.jsv.2023.117875]. I designed the study, obtained the experimental and numerical results and wrote the drafts of the manuscript.

This thesis contains material previously published in [**Y. Zhao**, Y. Chen, and L. Ye, A non-contact inspection method of tile debonding using tuned acoustic wave and laser doppler vibrometer, in the 17th International Conference on Engineering Structural Integrity Assessment, in conjunction with, the 2023 International Symposium on Structural Integrity (ESIA17/ISSI2023) International Conference. 2023: Manchester, United Kingdom, 23rd May-25th May 2023]. This material comprises section 3.1. I designed the study, obtained the experimental results and wrote the drafts of the manuscript.

In addition to the authorship attribution statements above, in cases where I am not the corresponding author of a published item, permission to include the published material has been granted by the corresponding author.

Yu Zhao

03/10/2025

As supervisor for the candidature upon which this thesis is based, I can confirm that the authorship attribution statements above are correct.

Chang Li

03/10/2025

Statement regarding the use of generative AI

During the preparation of the thesis, the author used DeepSeek for the purposes of text enhancement. The use of this generative AI tool includes sentence structure and spelling. The author confirms that where text was modified by generative AI, the content was reviewed for possible errors, inaccuracies, and bias. The author takes full responsibility for the submitted thesis and ensures the work is their own and has used generative AI within the parameters of use (refer to the University of Sydney generative AI guide for researchers).

Yu Zhao

29/9/2025

Content

Symbols and Abbreviations

a	Scale factor (CWT); Constant (Energy calculation)
A	Cross-sectional area
A_0	Initial cross-sectional area
AMP_i	Amplitude of short-term energy
b	Translational factor (CWT)
B	Fitness function; Isentropic bulk modulus
c	Sound speed in a medium
C_ζ	Admissibility constant (CWT)
d	Bias value in a neural network
Det	Threshold for signal detection
E	Young's Modulus (Elastic Modulus)
EEF_i	Energy Entropy Ratio
EL_i	Short-term energy (Logarithmic)
f	Frequency
$f(t)$	Signal in the time domain
f_0	Original resonance frequency
f_n	Resonance frequency with added mass
H_i	Short-term spectral entropy
h	Thickness
m	Mass
Δm	Added mass (e.g., of a sensor)
n	Sample index
N	Number of samples/signals
p	Sound pressure

p_0	Reference sound pressure in air
$p_i(k)$	Spectral probability density function
$S(\omega)$	Power Spectral Density
$S^{mt}(\omega)$	Multi-Window Spectral Estimate
t	Time
T	Temperature; Period
T_i^{l-1}	i-th activated neuron value in layer l-1
v	Wave velocity; Output vector in a neural network
w	Displacement
W	Amplitude coefficient for displacement
$x(n)$	Discrete-time signal
$X(k)$	Frequency-domain sequence (DFT/FFT)
$X(a,b)$	Continuous Wavelet Transform
$Y_i(k)$	Discrete Fourier transform result of a framed signal
Δf	Resonance frequency shift
$\zeta(t)$	Mother wavelet function
$\theta(x),\phi(y)$	Characteristic beam functions
λ	Wavelength
ρ	Density
σ	Poisson's ratio
ω	Angular frequency ($\omega=2\pi f\omega=2\pi f$)
ω_{ij}	Connection weight in a neural network

ANN	Artificial Neural Network
CWT	Continuous Wavelet Transform
DDF	Digital Damage Fingerprints
DL	Deep Learning

DOF	Degree of Freedom
FC	Fully Connected
FEA/FEM	Finite Element Analysis/Finite Element Method
FFT	Fast Fourier Transform
FRP	Fiber-Reinforced Polymer
GPR	Ground-Penetrating Radar
GWO	Grey Wolf Optimisation
HGU	Hydropower Generation Unit
IE	Impact-Echo
IR	Impact-Response
LDV	Laser Doppler Vibrometer
LU	Laser Ultrasonics
MLP	Multi-Layer Perceptron
MTNB	Multitone Burst
MWSE	Multi-Window Spectral Estimation
NDI/NDT	Non-Destructive Inspection/ Non-Destructive Testing
NN	Neural Network
PI	Polyimide
PZT	Piezoelectric Transducer
ReLU	Rectified Linear Unit
RP	Reference Point
SCR	Stable Continental Region
SLDV	Scanning Laser Doppler Vibrometer
SNR	Signal-to-Noise Ratio
SPL	Sound Pressure Level
SVM	Support Vector Machine

TPS	Thermal Protection System
UAV	Unmanned Aerial Vehicle
WT	Wavelet Transform

Publications

The work directly from this thesis:

Journal

1. **Y. Zhao**, Y. Chen, and L. Ye, A non-contact inspection method of tile debonding using tuned acoustic wave and laser doppler vibrometer. Journal of Sound and Vibration, 2023. **564**: p. 117875. DOI: https://doi.org/10.1016/j.jsv.2023.117875.
2. **Y. Zhao**, Y. Chen, L. Ye, L. Chang, Fast non-contact inspection of tile debonding using deep learning network with tuned acoustic wave signals. To be submitted to Structural Health Monitoring.
3. **Y. Zhao**, Y. Chen, X. Xie, L. Ye, L. Chang, A non-contact inspection method for detecting stator tightness of hydro power station. To be submitted to Journal of Mechanical Sciences.

Conference paper

1. **Y. Zhao**, Y. Chen, and L. Ye, A non-contact inspection method of tile debonding using tuned acoustic wave and laser doppler vibrometer, in the 17th International Conference on Engineering Structural Integrity Assessment, in conjunction with, the 2023 International Symposium on Structural Integrity (ESIA17/ISSI2023) International Conference. 2023: Manchester, United Kingdom, 23rd May-25th May 2023

The work outside of this thesis:

Journal article

1. Y. Deng, **Y. Zhao**, B. Wan, L. Chang, Effects of re-entrant auxetic structure on friction-induced vibrational behaviour of 3D printed PLA in sliding wear process. Friction, 2025. DOI: https://doi.org/10.26599/FRICT.2025.9441172.

List of Figures

List of Tables

Chapter 1: Introduction

The acoustic inspection method has gained widespread interests for defect detection due to its advantages, such as high safety, portability, and short operational time. This chapter begins with an introduction to the inspection objectives, followed by an explanation of the importance of detecting tile debonding. A comparative analysis of conventional non-destructive inspection (NDI) techniques is then provided, highlighting the benefits and limitations of each. The chapter concludes with an overview of the thesis, outlining the key topics discussed in subsequent chapters.

1.1 Background

In recent decades, the pace of urbanisation has rapidly accelerated. It is projected that by 2050, approximately 70% of the global population will reside in cities [1]. As urbanisation progresses, countless tall buildings have been constructed, many of which have stood for several decades. Over time, these buildings show signs of aging, including damage to glass, paint, and tiles. This wear and tear on these structures increases the risk of objects falling from these structures, posing a growing threat to public safety. Even at moderate heights, falling objects can present serious hazards to people below [2]. For example, the impact energy of a 250-gram object falling from a height of 30 meters could potentially be fatal [3]. In New South Wales alone, over 15,500 injuries have been reported due to falling objects since 2016, resulting in 17 deaths and 200 permanent disabilities [4]. One of the key factors contributing to this risk is the deterioration of the adhesive layer between building decorations, such as tiles, and the walls they cover. Over time, this can compromise the integrity of the structure [5, 6]. Ceramic tiles, long valued for their durability and practicality, have been a common choice for building facades [7]. Porcelain tiles, in particular, became popular in Italy in the late 1970s [8], and since then, they have been widely used for both decorative and protective purposes on building exteriors [9, 10]. Not only do tiles enhance the aesthetic appeal of buildings [11, 12], but their low water absorption also helps prevent humidity-related erosion, making them ideal for facade applications [13]. A notable example is the Sydney Opera House, whose iconic gleaming exterior is covered with approximately 1.4 million tiles [14]. Exposed to the sea winds of Sydney Harbour, these tiles face constant environmental stress. If tile debonding goes undetected, the safety of the thousands of tourists who visit could be at risk.

Figure 1.1 Over 1,400,000 tiles on the Sydney Opera House [14]

The material components of modern ceramic tiles primarily consist of clays and fluxes [15]. The clays can be categorised into various types, such as red-firing clay, white-firing clay (ball clay), and kaolin [16, 17]. The manufacturing process for these tiles is typically divided into two categories: wet and dry routes [16]. A detailed discussion of the manufacturing procedure is beyond the scope of this thesis. Regardless of the manufacturing method used, tiles that meet the required quality standards are designed to be durable and long-lasting. Tiles are typically affixed to concrete substrates in buildings using adhesives, with mortar being the most commonly used adhesive in construction. Compared to the tile itself, mortar is relatively fragile. Previous studies have shown that the weakest point in the tile-adhesive-substrate system is the tile-adhesive interface [18-20]. Various factors can contribute to defects at this interface, with wear and tear, earthquakes, and strong winds being the primary causes of adhesive failure [2, 21].

Regarding seismic activity, Australia is classified as a stable continental region (SCR), with relatively low seismic activity compared to other parts of the world [22]. The likelihood of large, surface-rupturing earthquakes in Australia is minimal, and earthquake-induced defects are typically insignificant [23]. While earthquakes are not a major concern, strong winds can still pose a risk, potentially leading to tiles detaching and falling. According to the Australian Standard AS 4055:2021, which outlines wind load requirements for housing, all buildings in Australia must be capable of withstanding winds with a gust speed of up to 187 km/h (Category N3), which corresponds to non-cyclonic winds [24-27]. Additionally, several studies have reported a global decline in wind speeds over the past few decades, primarily due to atmospheric changes driven by climate change [28-30]. Consequently, non-damaged tiles are generally resilient to the winds typically encountered in Australia.

The primary focus of this study is the wear-and-tear-related defects in tiles. The tiling system in buildings can be simplified as a multilayer structure consisting of the tile, adhesive mortar, and the concrete substrate. Each of these layers has distinct material properties, meaning they respond differently to environmental factors such as humidity and temperature changes. This mismatch in physical properties leads to differential deformation, resulting in internal stresses. These stresses concentrate at the interfaces between the layers, causing initial cracks and erosions [31-33]. Over decades of exposure to environmental stress, delamination can occur between the tiles and the substrate, ultimately leading to tile debonding and detachment, as illustrated in Figure 1.2. Wear-and-tear-induced defects also weaken the bond between the tiles and the substrate, making it easier for external forces, such as wind, to dislodge the tiles.

Figure 1.2 Tiles fall off from an old residential building [34]

Therefore, to prevent tile debonding, it is essential to conduct regular inspections and maintenance, especially for tiles on tall buildings. This thesis primarily focuses on the detection of tile debonding, employing methods based on various physical principles to accurately determine the shape and location of the debonding. Traditional inspection methods often rely on the experience of skilled operators. For instance, experienced workers can identify defects by analysing the appearance and the sound produced when tapping the tiles. However, this method lacks the ability to quantify the defects, and its reliability can be influenced by environmental factors and human error. To minimise potential damage during inspections, non-destructive inspection (NDI) techniques are typically used. Numerous NDI methods have been developed, based on different principles, including mechanical, chemical, electrical, physical, and visual techniques [35, 36]. NDI methods can be further categorised into two main types: contact inspection and non-contact inspection, depending on the deployment approach. This study aims to explore both contact and non-contact inspection techniques for evaluating tiles on buildings. New approaches for capturing defect signals, along with corresponding data processing methods, are systematically proposed and evaluated. Ultimately, this thesis offers valuable insights into tile debonding detection, with the potential for broader applications.

1.2 Overview of this thesis

The primary objective of this study is to systematically investigate appropriate non-destructive inspection (NDI) methods for detecting tile debonding or loose fixation. The specific goals of the study are as follows:

1. Establish a non-contact acoustic inspection approach for accurately detecting tile debonding on walls, using a directional sound source and a Laser Doppler Vibrometer (LDV).
2. Develop an effective numerical model to simulate the acoustic interaction within the tiling system.
3. Build a defect database and establish a deep learning network to enhance the efficiency of the non-contact acoustic inspection method.
4. Expand the non-contact acoustic inspection approach to assess the fixation condition of slot wedges in a hydropower generator.

5. Develop a contact inspection method that analyses vibration signals activated by impact. An impact hammer is used to excite the tile, and a microphone collects the vibro-acoustic signals, mimicking the human ear’s ability to detect sound.

The following chapters outline the methodologies and findings related to these goals.

Chapter 2 provides a brief overview of recent advancements in non-destructive inspection methods, focusing on both contact and non-contact techniques. It also discusses the physical principles, data processing algorithms, and machine learning applications used in NDI methods.

Chapter 3 describes an experimental study of a non-contact acoustic method using acoustic excitation. Here, tiles with typical debonding areas are analysed. A directional sound source generates a multitone burst (MTNB) acoustic wave, and the vibro-acoustic signals at different points on the tile surface are captured using a Laser Doppler Vibrometer (LDV). These signals are processed to create a debonding map, represented by the out-of-surface velocity at each inspection point, which characterises the debonded areas.

Chapter 4 develops an effective numerical model to simulate the non-contact acoustic method described in Chapter 3. It includes an in-depth analysis of the acoustic interaction with the tiling system. The chapter also discusses the data processing of vibration signals collected from multiple inspection points and how the debonding areas are reconstructed from these signals. A detailed comparison between numerical simulations and experimental results is provided, with a focus on model accuracy.

Chapter 5 introduces a deep learning network designed to improve the efficiency of the non-contact acoustic method. Vibration signals from each inspection point are processed using continuous wavelet transform (CWT) and converted into time-frequency scalograms. A database of labelled and categorised scalograms is created, and two deep learning networks are trained with this data. The first network identifies debonding types based on predefined geometries, while the second network evaluates bonding conditions for more specific debonding assessments. The two-stage deep learning method shows high classification accuracy, enabling quick and effective identification of tile debonding.

Chapter 6 extends the application of the non-contact acoustic method to inspect the fixation condition of slot wedges within a hydropower generator. Loose slot wedges can pose significant safety risks to the operation of the generator. This chapter classifies typical slot wedge components into three categories: loose, middle, and normal. Vibration signals from the slot wedge surface are analysed to determine the fixation condition. Compared to traditional contact inspection methods, the non-contact acoustic approach offers faster inspection times while maintaining comparable accuracy.

Chapter 7 presents a contact acoustic approach using mechanical excitation. In this approach, an impact hammer excites the tile, and a microphone records the vibro-acoustic signals. These signals are collected from various inspection points, processed, and analysed to differentiate between normal and debonded areas, allowing for the identification of the bonding condition and debonding location.

Chapter 8 concludes the systematic study presented in this thesis, summarising key findings and offering suggestions for future research directions.

Chapter 2: Overview on non-destructive inspection using acoustic technologies

This chapter provides an overview of non-destructive inspection (NDI) technologies, with a particular focus on acoustic inspection methods. It highlights key challenges associated with this specific NDI approach. First, the physical principles and mechanisms underlying various NDI technologies are summarised. Following this, the chapter reviews the development of acoustic inspection over the past few decades, detailing significant advancements in the field. It then categorises and analyses both contact and non-contact acoustic inspection methods. Efforts aimed at enhancing inspection accuracy and efficiency are discussed, with a particular emphasis on signal processing techniques for acoustic signals. The chapter also outlines potential future directions for research and emphasises the promising outlook for acoustic inspection technologies. Finally, it summarises the challenges and limitations faced by current NDI methods, stressing the need for advanced acoustic inspection solutions to address the detection of tile debonding in building structures.

2.1 Non-destructive inspection (NDI)

Non-destructive inspection (NDI) technology is widely employed for on-site evaluations, enabling the detection of defects without causing any damage to the structure. NDI uses advanced methodologies and instruments to assess defects in terms of their types, shapes, locations, quantities, and specifications, both inside and on the surface of structures [37-39].

The minimum achievable resolution of an NDI method is determined by the dominant wavelength, λ [40]. In a discontinuous medium, the resolution of the NDI technique is typically λ/2 [40, 41]. The relationship between wave velocity v, wave frequency f, and wavelength λ is given by the following equation:

$$v = \lambda \times f \tag{2.1}$$

Since the wave velocity v is typically considered constant within a given medium, a shorter wavelength λ corresponds to a higher frequency f. However, as frequency increases, so does the attenuation of the signal [42, 43]. In practice, selecting the dominant signal involves a trade-off between accuracy and signal attenuation. Over the years, a variety of techniques utilising different dominant signals have been applied to NDI, including mechanical, physical, electrical, chemical, and even visual inspection methods [35, 36]. Each of these techniques comes with its own set of advantages and limitations.

Commercially available NDI equipment, such as impact hammers and ground-penetrating radar, are effective but limited in their ability to inspect specimens from long distances [44-46]. Computer vision and visual quality inspection provide intuitive surface-level inspection, but these methods are restricted to detecting cracks and surface damage [47, 48]. Radiographic techniques, including gamma-ray and X-ray inspection, can identify defects deep within materials, but exposure to radiation without proper safety measures poses significant health risks to workers. As a result, specialised vehicles and facilities are necessary for the transport and storage of radiographic equipment [39, 40]. Active thermography is widely used for inspecting low-thermal-conductivity materials. However, the large heating systems or solar heat required for this method limit its all-weather operational capability in field-based inspections [49-51]. The existence of shadow also limits its usage. Acoustic methods, utilising sonic or ultrasonic waves, detect defects by analysing the reflection or transmission of mechanical stress waves through the material [40, 45]. Compared to other NDI methods, acoustic techniques offer the distinct advantage of being able to detect defects within the material itself, while maintaining higher safety levels and significantly shorter operation times. This combination of benefits makes acoustic methods particularly well-suited for field-based inspections.

2.2 Development of acoustic inspection

NDI inspection methods can be generally classified into two categories: contact inspection and non-contact inspection [52]. Contact inspection requires direct physical contact between the probe and the specimen. This method typically involves using adhesives to secure the probe to the surface, and in some cases, even drilling holes into the structure [5, 40, 41, 53, 54]. Contact methods help minimise the interaction between air and the solid material, thus reducing signal attenuation and providing higher accuracy. These methods generally analyse changes in the structural response, such as mode shape variations, natural frequency, stiffness, and other modal characteristics [55-57]. However, in most studies, the contact inspection equipment is fixed on the specimen surface, which results in a relatively longer operation time[40, 54]. In contrast, non-contact inspection methods involve remote excitation, offering quicker deployment and the ability to maintain a safer working environment, especially in field settings [58-60]. Non-contact inspection is highly efficient and reduces the risk to workers. However, compared to contact-based methods, non-contact techniques typically suffer from greater signal attenuation, which can negatively impact the accuracy of the inspection.

Acoustic inspection systems can be either contact or non-contact methods. Depending on the relative positioning of the actuator and sensor, acoustic methods can be categorised into three transmission modes: direct transmission mode (also known as pitch and catch), semi-direct transmission mode, and indirect transmission mode (also known as pulse and echo) [40, 61, 62]. These modes are illustrated in Figure 2.1.

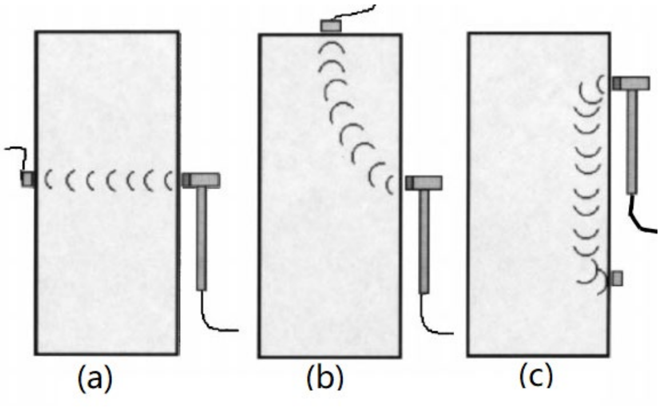

Figure 2.1 Three transmission modes of acoustic method: (a) direct; (b) semi-direct; (c) indirect [40]

The direct transmission mode cannot accurately locate the exact position and extent of a defect, as it records the average wave velocity along the entire path. Therefore, it is typically used for simple evaluations, such as assessing the relative condition of the structure or estimating internal stress [63, 64]. In contrast, the semi-direct and indirect transmission modes are capable of determining the precise location and extent of the defect. As a result, these modes are commonly used in commercial acoustic inspection equipment [61]. In all three modes, the actuator and sensor can either be attached to the surface of the specimen or positioned at a distance, depending on the specific application scenario.

2.2.1 Contact methods

After decades of development, contact methods are now capable of determining the position and size of defects with suitable resolution [44-46]. The traditional actuators used in contact acoustic methods are varied and include sound probes, piezoelectric transducers (PZT), ground-penetrating radar (GPR), and, most commonly, the impact hammer [65, 66]. As mentioned earlier, the semi-direct and indirect transmission modes are widely employed in commercial equipment. In these modes, the actuator and sensor can be integrated into a compact sound probe, providing excellent portability—this configuration is known as the pulse-and-echo system [44, 67]. Depending on the scanning orientation, ultrasonic data collected by sound probes can be classified into standard formats such as A-scan, B-scan, C-scan, and S-scan [67-69]. These formats can be displayed simultaneously in modern computerised ultrasonic scanning systems [70], which can even combine different scan formats to reconstruct a 3D model, as shown in Figure 2.2 [71].

Due to the small size and light weight of the sound probe, multiple probes can be deployed in various directions to improve resolution [72]. Mohammadkhani et al.[73] used an ultrasonic phased array probe to inspect aerospace composite structures. They applied a wavelet transform-based algorithm with a smart thresholding technique, using the extracted statistical mean and standard deviation of structural noise to determine the depth of defects. The depth signals gathered from different directions were then combined to generate a 3D model of the defects within the structure. Similarly, Blandford and David [74] recorded the vibration amplitude at each layer of a laminated composite structure using C-scan, creating defect profiles for each layer. These profiles were then combined to reconstruct a 3D model of the defect.

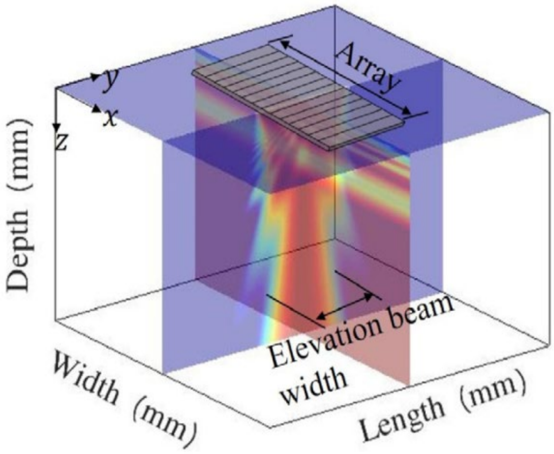

Figure 2.2 3D reconstruction of a specimen with different ultrasonic scan formats [71]

Another widely used commercial device is ground-penetrating radar (GPR), which also operates as a pulse-and-echo system. In this method, high-frequency electromagnetic pulses are emitted into the specimen, and the receiving antenna captures the reflected echoes from the selected region [58]. This technique is commonly referred to as the impulse radar method [75, 76]. Originally, GPR was primarily used by geophysicists for subsurface investigations [40]. However, when applied to structural inspection, the depth of inspection is relatively shallow, and higher signal attenuation is typically acceptable. To achieve better resolution in structural applications, the frequency of the GPR is set higher than in geophysical applications, which results in improved resolution at the cost of a shallower penetration depth.

The actuators mentioned earlier, such as sound probes, piezoelectric transducers (PZT), and ground-penetrating radar (GPR), can directly generate mechanical waves in the medium. In addition to these methods, mechanical waves can also be generated through external mechanical excitation. One of the oldest non-destructive inspection (NDI) methods in construction is the knocking technique, where a hammer is used to strike a specimen [77]. Experienced operators can assess the condition of a structure by recognising the sound produced during the knocking, which falls within the human hearing range (20 Hz - 20 kHz). A clear sound typically indicates a solid structure, while a muffled sound may suggest defects or voids. However, this method is subjective, and even seasoned operators can be influenced by surrounding noise.

Since the 1980s, the impact hammer has been widely used as an actuator for inspecting concrete elements [78, 79]. When using an impact hammer as an actuator, inspections can be classified into two methods: the impact-echo (IE) test method and the impact-response (IR) test method [59, 75]. The IE method uses a high-frequency, low-amplitude source, while the IR method uses a low-frequency, high-amplitude source. The IE method measures the frequency domain of the compression wave between the surface and any internal defects, whereas the IR method records the global deformation response of the structure. Both methods can be used to generate a two-dimensional grid of vibration responses to locate defects [80]. In a traditional contact inspection setup, an impact hammer is used as the excitation source, and accelerometers are deployed to record the vibration properties, as illustrated in Figure 2.3.

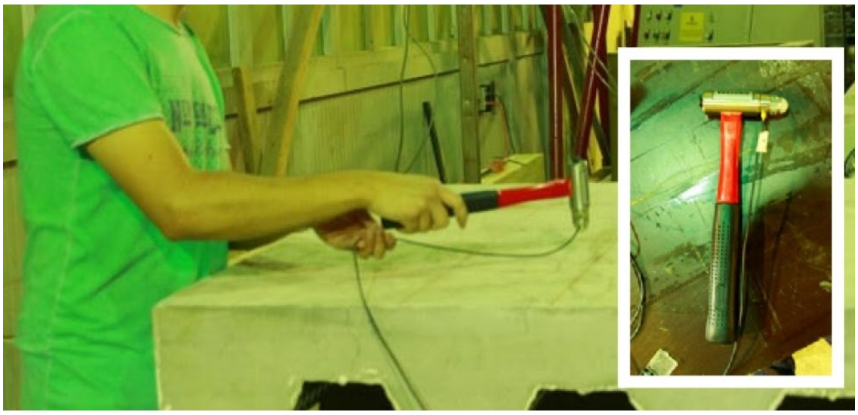

Figure 2.3 Concrete damage inspection by impact hammer [81]

Shukla and Koo [82] used forced vibration, generated by an impact hammer, to track changes in the net stiffness of a space shuttle’s Thermal Protection System (TPS) tiles in order to monitor structural integrity. While this method can detect changes in the structure, it cannot assess the severity of the damage or pinpoint the exact location of the defect. In contrast, Saadatmorad et al. [83] employed Pearson-based correlation coefficients to compare the mode shapes between intact and damaged steel beams, using one-dimensional discrete wavelet transform (1D-DWT). Their approach allows for the identification of the damage location within the beam.

However, the contact inspection method using an impact hammer has its limitations. This method typically involves an accelerometer to record the vibration signals. The deployment of the accelerometer introduces mass loading on the surface of the specimen. Although the accelerometer's mass is relatively small, it can cause a slight shift in the specimen's resonance frequency, especially for lightweight or highly damped materials, such as rubber [84]. Additionally, this added mass introduces some uncertainty in the estimation of the modal parameters. In a one-degree-of-freedom (DOF) system, the resonance shift Δf can be determined by:

$$\Delta f = f_0 - f_n, \qquad \frac{\Delta f}{f_0} = 1 - \sqrt{\frac{m}{m + \Delta m}} \tag{2.2}$$

where f_0 is the resonance frequency of the original specimen, f_n is the resonance frequency of the specimen with the attached accelerometer, m is the mass of the specimen, and Δm is the mass of the accelerometer. As shown in Equation (2.2), to correct for the resonance shift (Δf), all the masses in the system must be clearly measured, which makes the inspection process relatively simple in theory. However, in practice, the inspection system is often more complex than a one-degree-of-freedom (DOF) system, and measuring the mass of the structure can be challenging. To mitigate the impact of the mass, accelerometers are becoming smaller, and alternative sensors, along with corresponding data processing methods, are being developed. For instance, Xie et al. [85] designed an offline detection system to inspect slot wedge loosening in the stator of a hydropower generator. An inspection robot, equipped with an impact hammer, taps the wedge, and the looseness of the wedge is assessed by analysing the percussion sound signals. This method avoids the resonance shift caused by the accelerometer.

2.2.2 Non-contact methods

As mentioned earlier, contact inspection methods generally experience lower attenuation, but the deployment time for such systems is relatively long. Additionally, the mass of the accelerometer can affect the resonance frequency of the original system. To mitigate these uncertainties, non-contact methods have been developed. Common non-contact acoustic inspection techniques include laser ultrasonics (LU), air-coupled ultrasonic inspection, and the acoustic method using pressure waves in combination with a Laser Doppler Vibrometer (LDV) [84, 86, 87].

Laser ultrasonics (LU), including femtosecond and picosecond LU, utilises modulated lasers to induce ultrasound by irradiating the specimen, causing rapid thermal expansion [88] , as illustrated in Figure 2.4.

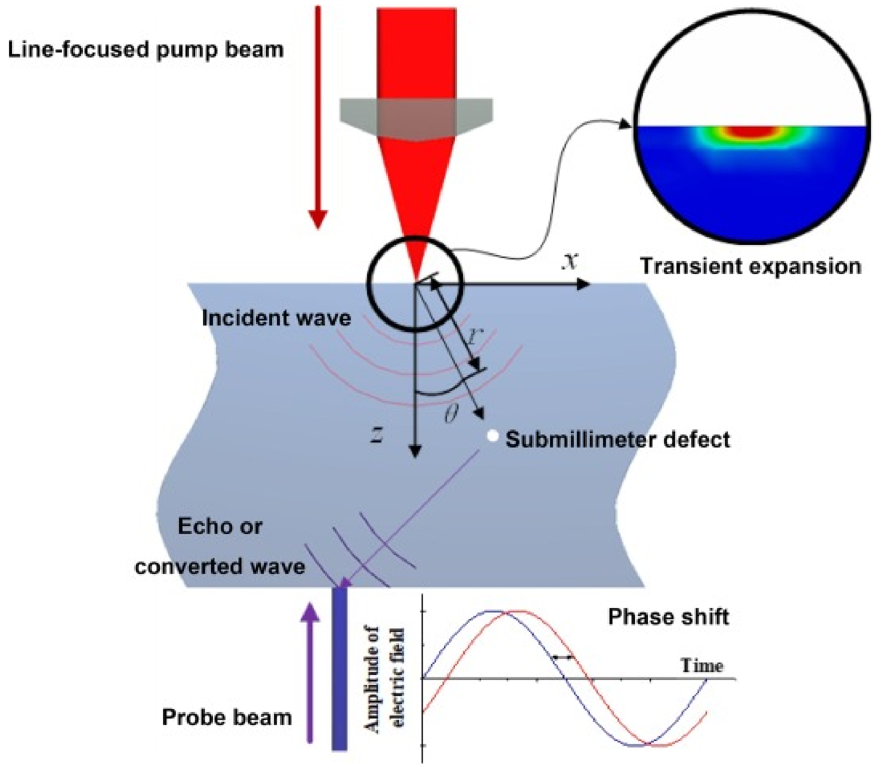

Figure 2.4 Schematic diagram of laser ultrasonic inspection [88]

The wavelength of the induced ultrasound in Laser Ultrasonics (LU) is ultrashort, making it a powerful NDI tool for detecting minor defects in small specimens, such as defects in integrated circuits (ICs) and cracks in metal boards or weld seams [89-92]. Additionally, the LU method can excite the specimen remotely, making it suitable for extreme environments such as high temperatures, high corrosion, and radiation exposure [93]. Masserey et al. [94] used a heterodyne laser interferometer to detect surface cracks with complex geometries. The interferometer measures the out-of-plane displacement of the surface generated by a laser beam. The time delay between cracked and non-cracked specimens is then calculated to characterise the crack’s shape, with good agreement achieved between the numerical model and experimental results. Hernandez-Valle et al. [95] used laser-based ultrasonic generation and detection of Rayleigh waves to measure surface defects with varied branched geometries. The geometry of the defect is characterised by analysing the reflection and transmission of ultrasonic surface waves. Zarubin [96] developed a refraction-corrected tomographic algorithm for immersion laser-ultrasonic imaging, resulting in reconstructed ultrasonic images with better resolution than those obtained through X-ray imaging. Pei et al. [97] developed a phased array laser ultrasonic testing system that uses a compact optical fiber array bundle and a laser interferometer to inspect inner cracks in thick metal specimens. Li et al. [98] analysed the interactions between laser-generated surface acoustic waves (SAWs) and different cracks, measuring crack depth using an optimised algorithm that selects key features from the transmission and reflection acoustic signals.

However, the LU method is more suited for inspecting small defects, typically at the millimeter or even micron level [86]. To avoid damaging the specimen, the laser energy must be kept below the ablation threshold, which results in weaker signals. Consequently, the inspection depth is also limited [88, 89]. As a result, the LU method is not ideal for tile inspection, where larger defects and deeper penetrations are typically encountered.

Air-coupled ultrasonic inspection is another widely used commercial NDI method. This technique does not require any coupling media, such as glue, grease, or water [99]. The probes used in air-coupled ultrasonic inspection typically consist of classical piezoelectric transducers with additional transitional layers and a critical final matching layer on the piezoelectric element to improve the transfer of acoustic energy in the air, or capacitive devices, which are vibrating membranes [100]. The primary limitations of this method are the reflection loss between air and solid media, as well as the attenuation of high-frequency ultrasound in air. Consequently, this method often requires two-sided access—such as through-transmission mode, guided wave mode, or Rayleigh wave mode— to gather sufficient signal amplitudes for accurate measurement [101-104] , as shown in Figure 2.5. In these modes, two or more capacitive film transducers operate as reciprocal devices, detecting waves transmitted through or reflected from the specimen. These modes also help reduce interface losses.

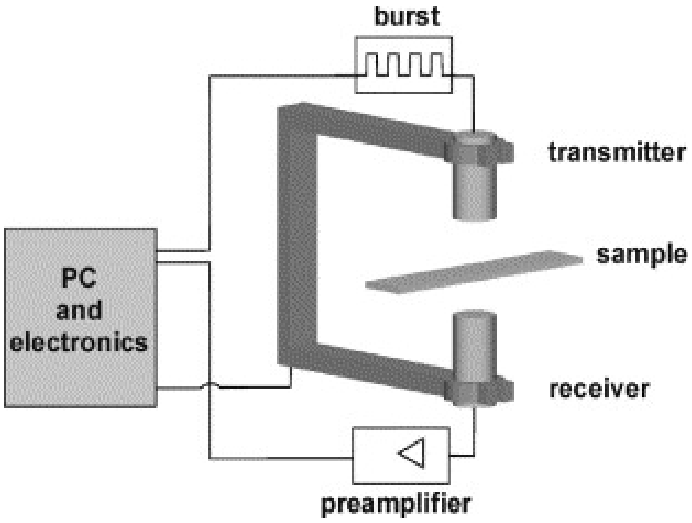

Figure 2.5 Through transmission mode of air-coupled ultrasonic inspection [104]

Römmeler et al. [105] utilised an air-coupled ultrasonic setup with Lamb wave mode conversion to detect and localise small defects in thin polymer plates. Their study demonstrated that mounting the transducer close to the surface is advantageous, as it increases the inspection window for Lamb wave detection and allows multiple reflections of the excitation pulse between the transmitter and the plate surface. Additionally, performing multiple measurements along the direction of Lamb wave propagation is crucial for thorough signal analysis and visualising mode conversion. Kažys et al. [106] proposed a one-sided access air-coupled ultrasonic measurement technique that successfully detected and visualised inhomogeneities in composite materials. In this method, both the transmitter and receiver are placed on the same side of the specimen. However, the technique is sensitive to specular reflections and edge waves, and the distance between the transducers must be kept short to maintain spatial resolution. Han et al. [107] optimised an air-coupled ultrasonic signal processing and imaging program based on time-frequency analysis, which can adaptively reconstruct the feature signal and effectively suppress noise interference. This approach offers a flexible and cost-effective solution for air-coupled ultrasonic inspection.

However, in practice, the use of air-coupled ultrasonic inspection is limited. As previously mentioned, air-coupled transducers are typically placed on both sides of the specimen to gather sufficient signal amplitude [87, 108]. However, the signal amplitude generated by air-coupled ultrasonic equipment is relatively low, leading to a low signal-to-noise ratio (SNR) [109]. Additionally, the multi-modal and dispersive response of the structure being inspected can also affect the ultrasonic guided wave generated by the equipment, making signal processing more complex [110]. The inspection results are further influenced by discontinuous media, making this method unsuitable for inspecting complex multilayer systems, such as the tile-adhesive-substrate system [111]. In these systems, extracting damage information becomes particularly challenging. Moreover, the distance between the air-coupled ultrasonic probe and the specimen must be limited to just a few centimetres [112-114] , and the method requires high-altitude operation when inspecting tiles on tall buildings due to the short inspection range.

Current studies have demonstrated that a relatively large area of defective specimens on concrete can be detected from a long distance using a small, directional acoustic transducer [60, 115]. Building on this, an acoustic method using pressure waves and a Laser Doppler Vibrometer (LDV) has been developed. In this method, the acoustic transducer generates a specific pressure wave to excite the tiles, while the LDV provides high spatial resolution measurements without physical contact with the specimen. This approach allows for the remote measurement of the specimen's vibration signals from distances of up to 30 meters [84].

Katakura et al. [116] analysed the influence of different defect sizes and depths using both impact hammer inspection and the acoustic method with pressure waves and LDV. Their study demonstrated that the acoustic method using pressure waves and

LDV provides comparable detection accuracy to impact hammer inspection. They also found that the resonance frequency of the defect was proportional to the defect's depth, while being inversely proportional to the square of the defect's diameter. Sugimoto et al. [117-119] developed an acoustic inspection system to inspect the debonding of large tiles on walls, using a directional sound speaker mounted on an unmanned aerial vehicle (UAV) alongside an LDV. The defects were identified by discriminating between the signal and noise produced by the resonance of the defective parts. This method successfully measured the sizes of predefined circular debonding areas. Nakagawa et al. [120] enhanced the accuracy of defect localisation by analysing signals gathered through the acoustic method using pressure waves and a scanning laser Doppler vibrometer (SLDV). They incorporated a resonance judgment process into the conventional time- and frequency-gating technique, improving the localisation accuracy.

However, current studies focus on regular shapes, such as circles. While the position and severity of the debonding area can be localized and measured, the profiles of these areas are not typically plotted. In real-world applications, debonding areas may have different geometries, and the sizes of the debonding tiles may be relatively small, requiring high resolution to accurately detail their profiles. Moreover, most of the current research has been based on experimental studies with limited numerical analysis [121].

2.3 Methods of signal processing for acoustic signals

In practice, the accuracy of the NDI technique may not be sufficient to identify the specific profile of the debonding area. Some NDI techniques may also require multiple inspection points, which reduces their efficiency [115, 117, 122]. An increase in the number of inspection points leads to a corresponding rise in the number of signals. Furthermore, signals collected by different techniques may contain noise and irrelevant data. Therefore, effective data processing approaches are crucial for improving the accuracy and efficiency of the NDI technique.

With the growth of computational power, machine learning has become integral to inspection data processing, result augmentation, and defect type classification [123-126]. In most cases, traditional algorithms cannot capture the underlying relationships. The goal of training a machine learning model is to achieve high-quality classification by identifying the connections between inputs and outputs [127, 128]. Through machine learning, computer systems can extract valuable information from example signals, enabling them to learn specific tasks and improve performance [129].

Machine learning has two main types of learning: supervised and unsupervised [129, 130]. In supervised learning, each sample signal is assigned a label, as illustrated in Figure 2.6. The label defines the outcome of the learning process, representing the true value. The two main types of supervised learning tasks are classification and regression. Classification aims to group samples into predefined classes, and the learned classifier is then used to predict the class of new samples. In contrast, regression predicts a numerical value rather than assigning samples to a specific class. For instance, regression could estimate weight based on features like shape, height, and width.

Unsupervised learning, on the other hand, does not require labeling. It focuses on identifying patterns in the sample signals without a predefined goal. Unsupervised learning is commonly used for preprocessing and understanding sample signals. In this study, both supervised and unsupervised learning techniques are employed.

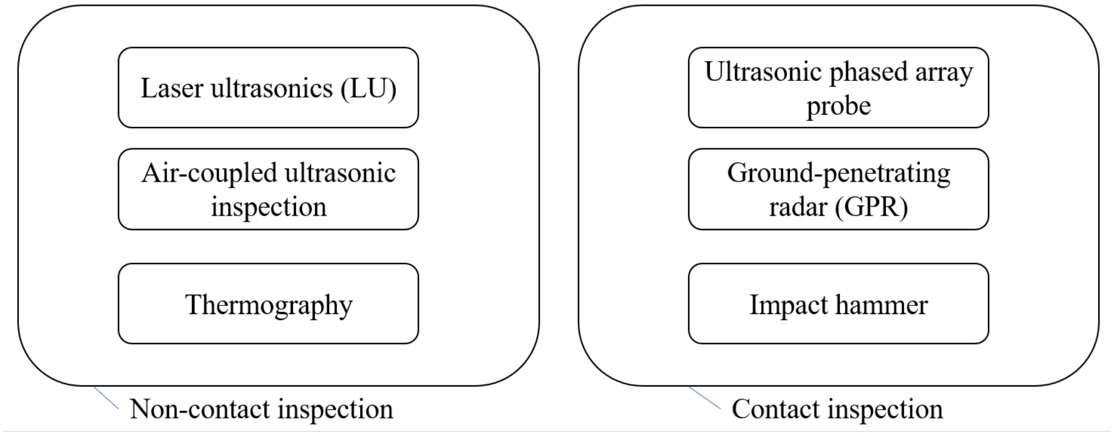

Figure 2.6 Label the NDI techniques by their contact type

Since the mid-1980s, machine learning has been applied to NDI (Non-Destructive Inspection) applications. Early efforts primarily focused on automated testing systems that used simple decision algorithms [131, 132]. Early machine learning algorithms, such as the perceptron, single-hidden-layer neural networks (NN), and support vector machines, significantly enhanced the effectiveness of NDI techniques [133-135]. Hornik [136, 137] demonstrated that multilayer feedforward networks, even with just a single hidden layer and sufficiently many hidden units, can serve as universal approximators when using arbitrary bounded and non-constant activation functions. A universal approximator can approximate any Borel-measurable function between finite-dimensional spaces with any desired level of accuracy. This theoretical result confirmed the practical feasibility of neural networks.

The perceptron is the simplest type of neural network and can be viewed as a basic classifier [138]. It produces a single output based on multiple inputs, where a linear transformation of the inputs (weighted by a set of input weights) determines the result. The perceptron performs a weighted sum of the DDD input features, along with an additional constant input, and then outputs "yes" or "no" based on whether the weighted sum exceeds a given threshold TTT [139]. The perceptron classifier separates data points in the feature space in a linear fashion. The DDD-dimensional feature space is divided into "yes" and "no" regions by a line, plane, or hyperplane, depending on the number of dimensions, which is determined by the perceptron classifier. The class CCC corresponds to the linear separation rule. In a neural network, the hidden layer is situated between the input layer and the output perceptron(s).

An input layer, hidden layers, and output layer combine into a common structure called Multi-Layer Perceptron (MLP), which is also known as the artificial neural network (ANN) [140-142]. An MLP with two hidden layers, an input layer, and an output layer is plotted in Figure 2.7 [143]. As shown in the figure, there are n input variables $X = \{x_1, x_2, \dots, x_n\}$ and m output variables $Y = \{y_1, y_2, \dots, y_n\}$ in the input layer and the output layer, respectively.

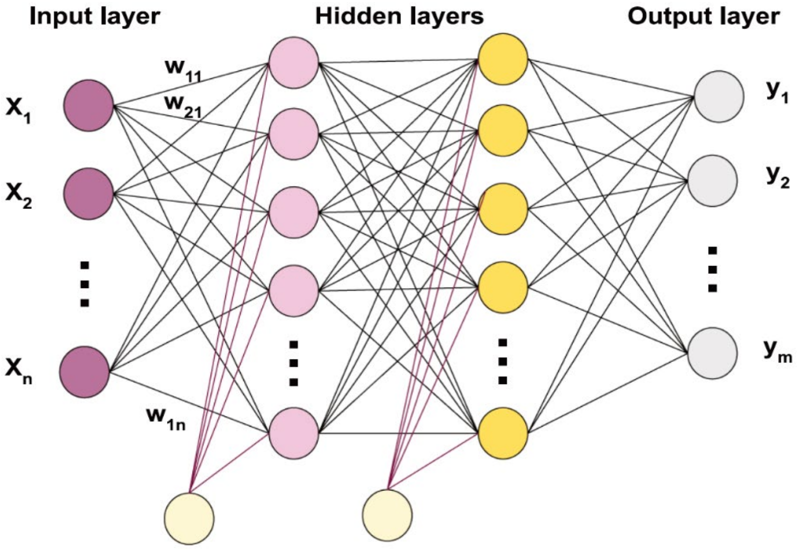

Figure 2.7 The structure of an ANN with two hidden layers [143]

The combination of hidden layers and non-linear activation functions allows artificial neural networks (ANNs) with this architecture to solve complex input-output mapping problems. The choice of neural architecture, including the number of hidden layers and neurons in each layer, is crucial for network design, particularly when identifying influential parameters [143, 144]. These parameters play a key role in shaping the structure of the ANN.

Support vector machines (SVMs) are considered one of the most effective techniques for optimizing expected solutions [145]. They are powerful and robust algorithms for both classification and regression, with applications across various fields [145]. The core principle of SVM is to use a hyperplane (or surface) that maximizes the margin between different classes in the training set, thereby enhancing the model's generalization ability.

With the advancement of computing power, numerous machine learning methods have been developed for defect detection, building upon early algorithms. As shown in Figure 2.8, modern machine learning can be divided into three main categories: supervised learning, unsupervised learning, and ensemble methods [146]. Supervised learning encompasses seven sub-categories: artificial neural networks (ANN), fuzzy logic, SVM, linear regression, decision trees, random forests, deep learning (DL), and optimization techniques, with a focus on genetic algorithms (GA). Ensemble learning methods include bagging, boosting, and ensemble fuzzy models. Unsupervised learning is further divided into self-organizing maps (SOMs) and clustering methods, which include principal component analysis (PCA), Gaussian mixture models (GMM), and K-means clustering.

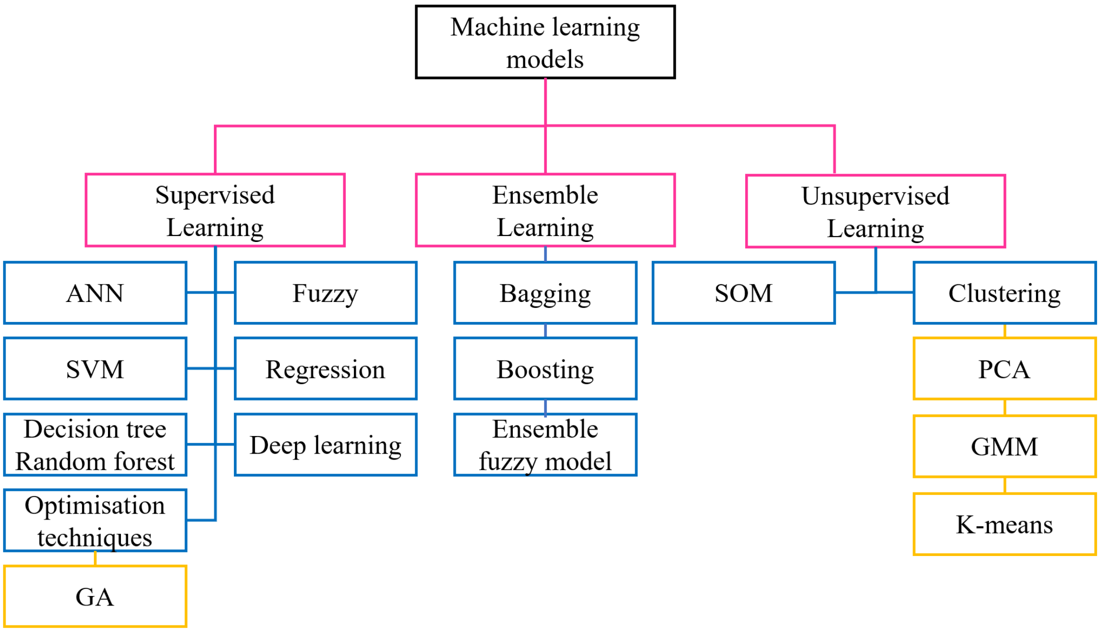

Figure 2.8 Working process of convolutional architecture [146]

In a study by Thobiani et al. [147], artificial neural networks (ANNs) were used to predict the length of cracks in a damaged plate. The ANN parameters were optimized using Grey Wolf Optimization (GWO) and an improved version of GWO, combined with Particle Swarm Optimization (PSO) (IGWO). Based on the mode shape-based damage index (MSDBDI) recorded at different inspection points, Ho et al. [148] determined the damage location in a bridge deck. Their study also analyzed changes in displacement mode shapes and frequency shifts at these points using an Antlion Optimizer artificial neural network (ALOANN) to assess the damage level. Finite element (FE) models were used to evaluate the accuracy of this two-step method. Czarnecki [149] trained an ANN using pull-off adhesion values obtained from five traditional NDI methods (optical method, three acoustic methods, and precise survey), alongside a pull-off method. His study demonstrated that a five-technique NDI method can match the accuracy of the destructive pull-off method when aided by an ANN.

Bonagura and Nobile [150] enhanced the SonReb method using ANN to measure compressive strengths. The SonReb method, an NDI technique that combines the rebound hammer and ultrasonic pulse velocity methods, can achieve the same accuracy as destructive core drilling tests with the aid of ANN. The Root Mean Square Error (RMSE) was only 0.00013 MPa. Minh et al. [151] addressed the structural damage identification (SDI) problem using a K-means Optimizer (KO). Barros et al. [152] developed a model-based decision tree algorithm to predict damage in a riveted steel truss bridge. A Finite Element (FE) model was created based on data gathered from Terrestrial Laser Scanning (TLS) and Ambient Vibration Testing (AVT), and nineteen potential damage cases were simulated. This calibrated FE model was used to train the decision tree algorithm, which proved to be an economically efficient and routine method for bridge inspection, capable of detecting and locating potential damage based on the bridge's actual modal characteristics. Prakash et al. [153] used water-coupled ultrasound scans, processed by a histogram of oriented gradients (HoG) and SVM, to analyze components of the A380 aircraft. Features, including the region area size and centroids of scan images, were extracted. As shown in Figure 2.9, Maximally Stable Extremal Regions (MSER) defects were highlighted in colored regions, defect sizes were circled with ellipses, and centroids were marked with black dots. The features were then analyzed using SVM, yielding good results and improving defect identification efficiency for A380 aircraft components.

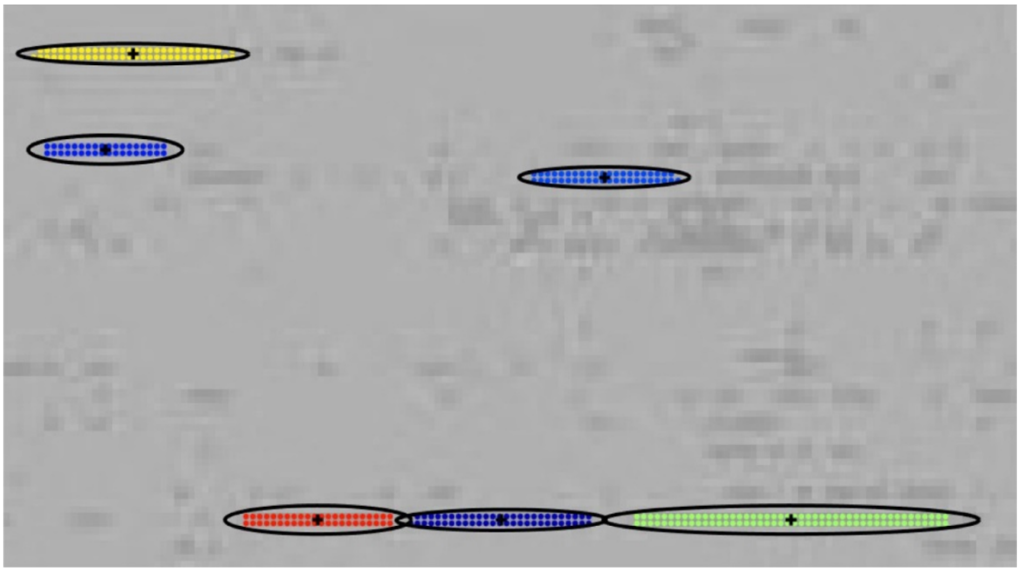

Figure 2.9 Feature extraction of ultrasonic scan [153]

However, in the supervised learning algorithms mentioned above, features within the signal were manually extracted and then imported into machine learning models for classification. This traditional feature extraction process largely depends on manually designed features, which limits their representational capabilities. As a result, it becomes challenging to capture more comprehensive semantic information, and the detection accuracy for complex scenes and targets may not be sufficient [154]. Additionally, the training effort required for this process may be limited. Ayman et al. [155] explored different feature-learning methods, incorporating both shallow and deep learning approaches for bearing prognostics. Shallow feature-learning methods can be further categorized into signal decomposition approaches and feature extraction techniques. Common signal decomposition methods include empirical mode decomposition (EMD), variational mode decomposition (VMD), and wavelet transform (WT). In contrast, deep learning (DL) algorithms can automatically capture the necessary features without manual intervention

The early attempts at deep learning (DL) were essentially based on traditional machine learning algorithms. In 2006, Hinton et al. [156] first proposed the principle of deep learning. The motivation behind this approach was to construct neural networks that simulate the human brain, enabling analytical learning. This method can also be applied to process various types of data, such as text, sound, and images. In 2014, Girshick et al. [157] developed the first deep learning algorithm for object detection, known as the Regions with CNN Features (R-CNN) method. Tao and Li [154] summarized the key differences between deep learning and traditional image defect detection methods in Table 2.1.

Table 2.1. Comparison of object detection algorithms: on traditional image processing and DL [154].

Object detection algorithm	Based on traditional image processing	Based on DL
Feature extraction methods	Manual design feature	Deep network
Detection proposal methods	Sliding window or Image pyramid	Proposal or Direct regression
Classification	Traditional classifier	Deep network
Training process	Multiple steps	End to end

As shown in Table 2.1, the advantages of the deep learning-based object detection method are as follows:

1. Hierarchical Feature Learning: DL algorithms, utilizing deep neural networks, can learn hierarchical features directly from the data. This allows higher-level features to be extracted from the original image. Compared to traditional

algorithms, deep learning offers better generalization and expressive capabilities, minimizing the impact of complex detection environments.

2. Efficiency and Accuracy: The use of proposal-based or direct regression methods in DL algorithms enhances efficiency. This approach also leads to higher detection accuracy, especially for complex objects with varying scales and postures.
3. Streamlined Training Process: Traditional methods often require a multi-step training process, whereas DL-based methods can streamline this by employing proposal or direct regression techniques to obtain object proposals.
4. Flexibility and Adaptability: Deep learning algorithms, with their deep networks for feature extraction and object detection, provide excellent flexibility and adaptability, making them more effective for handling diverse tasks.

Cai et al. [158] summarized the use of deep learning (DL) for defect identification in hydraulic structures. The DL-based image enhancement techniques they reviewed include Convolutional Neural Networks (CNNs), transformer architectures, and Generative Adversarial Networks (GANs). These algorithms were shown to effectively improve underwater imaging by reducing chromatic distortion, blurring, and low contrast.

Automatic feature extraction from the signal relies on convolutional architecture, which has the capacity to learn complex relationships among patterns extracted from raw data [155, 159]. This architecture was developed specifically to automatically gather features.

The convolutional architecture slides a predefined window across the feature map at each channel, extracting adjacent feature tiles at different positions. This process automatically gathers features using the learned weight matrix and convolution kernel, as shown in Figure 2.10 [160]. The resulting kernels are then filtered and reassembled into a new map that contains all the features from the raw images.

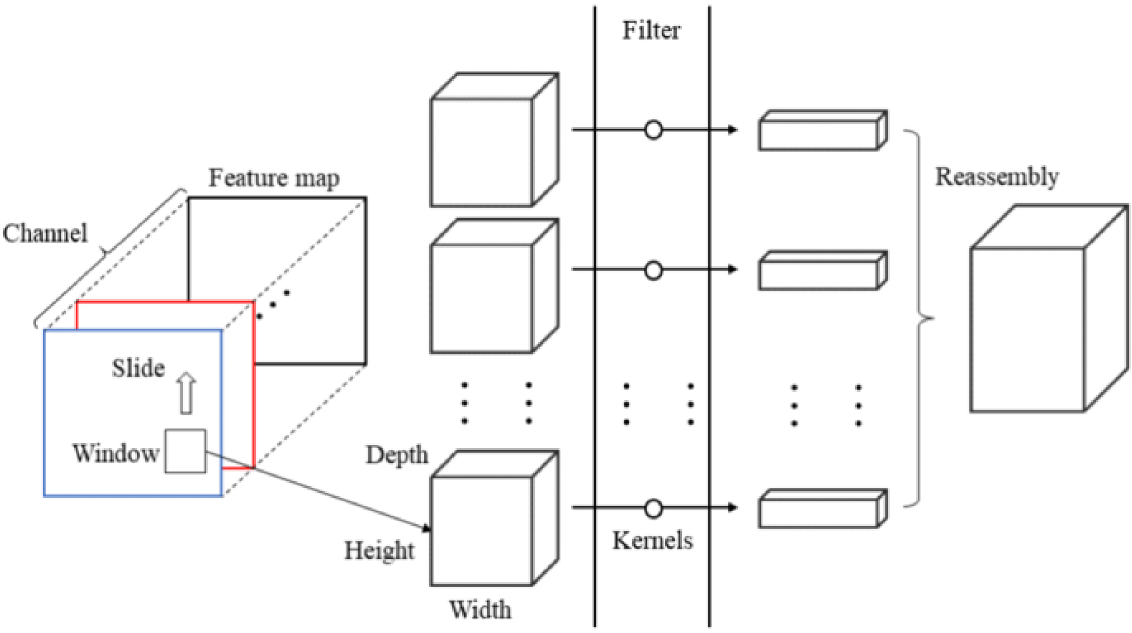

Figure 2.10 Working process of convolutional architecture [160]

Consider image classification as an example. The input image x at each layer in the CNN architecture has three dimensions: height, width, and depth. In practice, the height m is equal to the width, and the depth is also referred to as the number of channels r. For an RGB image, the depth r equals three, so the input dimensions are $m \times m \times r$. The kernels in each convolutional layer are denoted by k and also have three dimensions, which can be written as $n \times n \times q$ just like the input image. The n in the kernels is smaller than the input m, while the q is less than or equal to the input r. What’s more, the kernels are the foundation of the local connections. These kernels share similar parameters, including bias b^k and weight W^k. The kernels are convolved with the input to generate k feature maps h^k, with a size of m-n-1, as shown in Equation (2.3).

$$h^k = f(W^k * x + b^k) \tag{2.3}$$

As shown in Equation (2.3), the input and weights in the convolutional layer are computed using a dot product, similar to techniques in natural language processing (NLP). However, in convolutional layers, the inputs correspond to smaller regions of the initial image. After this, a nonlinearity, typically an activation function, is applied to the output of the convolutional layer.

Thanks to advancements in computer technology, more complex machine learning models based on convolutional architectures, such as CNNs and other deep learning algorithms like the spatial pyramid pooling (SPP) network, have been applied to image analysis [131, 161, 162]. These convolutional architectures can learn optimal features for the desired classification, eliminating the need for manual feature extraction. As a result, CNNs have become the most widely used type of deep learning network [163].

The CNN architecture is inspired by neurons in the human or animal brain, specifically simulating the structure of the visual cortex in a cat's brain [164]. It mimics the complex arrangement of cells in the visual cortex. The CNN offers three key benefits: parameter sharing, sparse interactions, and equivalent representations [163]. By employing shared weights and local connections, the CNN efficiently leverages the 2D structure of input data, such as image signals. Compared to conventional fully connected (FC) networks, CNNs use fewer parameters, simplifying the training process and accelerating network performance. Like the cells in the visual cortex, CNN neurons only sense small regions of the entire scene. Following this principle, the input is locally filtered, and the local correlations are extracted from the whole input.

Take an image classification CNN as an example; its architecture is shown in Figure 2.11. The system is used to classify different animal species.

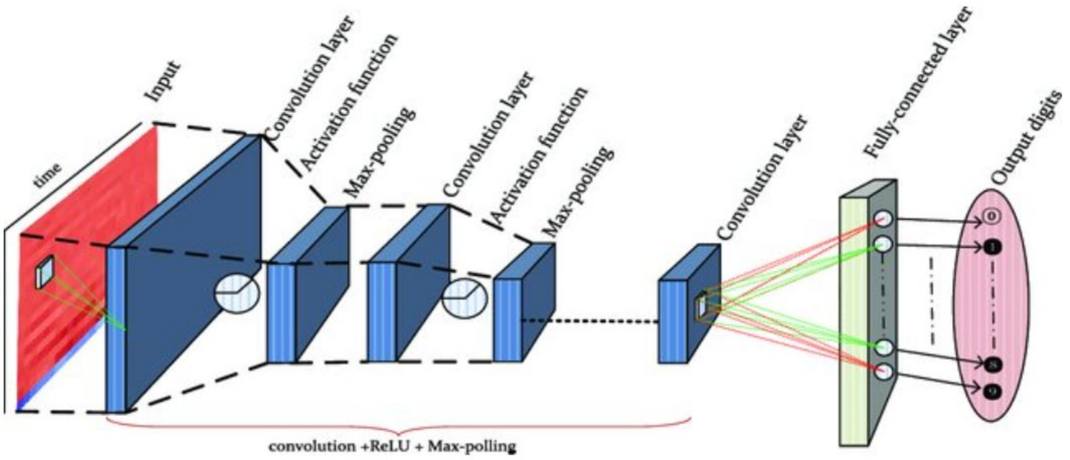

Figure 2.11 A CNN architecture for image classification [165]

As shown in Figure 2.11, the architecture of a commonly used CNN is similar to that of an ANN. It consists of multiple convolutional layers to extract features, which are then passed through a rectified linear unit (ReLU) layer to map the linear output from the convolutional layer to a non-linear one. Following this, sub-sampling (pooling) layers are used to down-sample each feature map, reducing the size of the data. This process decreases the time required for training and helps mitigate overfitting. In the pooling layer, functions such as max pooling or average pooling are typically applied which can be used to reduce the area to the size of the kernel (p × p). Finally, the last layers are fully connected (FC) layers that define the output size. These layers receive low-level and medium-level features and generate high-level abstract information, similar to the final layer in a typical neural network. The classification score is computed in the output layer, which can use methods such as a support vector machine (SVM) or a softmax function. For each instance, the probability of a specific class is represented by the corresponding score.

Many researchers have combined the DL network with NDI. Yuan et al. [166] developed a wide-band Lamb-wave-based active monitoring technology to inspect thin-walled composite structures. A neural network was adopted to analyse the collected signal and determine the damage mode. Sung et al. [167] monitored the impact damage within smart composite laminates by piezoelectric transducers. In their study, the wavelet transform (WT) was used to measure the features of the acoustic emission waves. A neural network was designed to analyse these features. Then the defects within the structure can be located, and the damage caused by the impact can be estimated. Similarly, Sikdar et al. [168] deployed a piezoelectric acoustic emission (AE) sensor network to monitor the influence of the impact on a composite panel. The continuous wavelet transform (CWT) is introduced in their study to extract features from the AE signal. Then, the damage source is classified by a trained DL network. Ma et al. [169] monitored the running state of a substation power transformer by analysing the AE signal generated by the operation of the transformer. Then, a CNN was used to identify the defective sound signal from the collected AE signal. Wang et al. [170] identified the bearing fault with the sound signal collected by the microphone. In this acoustical-based fault diagnosis method, acoustic images were generated by the collected sound signal, and then a CNN was trained to analyse the acoustic images and define the conditions of bearing fault. Ghafoor et al. [171] used non-contact laser ultrasonic technology to detect railhead defects. In their study, a CNN was built to classify railhead surface and subsurface flaws and ensure automatic detection.

Although the deep learning (DL) technique has proven to be an effective approach for NDI applications, research on inspecting tile debonding using DL is still limited. As discussed in Chapter 2.2, traditional NDI methods can identify the debonding status and position of building tiles, but their accuracy is insufficient for fully profiling the specific geometries of the debonding area [118]. While it is possible to improve the accuracy of traditional methods by increasing the number of inspection points, this approach is time-consuming and not practical for real-world engineering applications.

2.4 Summary of the challenges in NDI methods

This chapter provides an overview of the NDI technique, with a particular focus on the principles of inspections based on acoustic technologies and corresponding data processing methods, such as ANN and deep learning (DL). It then summarizes the key advancements made to address a major challenge in NDI technologies: the relatively low inspection accuracy, which limits the application of acoustic technologies in on-site inspections. After presenting the physical mechanisms and principles behind different NDI techniques, the chapter highlights the significant progress made in improving the effectiveness of acoustic inspection methods. Additionally, the efforts in signal processing aimed at enhancing both the accuracy and efficiency of NDI inspections are discussed, along with a summary of the commonly used machine learning techniques in NDI.

Generally speaking, the NDI method should provide three key pieces of information: whether the specimen is damaged, the location of the damage, and the profile of the damage. Despite the advancements discussed in Chapter 2, there remains a knowledge gap in understanding the accuracy-efficiency relationship of both contact and non-contact acoustic NDI techniques. This gap can be summarized in the following aspects:

1. Compared with NDI techniques based on other physical principles, the accuracy of the acoustic technique is not high enough to plot the profile of the debonding area.
2. As mentioned, the acoustic technique can define the debonding condition of the tiles, but due to the relatively low accuracy, the acoustic inspection requires multiple inspection points, resulting in a low accuracy.

3. Current machine learning methods cannot achieve an acceptable classification accuracy, and the features in the raw acoustic signal are not fully used.

Hence, this PhD thesis aims to explore both contact and non-contact inspection methods for building tiles, focusing on optimization measures to improve the accuracy and efficiency of acoustic inspections. This is achieved through detailed investigations of new signal gathering techniques and corresponding signal processing approaches, such as ANN and deep learning (DL). Additionally, the thesis provides systematic examinations and valuable insights into the inspection of building tile debonding and its extended applications.

Chapter 3: Experimental study of non-contact detection of tile debonding using acoustic excitation

As mentioned in Chapter 1, the falling tiles from high altitudes constantly threaten citizens. Regular inspection for tile debonding is essential to avoid tile falls. The non-contact method can avoid working at height, ensuring the workers' safety. The non-contact acoustic method utilised in this chapter uses a directional sound speaker to generate a sound wave and excite the tile specimen, then uses a laser Doppler vibrometer (LDV) to record the signal at each inspection point.

3.1 Principle of inspection based on acoustic excitation

The principle of this inspection method is similar to the contact inspection method. If the specimen is "knocked", the different bonding conditions will result in different responses. As a non-contact inspection method, a directional acoustic transducer is used as a sound source and an LDV is employed to record the vibration signal. At a point on a surface, the sketch-up of this method is summarised in Figure 3.1. The tile is attached to the concrete wall via a tile construction adhesive. Some part of the adhesive layer is removed to simulate the debonding area. The distance between the sound source and the tile is 1 m. When the pressure wave generated by the sound source reaches the surface of the tile, the vibration signal of the tile is excited, which can be detected and recorded via the LDV equipment.

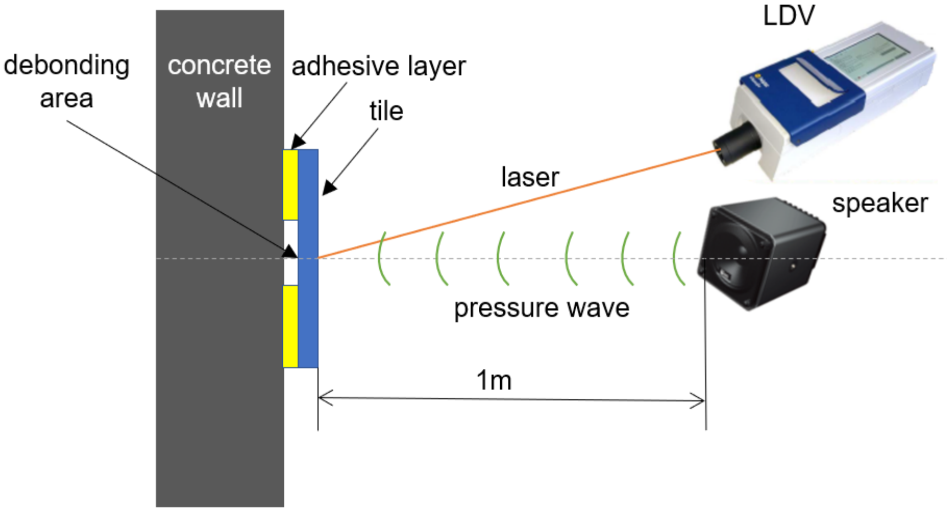

Figure 3.1 Setup of the acoustic inspection method used in this work

When the adhesive layer between the tile and wall is damaged, debonding occurs. The resulting cavity exists in the adhesive layer and weakens the bending rigidity, resulting in a different flexural vibration behaviour. In the debonding area, even a weak excitation can generate a relatively large vibration amplitude, and the resonance frequency of this area also changes. Based on these differences, this method can be used to analyse the vibration induced by acoustic irradiation and then identify a cavity within the adhesive layer, which means detecting the debonding areas.

In practice, the flexural resonance frequency of the debonding area is unknown. Therefore, the exciting signal should include a corresponding frequency band to actuate resonance. As a result, the exciting signal is selected as a multitone burst (MTNB) wave to reduce the inspection time [115, 117] This signal is widely used in high-speed measurement [117]. Using the MTNB signal, the sweep signal can be divided into sub-intervals, where the significant signal with a large magnitude of resonance can be easily captured, i.e., when the frequency moves close to the resonance frequency, the magnitude significantly increases. Then, the resonance frequency can be clearly identified after using the Fast Fourier Transform (FFT) in the large amplitude interval. The waveform of the signal is shown in Figure 3.2. The frequency range of the signal is 400~4200 Hz which can cover the first mode of the resonance frequency. As shown in Figure 3.2, the frequency range of this signal is 400~4200Hz. The frequency modulation interval is 200Hz, corresponding to 20 different frequencies. These frequencies are labelled as f1 to f20. The signal contains four pulses, and each pulse contains five frequencies. The first five frequencies are in the first pulse, with the last five frequencies in the second pulse. The length of each pulse is 3ms. The time interval between each pulse is 50ms. When the frequency is close to the resonance frequency, the amplitude of the vibration will be more significant.

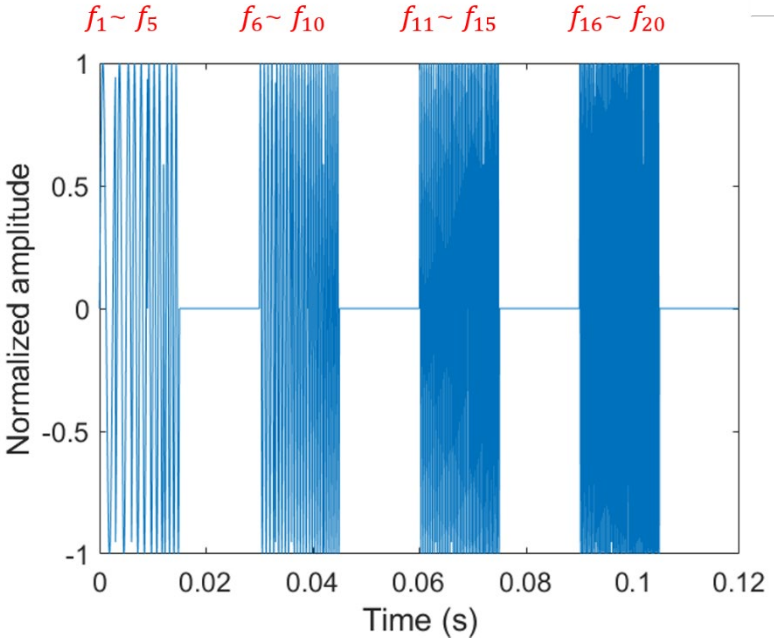

Figure 3.2 Waveform of an MTNB signal

The velocity at each inspection point can be collected by LDV equipment. This equipment measures the velocity component along the laser line of sight, as shown in Figure 3.3. In practice, the vibration velocity may not occur in the same direction as the laser line. As a result, the angle between the normal line of the surface and the laser beam will generate velocity components along the laser beam. Then, uncertainty will also appear in the result, especially for the in-plane velocity [84]. In this study, the velocity of the vibration is out-of-plane. Therefore, the uncertainty can be corrected by a cosine correction. Therefore, the angle between the LDV equipment and the normal line of the surface measured will not influence the measurement result in this study.

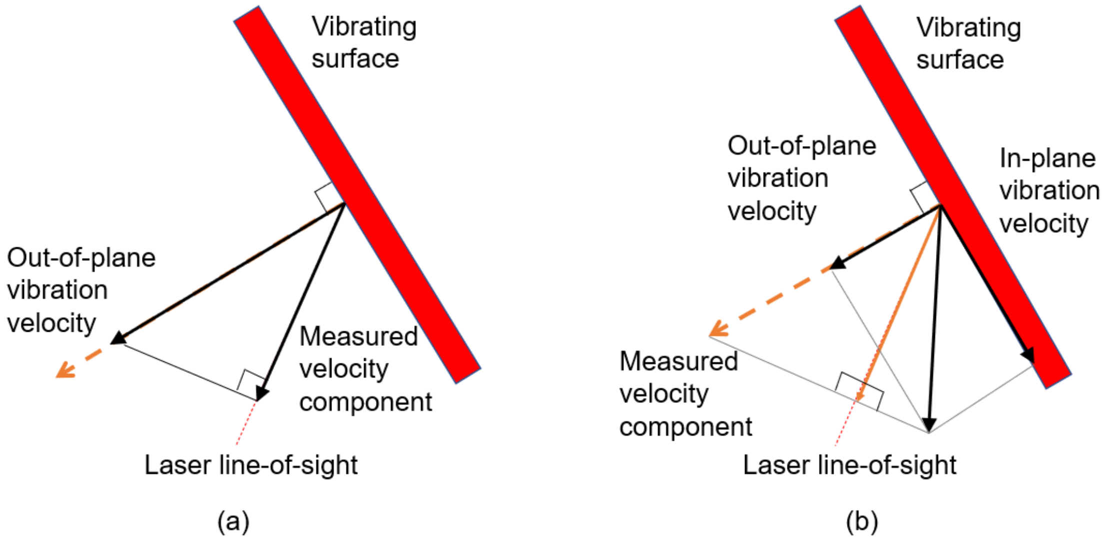

Figure 3.3 Velocity component for (a) out-of-plane vibration and (b) in-plane vibration [84]

The velocity signals at all inspection points are collected and compared. Specifically, using this method, the debonding area and the normal area can be determined by comparing the amplitude of the peak resonance frequency at the inspection point. Signals with relatively higher amplitudes indicate the debonding area. The resonance frequencies in the inspection points with debonding may vary within a very narrow frequency, but can be clearly distinguished from inspection points without debonding.

The frequencies at the maximum resonance peak in inspection points with debonding are determined, and the out-of-surface velocity amplitudes at this frequency in the frequency domain for all inspection points are then obtained. These amplitudes are plotted using a contour map. In this contour map, the different amplitudes will have different colours (or grey scale), resulting in different colours at the debonding area and the normal area, as shown in Figure 3.4. In this way, the debonding area is clearly identified.

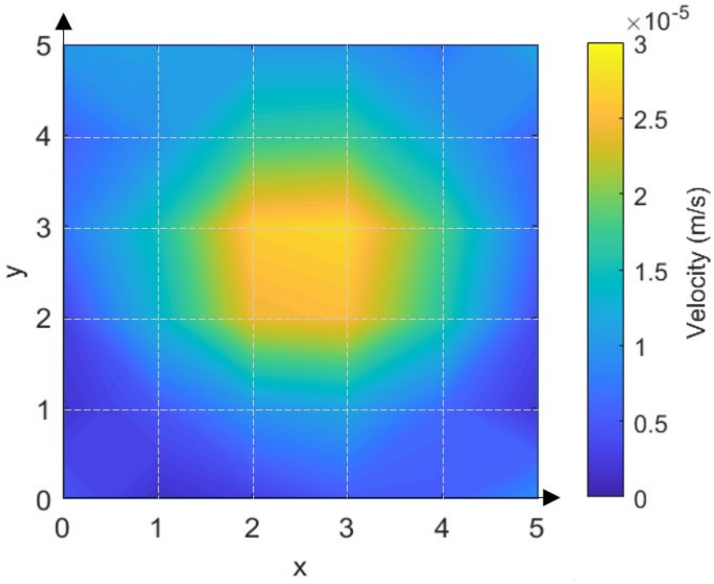

Figure 3.4 Out-of-surface velocity contour map of a tile with square debonding based on experimental measurement

3.2 Experiment setting

The experiment setting should simulate the actual condition of the tile on a high building. The tile is attached to the building surface with adhesive, which can be considered as a tile-adhesive-substrate system. A concrete board is used as a building substrate, and then the tile is attached to the concrete with adhesive. The shape of the adhesive is controlled to simulate different debonding shapes.

3.2.1 Ordinary tile fixing model

Before the experiment, several moulds built by a 3D printer were used to control the debonding area's size and shape. The adhesive layer is set to the recommended thickness, which is 3 mm [172, 173]. The location and the shape of each debonding area are summarised in Figure 3.5. For the square debonding area, the size is set as 67 × 67 mm. Since the size of the tile is 97 × 97 mm, the distance between the edge of the debonding area and the edge of the tile is limited to 15 mm. A tile without a debonding area is also attached to the board as a reference, as shown in Figure 3.5(f).

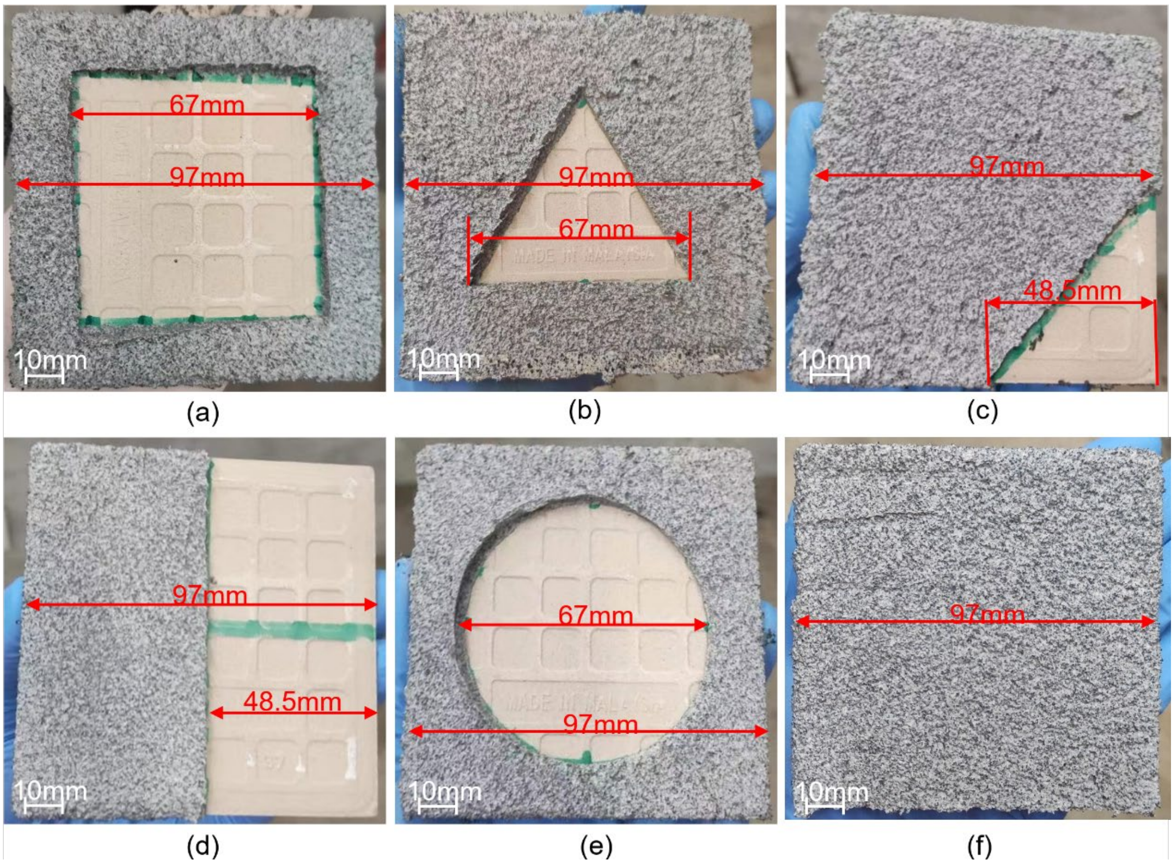

Figure 3.5 Geometries of adhesive layer to simulate (a) square debonding (b) triangle debonding (c) corner debonding (d) half debonding (e) circle debonding (f) no debonding

3.2.2 Excitation system: directional sound speaker

Figure 3.6 shows an external view of the experiment setup. In this experiment, a directional acoustic transducer (Meyer MM-4XP) is used as the sound source, and an LDV (Polytec VibroGo VGO-200) is selected as a laser sensor which is used to record the velocity signal on a selected point. The waveform of the signal is mentioned above in Figure 3.2. The distance between the tiles and the acoustic transducer is 1.0 m. The ceramic tile has a size of 97 mm in both width and height, and 5 mm in thickness. A concrete board (0.9 × 1.8 × 0.02 m) is selected as the outer wall specimen. The short side of the concrete board is placed vertically to the ground, and the tile is fixed on this board's surface. The vibration signal is first generated by a signal generator, a DC source provides the direct current to the acoustic transducer, and the acoustic transducer generates an acoustic wave which can excite the tile on the concrete wall. The signal is an MTNB signal mentioned in Chapter 3.1, the frequency range of this signal is 400~4200Hz. The vibration signal on the tile can be collected by the LDV remotely and synchronised with the measurement software on the laptop. A

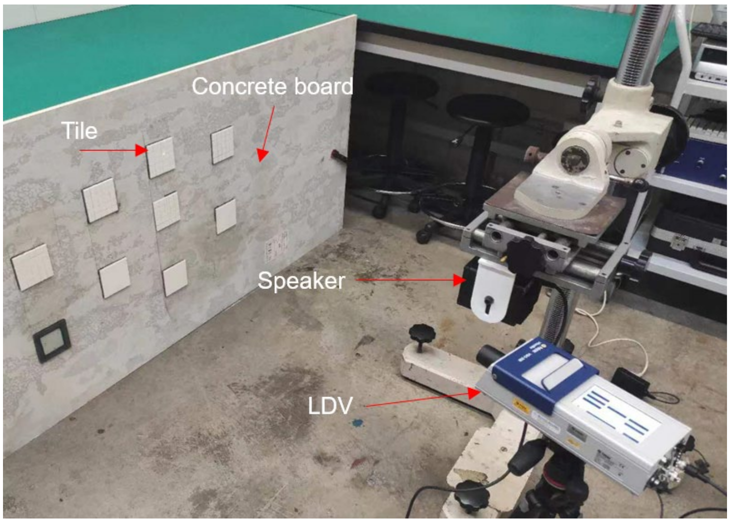

Figure 3.6 Experiment setup with an LDV

36 inspection points are selected on the surface of the tile to identify the debonding area, as shown in Figure 3.7.

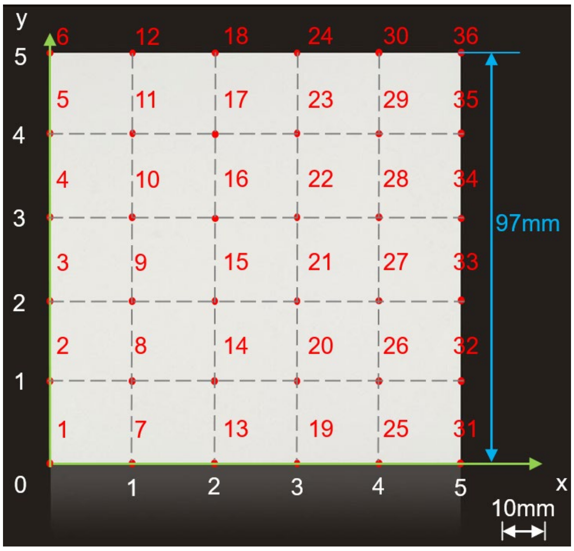

Figure 3.7 Select 36 inspection points on the tile's surface to identify the debonding area

3.3 Data processing

The data processing procedure is essential for the inspection. The signal gathered by the LDV contains background noise. In the meantime, the time-domain signal is hard to analyse. This chapter contains noise reduction and time domain to frequency domain transfer, and then a contour map is used to plot the debonding area.

3.3.1 Reduce noise

In this chapter, seven tiles with different debonding shapes are inspected. As mentioned in Chapter 3.1, the MTNB signal with a maximum frequency of 4200 Hz is used to excite the whole surface of a tile on a wall. The velocity signal induced by the acoustic wave at every 36 points is recorded with corresponding coordinates and then processed. In practice, noise will appear during the experiment. According to the previous studies [60, 115, 122], the natural frequency of the circular-shaped debonding model varies from 1500 Hz to 5000 Hz. This study considers a wide range of engineering debonding shapes, so the frequency range can be correspondingly expanded as 0~6000 Hz to cover more information. Additionally, the directional sound source used in this study is Meyer MM-4XP, and the frequency range of this speaker is 135 Hz~17 kHz, thus the frequency range is finally defined as 200~6000 Hz. A low-pass filter and a high-pass filter are used to limit the frequency of the signal to 200~6000 Hz. Figure 4 shows the captured signal of an inspection point with tile debonding. After the filter, the time-domain vibration signal is clear (Figure 3.8(a)), but the raw signal contains a long period without an exciting signal. Therefore, a time gate is set to limit the signal during the exciting period in Figure 3.8(b). With these methods, a higher signal-to-noise ratio can be achieved.

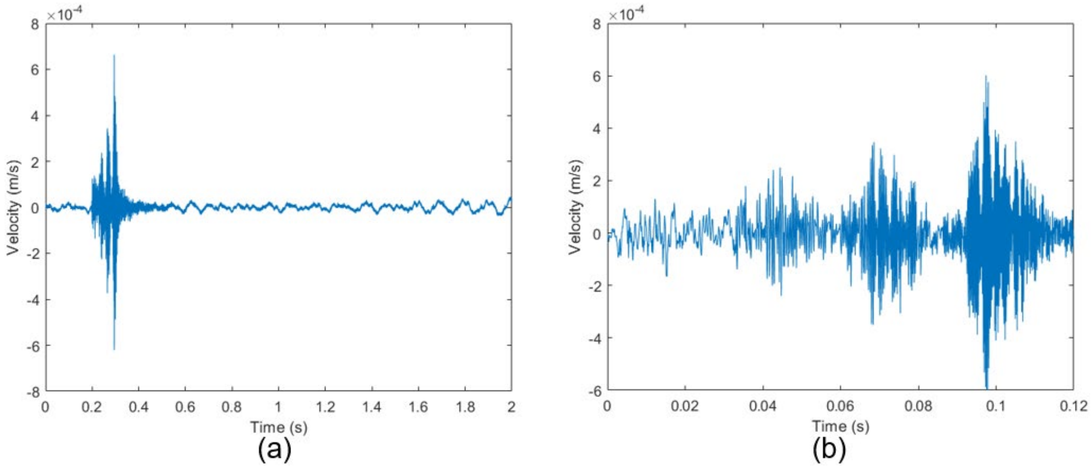

Figure 3.8 Signals collected from inspection point 21 in debonding area: (a) original signal collected by LDV, (b) signal after a low-pass filter and a high-pass filter

3.3.2 Time domain to frequency domain

In data recording stages, the signal amplitude is expressed as a time function, known as the time domain signal. However, the key information of the signal is in the frequency, phase, and amplitude of the component sinusoids. The shape of the time domain waveform is noisy and conveys little information. The frequency distribution of the signal cannot be described.

In complex notation, the time and frequency domains each contain one signal of N complex points. In the time domain, the N points are repeated over and over from negative to positive infinity. These complex points are composed of two numbers, the real part and the imaginary part, as shown in Equation (4.1).

$$F(X) = Re(X) + Im(X) \tag{4.1}$$

The Fast Fourier Transform (FFT) is a common method used in data processing. The FFT is an efficient algorithm that digitally computes a discrete signal's Discrete Fourier transform (DFT) [174].

The DFT converts a time-domain sequence x(n) of N complex points to a frequency-domain sequence X(k), as shown in Equation (4.2):

$$X(k) = \sum_{n=0}^{N-1} x(n) \cdot e^{-j\frac{2\pi}{N}kn} \, (k = 0, 1, \dots, N-1) \tag{4.2}$$

The computational complexity of DFT is O(N2).

In 1965, Cooley and Tukey [175] developed the FFT to reduce computational complexity. The FFT can split the sequence into even and odd subsequences recursively:

$$X(k) = \underbrace{\sum_{m=0}^{\frac{N}{2}-1} x(2m) \cdot e^{-j\frac{2\pi}{\frac{N}{2}}km}}_{Even\ Subscquence} + \\ e^{-j\frac{2\pi}{N}k} \cdot \underbrace{\sum_{m=0}^{\frac{N}{2}-1} x(2m+1) \cdot e^{-j\frac{2\pi}{\frac{N}{2}}km}}_{Odd\ Subscquence} \, (k = 0, 1, \dots, N-1) \tag{4.3}$$

The recursion layers are $\log_2$N. The computational complexity of FFT is O(NlogN), which is much less than DFT.

In the frequency domain, the frequency is only considered to be from 0 to positive infinity. Therefore, N/2+1 sample frequency domains are produced.

Using the FFT, every input signal can be represented as a group of cosine waves, each with a specified amplitude and phase shift.

As several peaks are found in the frequency domain, the highest peak in Figure 3.9(a) is chosen as the resonance peak. This resonance peak denotes the first mode natural frequency of the debonding. Similarly, the frequency domain for a point without debonding is shown in Figure 3.9(b). Compared with the signal with debonding, the amplitude of the signal without debonding is much smaller.

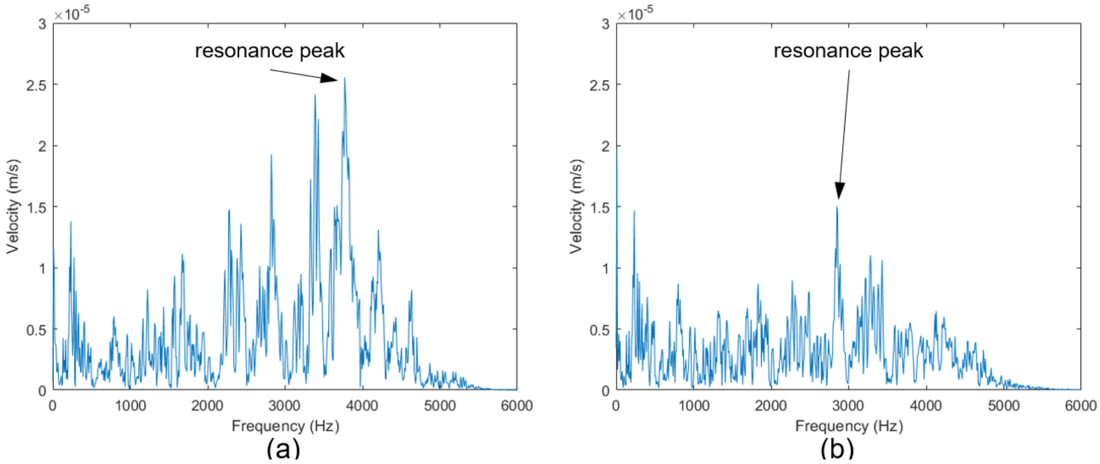

Figure 3.9 Signals collected from inspection points after FFT: (a) in the debonding area, (b) in the normal area

3.3.3 Plot debonding map

The maximum peak resonance frequencies in the FFT at all inspection points of each tile are summarised in Table 3.1.

Table 3.1 Maximum peak resonance frequencies of different tiles

Debonding shape	Experience resonance frequency (Hz)	Simulation resonance frequency (Hz)
Normal	3138	3198
Square	3771	3869
Triangle	3321	3308

Circle	3671	3629
Half	3829	4010
Corner	3213	2999

Then, the velocity amplitudes of the maximum resonance frequency at all 36 inspection points are collected, and the corresponding amplitudes are plotted on a map. In practice, the situation is more complex. Noise, including the noise of the LDV and the workplace, will also be collected by the LDV equipment. Figure 3.10 shows the debonding maps of all six debonding shapes in Figure 3.5. Different debonding shapes result in different shapes of the debonding map. The debonding map with a shape of corner debonding and half debonding has a relatively clear profile.

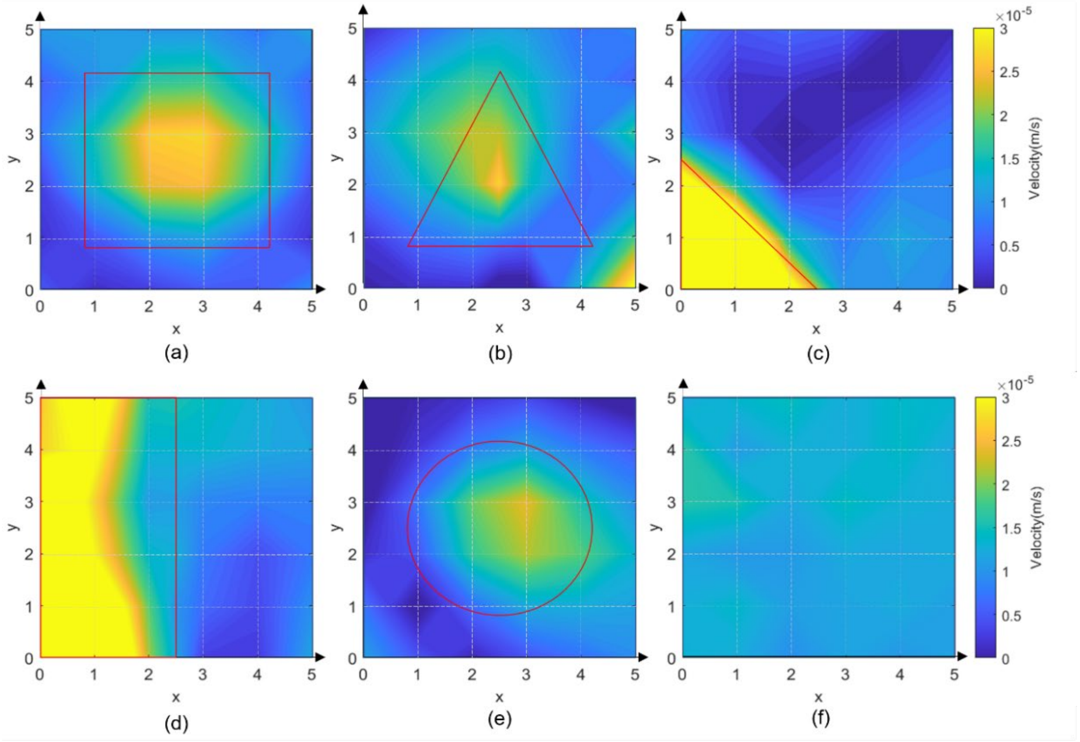

Figure 3.10 Debonding map of different debonding shapes: (a) square debonding (b) triangle debonding (c) corner debonding (d) half debonding (e) circle debonding (f) no debonding

3.4 Non-contact inspection of thick tile debonding

The designer of the Sydney Opera House, Jørn Utzon, expected to present a roof with a smooth curve and a glittering surface to the visitors [176]. Therefore, he entrusted a Swedish tile manufacturer, Höganäs, to produce specially designed tiles. In the meantime, Jørn Utzon didn't want the workers to attach the tile directly to the roof since this stage may create an uneven surface. As a result, the ribs of the roof shells on the Sydney Opera House are covered by precast concrete lids. According to the official conservation management plan written by Alan Croker [177], the tiles are directly fixed on the concrete lids with cement, as shown in Figure 3.11(a). After the cement set, the concrete lids are assembled in a factory, then transferred to the Sydney Opera House construction site. Finally, these concrete lids are fixed on the roof ribs with screws, as shown in Figure 3.11 (c).

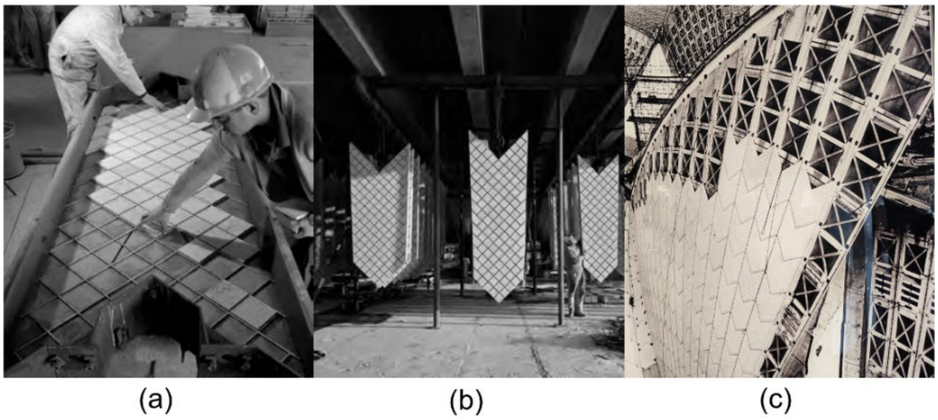

Figure 3.11 Precast concrete lid in (a) tile assembling process (b) factory (c)construction site of the Sydney Opera House [177]

The tile used on the tile lid is made by a Swedish tile manufacturer Höganäs. The size of the tile is 120 × 120 × 14 mm. The pre-debonding areas are formed in four different shapes, as shown in Figure 3.12.

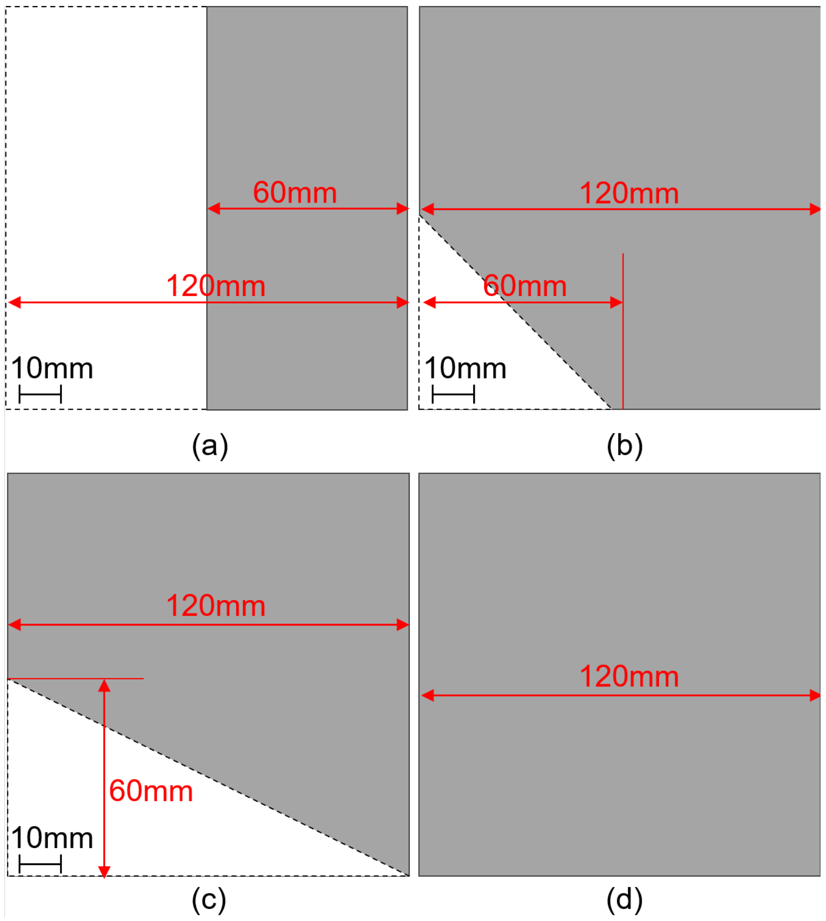

Figure 3.12 Geometries of the PI film to simulate (a) corner debonding (b) half debonding (c) long corner debonding (d) no debonding

Figure 3.13(a) shows that a very thin Polyimide (PI) film is attached to the back of the tile as a pre-debonding. Then, the tile is inserted into a mould made of acrylic board to form the lid to simulate the tile assembly process for the precast concrete lid, as shown in Figure 3.13(b). Finally, the cement was added and solidified in the mould, and the roof lid is shown in Figure 3.13(c). As mentioned in the official conservation management plan [144], the thickness of the precast concrete lid is 120 mm. As a result, the cement layer in the specimens is also determined to be 120 mm. The size of the tile lid specimen is 120 × 120 × 134 mm.

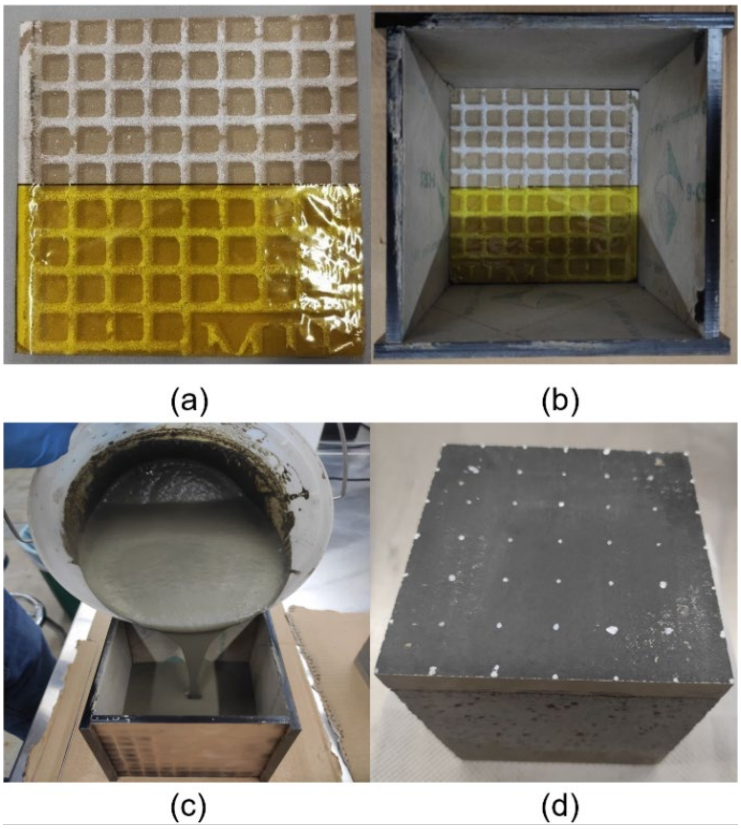

Figure 3.13 Roof lid manufacturing (a) attach a very thin PI film to the tile (b) insert tile into the acrylic board (c) add cement into the mould (d) roof lid specimen produced

The size of the tile is larger than the commonly used 97 × 97 × 3 mm tile. Therefore, 49 inspection points were placed on the surface of the tile lid to identify the debonding area, as shown in Figure 3.14.

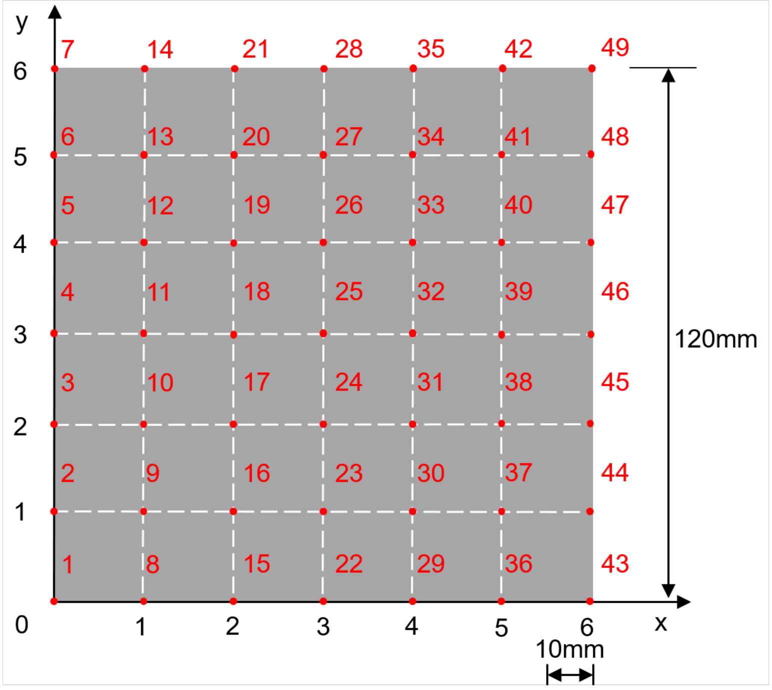

Figure 3.14 49 inspection points on a tile

The different debonding shapes of the specimens used in this study are mentioned in Figure 3.12. The instruments used in this part are the same as mentioned in Chapter 3.2. The experiment setup is shown in Figure 3.15. A tile lid is placed on the ground, a directional acoustic transducer is used as a sound source, and an LDV is used to record the pressure wave at each inspection point.

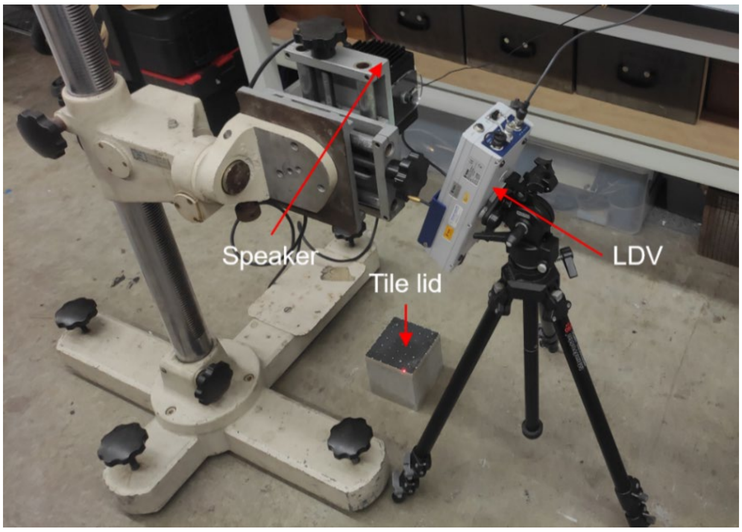

Figure 3.15 Experiment setup for inspecting thick tile

The debonding map of each specimen is shown in Figure 3.16. Compared with

Figure 3.10, though the tile thickness increases, the profile can still be recognised. The debonding with a long corner shape has the clearest profile. In the meantime, other debonding shapes can also be identified.

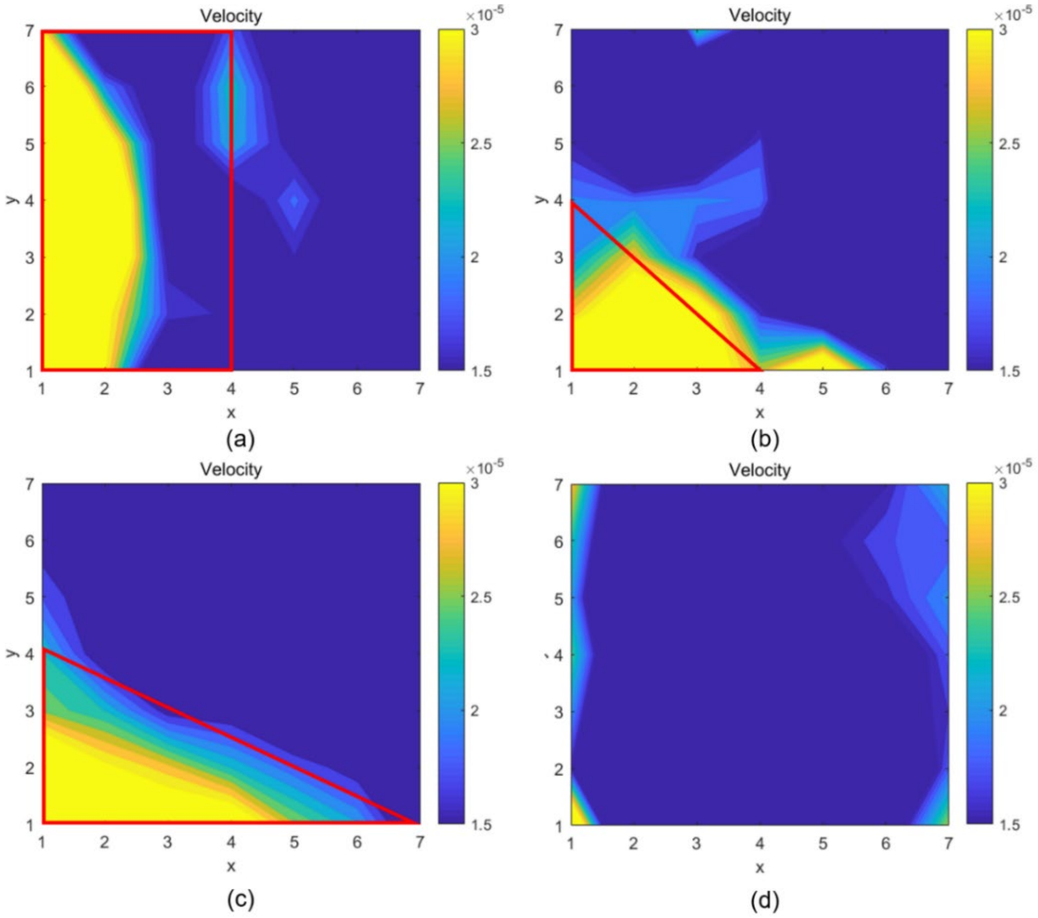

Figure 3.16 Velocity map of the tile lid with (a) corner debonding (b) half debonding (c) long corner debonding (d) no debonding

3.5 Summary

In this chapter, a non-contact inspection method is developed to inspect the debonding of tiles on a wall, using an LDV and an acoustic wave of a sweeping frequency band based on the activated vibration behaviour of the tiles with and without debonding. The velocity amplitudes in the frequency domain at multiple points are plotted to construct a velocity contour map to identify the debonding area. Based on the experiments, the velocity contour maps correlate well with the actual debonding areas, demonstrating the method's capability for quantitatively detecting tile debonding. The experiment also shows that the increase in tile thickness does not affect the inspection accuracy.

This method can be further developed for future applications to inspect defects within other structures at a distance. Specifically, this method eliminates the need to deploy sensors directly onto the tiles. In contrast to contact-based inspection techniques such as impact hammer testing, which require workers to operate at high altitude and manually strike each tile, the proposed approach significantly reduces labour costs and enhances safety. Furthermore, for structures with complex curved surfaces, such as the Sydney Opera House, the construction of scaffolding would be extremely time-consuming. Another advantage of the proposed acoustic method is its portability. The entire inspection system can be mounted on an unmanned aerial vehicle (UAV), enabling fully automated inspection without direct human intervention. This configuration constitutes a round-the-clock inspection system capable of examining tiles both during the day and at night, thereby substantially reducing the total inspection duration. The high efficiency and rapid assessment offered by this acoustic detection method are particularly advantageous for large-scale buildings. In addition, the current method can be extended with the aid of deep learning to improve its efficiency. Signals collected in this study can be used to build a database where different debonding shapes can be accordingly classified, as different vibration signals measured by the LDV can be related to various debonding shapes. Then, the deep learning model can be trained based on this database. After the model has been well trained, one single signal collected at one single inspection point may be enough for the prediction of any unknown debonding shape.

Chapter 4: Numerical study of non-contact detection of tile debonding using acoustic excitation

This chapter presents the development and validation of a numerical model designed to simulate the propagation of acoustic waves and their interaction with tiled structures for the purpose of detecting debonding defects. The model is constructed to replicate the experimental setup, incorporating three key components: the wave propagation medium (air), the tile, and the adhesive layer. A sound wave is generated at a predefined reference point and propagates through the air toward the tile surface. The tile is affixed to an adhesive layer, and the interactions between the incident acoustic wave and the tile are numerically analysed. Vibration signals are collected at 36 inspection points distributed across the tile surface, and a debonding map is subsequently generated. A comparative analysis reveals that the numerical model yields a more distinctly resolved debonding profile compared to the experimental results.

4.1 Tile fixing model building

Numerical modelling requires calculating the velocity at each inspection point. For a rectangular plate, the plate equation at each inspection point can be summarised in Equation (4.1) [178]:

$$\frac{\partial^4 w}{\partial x^4} + 2\frac{\partial^4 w}{\partial x^2 \partial y^2} + \frac{\partial^4 w}{\partial y^4} + \frac{12\rho(1-\sigma^2)}{Egh^2}\frac{\partial^2 w}{\partial t^2} = 0, \tag{4.1}$$

where ρ is the density, σ is Poisson's ratio, E is Young's modulus, h is the thickness of the plate, and w is the displacement at the point (x,y) at time t. The displacement w can be described as:

$$w = Wsin\omega t = A\theta(x)\phi(y)sin\omega t, \tag{4.2}$$

where A is the component amplitude coefficient, $\theta(x)$ and $\phi(y)$ are characteristic beam functions, and $\omega = 2\pi f$ is the circular frequency. In general, W can be assumed to be an infinite series. Then the out-of-surface velocity can be defined as:

$$v = \dot{w} = A\big(\dot{\theta}(x)\phi(y)sin\omega t + \theta(x)\dot{\phi}(y)sin\omega t + \theta(x)\phi(y)\omega cos\omega t\big) \tag{4.3}$$

Each term of the series satisfies a specific boundary condition and Equation (4.1), corresponding to different vibration modes [179]. In practice, the vibration equations of a plate with complex boundary conditions are hard to define by theoretical calculation. As a result, finite element analysis (FEA) is used in simulation to solve Equation (4.1) under different boundary conditions and different debonding conditions.

The simulation is conducted using FEA software to model a tile specimen and the sound source in a wave propagation model. In this simulation, the FE models of the tile, adhesive layer, and wave propagation medium (air) are established using Abaqus/CAE. To study the wave propagation between the sound source and the specimen in detail, boundary conditions, geometrical relationships, and corresponding analytical procedures are specified in this simulation, as summarised in Table 4.1.

Table 4.1 FE model for simulation

Geometrical models	Wave propagation medium (air)	Tile	Adhesive laver
Model size	Length: 2 m, radius: 0.5 m	97 × 97 × 5 mm	97 × 97 × 3 mm
Boundary condition	Tied to the tile	Tied to the adhesive layer	Fixe to the wall

The constitutive parameters, including debonding area, medium properties, sound pressure, and sound boundary, are taken into consideration systematically to simulate the response of the tile after being excited by the sound wave. 36 measurement points are selected on the surface of the tile. The vibration signals collected from these measurement points are filtered and processed using MATLAB. The time-domain signals are transferred into frequency domain signals, and the amplitudes of the resonance frequency of the debonding area at each measuring point are collected. Following this, the vibration map of the tile is plotted using the same procedure as articulated in the previous section.

In this simulation, the FE model contains three parts: the wave propagation medium (air), the tile, and the adhesive layer. To simplify the FE model, the concrete wall that holds the tile is not included in this simulation.

First, the medium (air) is modelled in Abaqus/CAE as an acoustic medium to simulate wave propagation. To simplify the simulation, the medium is designed as a capsule shape. In this medium, the propagation model is set as acoustic, the speed of sound in the air is set as 340 m/s, and the air density is set as 1.25 kg/m^3. The tile and adhesive layer are placed within the medium based on the experimental setting. Two reference points are placed within the medium, as shown in Figure 4.1. Reference Point 1 (RP-1) represents the sound source, which is 1 m away from the tile’s surface in the experimental setting. In the experimental setting, a sound level meter is used to present the sound pressure level (SPL) of the signal, which is 112.4 dB. The SPL can be defined by Equation (4.4) [180]:

$$SPL = 20\,log\frac{p}{p_0} \tag{4.4}$$

where p_0 is the reference sound pressure in the air, which is 2×10^{-5} Pa. Therefore, the sound pressure at the RP-1 is 8.3373 Pa, which corresponds to the amplitude of the exciting signal. As mentioned above, the waveform of the exciting signal is shown in Figure 3.2.

Reference Point 2 (RP-2) represents the stand-off point. For an incident wave like this simulation, the stand-off point should be located as close to the structure as possible [181]. In the model, the stand-off point is where the analysis begins. As a result, RP-2 is placed at the tile's surface, opposite the sound source (RP-1), as shown in Figure 4.1.

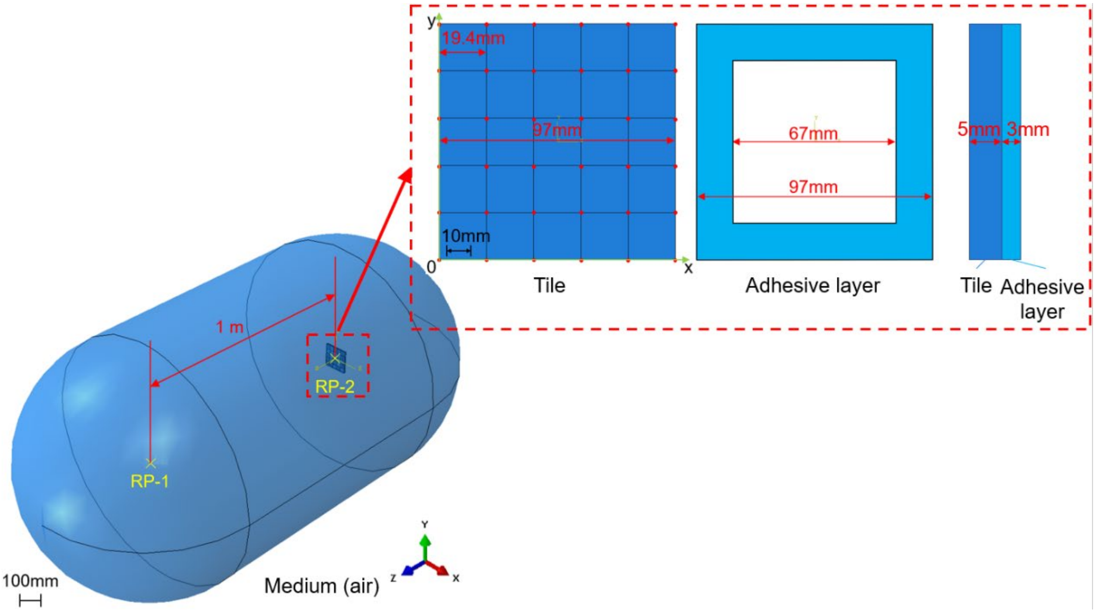

Figure 4.1 Geometric models in simulation for a tile with square debonding

To plot the vibration map, 36 measure points are deployed equally on the surface of the tile (in accordance with Figure 4.8). Then, to establish an FE model to fix the tile, the adhesive layer is modelled as a deformable component in Abaqus/CAE. Different shapes of debonding areas are also modelled, as shown in Figure 4.2.

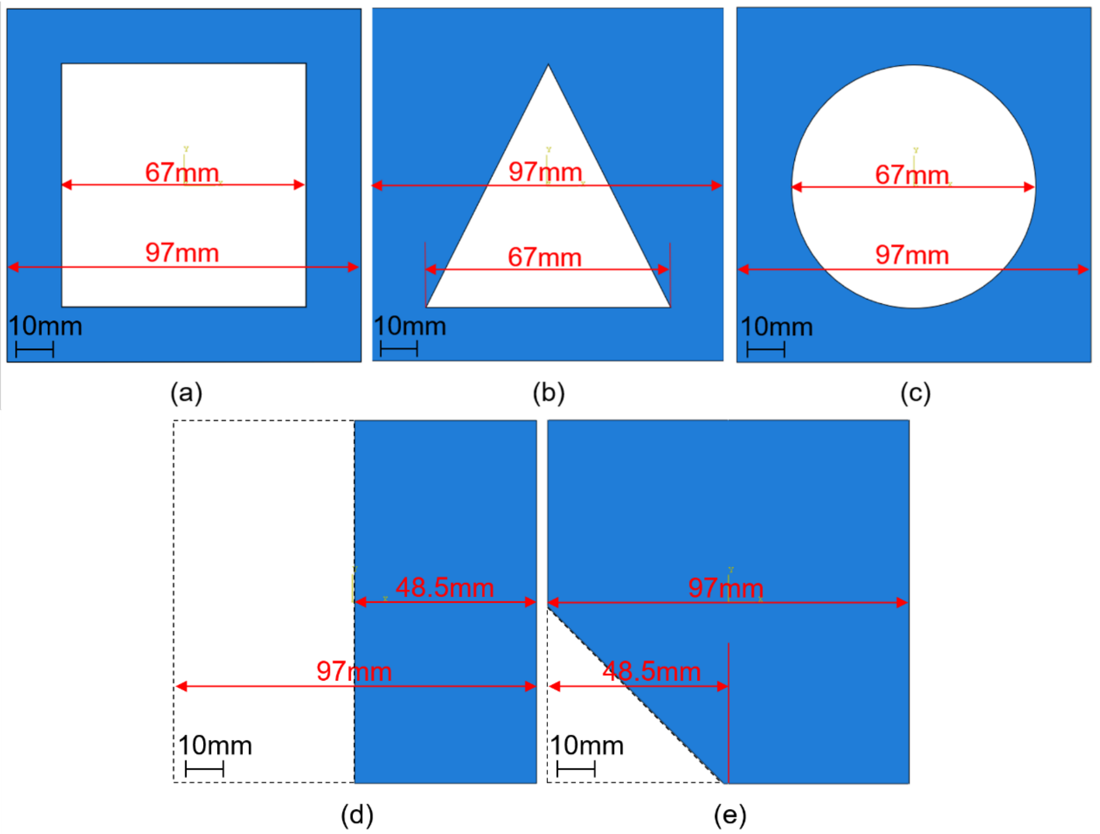

Figure 4.2 Geometric models of adhesive layers: (a) square debonding, (b) triangle debonding, (c) circle debonding, (d) half debonding, and (e) corner debonding

4.2 Model boundary conditions

In the actual construction, the back of the tile is fixed stably to the concrete wall through the adhesive layer, and the concrete wall is relatively large compared with the tile and the adhesive layer. Therefore, all six freedoms of the adhesive layer are limited in order to fix all the displacements and rotations on the adhesive layer. The tile is attached to the adhesive layer by “tie” contact so that the tile and the adhesive layer have the same DOF on the contact surface, so as to simulate the interface of the solid surface (tile and adhesive layer) and the gas surface (air). Additionally, the sound area of the simulation is limited within the capsule-shaped air medium to simplify the simulation. The sound boundary is set as the outer surfaces of the medium, as shown in Figure 4.1. These interactions are set as "acoustic impedance". To simulate the infinite sound medium, the boundary is set as "nonreflecting". These nonreflecting types of surfaces are set as "circular" for the middle part and "sphere" for the two ends to fit the shape of the medium. The boundary conditions of the models are diagrammatically presented in Figure 4.3.

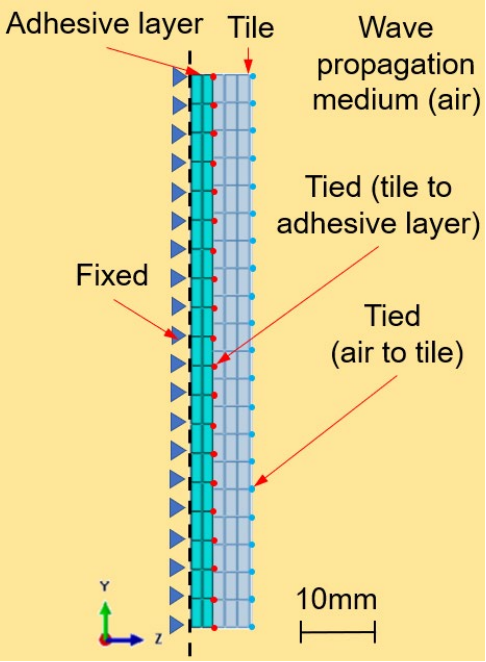

Figure 4.3 Boundary conditions of tile in FEM simulation

The mesh size of FE models influences the efficiency and accuracy of the simulation. A large mesh size may result in low accuracy but high efficiency, and vice versa. Therefore, different mesh sizes are evaluated in mesh-convergence analyses to reduce the computational time without lowering the numerical accuracy. As a result, the element sizes of the tile and adhesive layer are 2 mm, and the element size of the medium (air) is 50 mm for the analysis in this study. Besides, the element size of the contact surface in the medium is 2 mm.

The shapes of the tile and adhesive are regular, therefore the element shape of the tile and adhesive is set as a cube ("Hex") to reduce computational resources, while the element shape of the air is set as a tetrahedron (“Tet”) since the air model contains curved boundaries. The element types for both the tile and adhesive are set as solid (“C3D8R”) to simulate tile vibration, and the element type of the air is formatted as acoustic (“AC3D4”) to simulate acoustic wave propagation. The mesh of FE models is shown in Figure 4.4.

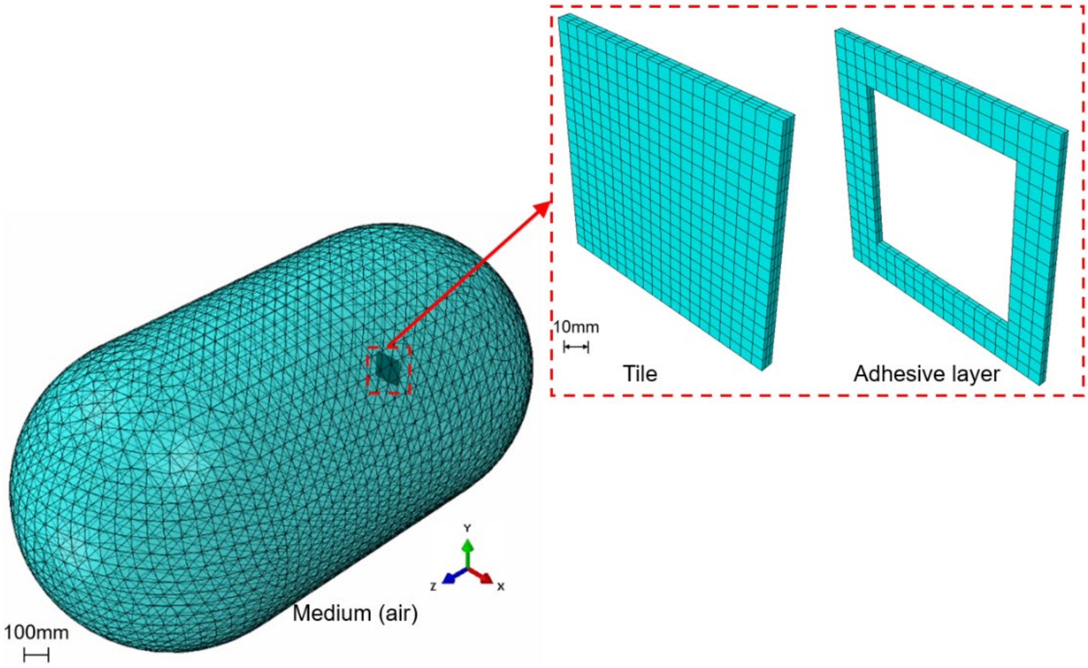

Figure 4.4 Mesh of FE models with square debonding

Based on the experimental setting, the tile used in this experiment is a Johnson 97 × 97 mm white gloss spectrum wall tile, and the adhesive used in this experiment is Dunlop premixed Resaflex tile adhesive. Their related material properties are not available in the reference provided by the manufacturers. Therefore, related experiments are also conducted, as shown in Figure 4.5. The densities of the tile and adhesive are measured, as well as their elastic behaviours. For the tile, a 3-point bending test is undertaken using a specimen (160 × 41 × 5 mm). A compression experiment is also conducted for the adhesive. The specimen of the adhesive is a cylinder with a 13.5 mm diameter and 9 mm thickness.

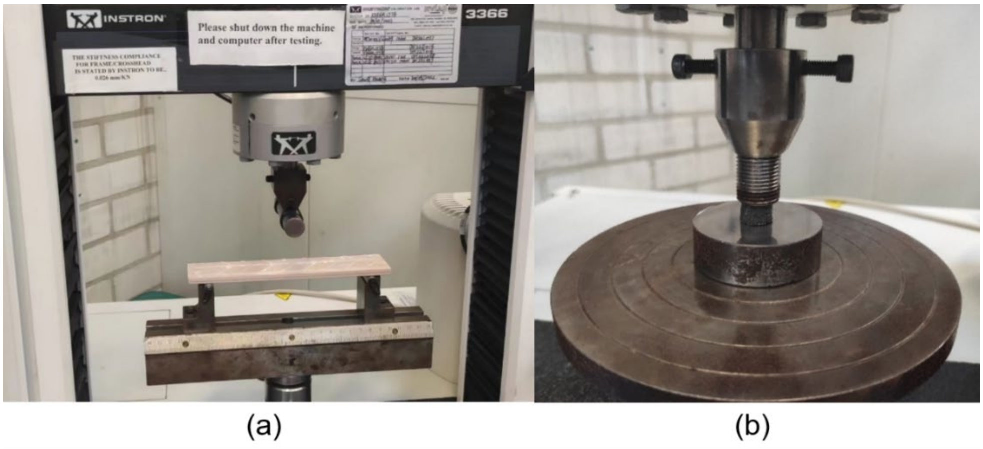

Figure 4.5 (a) 3-point bending test for the tile (b) compression experiment for the adhesive

In this simulation, the sound speed within the propagation model should be determined. In the material properties, the sound speed is defined by Equation (4.5) [180]:

$$c = \sqrt{\frac{B}{\rho}} \tag{4.5}$$

Where c is the sound speed in the medium, B is the isentropic bulk modulus of the medium, and ρ is the density of the medium. After checking the reference and conducting the experiment, the material properties of the tile and adhesive are summarised in Table 4.2 [180].

Table 4.2 Material properties for FEM simulation [180]

Material	Density(kg/m^3)	Isentropic bulk modulus (MPa)	Young's modulus (GPa)	Poisson's ratio
Tile	2209.7	/	19.55	0.24
Adhesive	1458.1	/	1.1	0.3
Air	1.21	0.143	/	/

4.3 Comparison between simulation and experiment

As the control group, the out-of-surface velocity map of the normal tile is plotted in

Figure 4.6. As shown in the simulation result (Figure 4.6(b)), the differences between each inspection point are very small. For the experimental result (Figure 4.6(a)), though there is no debonding in this tile, the amplitudes at each inspection point still vary. This situation may be caused by the small cavities within the adhesive layer while tiling in practice, resulting in noise signals.

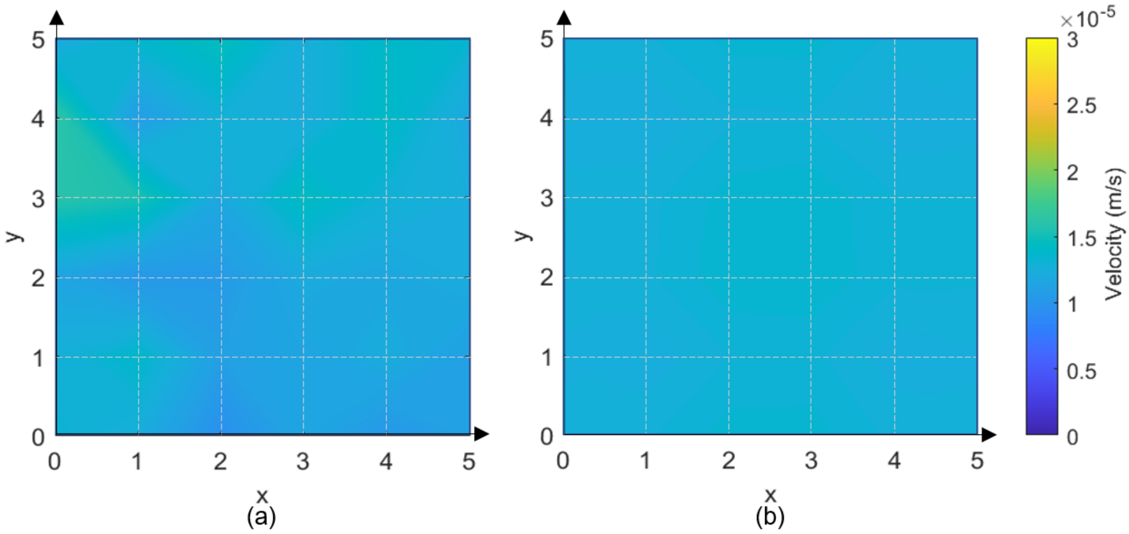

Figure 4.6 Velocity map of the tile without debonding: (a) experiment (b) simulation result

The debonding area of the tile with a square debonding area is plotted in Figure 4.7(a). Similarly, a repetitive experiment of a tile with the same shape of debonding area is also generated. The velocity map of another tile with the same square debonding area is shown in Figure 4.7(b). Figure 4.7 indicates that this method is consistent with the two results, showing a similar trend. The frequency of the first mode in the second tile is a little higher, while the amplitude in the second tile is a little higher. Compared with the experimental results as illustrated in Figures 4.7(a) and (b), the simulation result shows a good agreement, as in Figure 4.7(c).

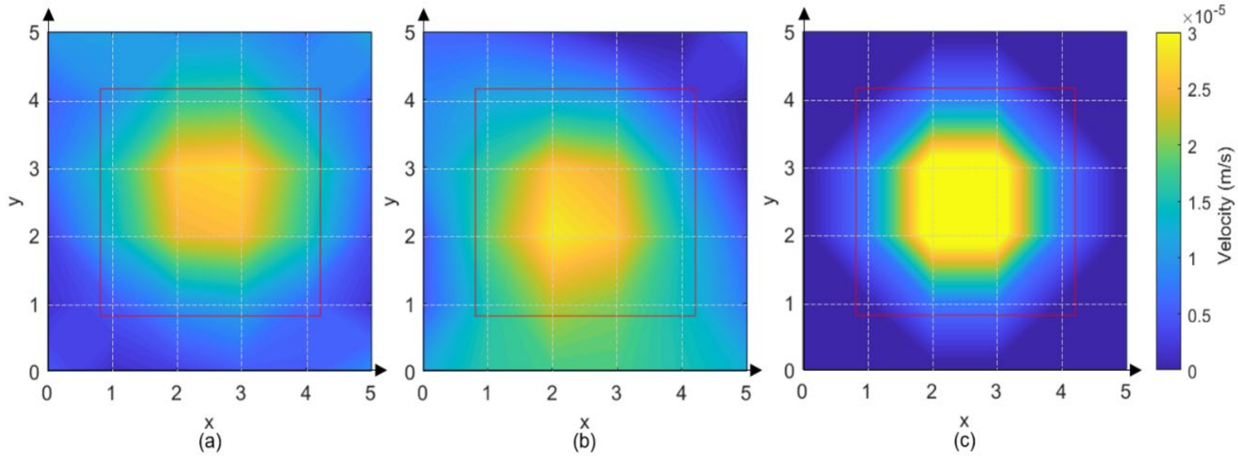

Figure 4.7 Velocity map of the tile with a square debonding area: (a) Experiment 1 (b) Experiment 2 (c) simulation

Then, using the same method, the simulation and experiment results of the tile with a triangle debonding area (shown in Figure 3.5(b)) and a circle debonding area (shown in Figure 3.5(e)) are plotted in Figure 4.8 and Figure 4.9, respectively. The simulation results and these two experiments show good consistency in shapes, and the velocity maps of the simulation results are more apparent for both shapes. The results show that this method can identify the debonding, but the shape of the debonding area is not clear enough to be recognised.

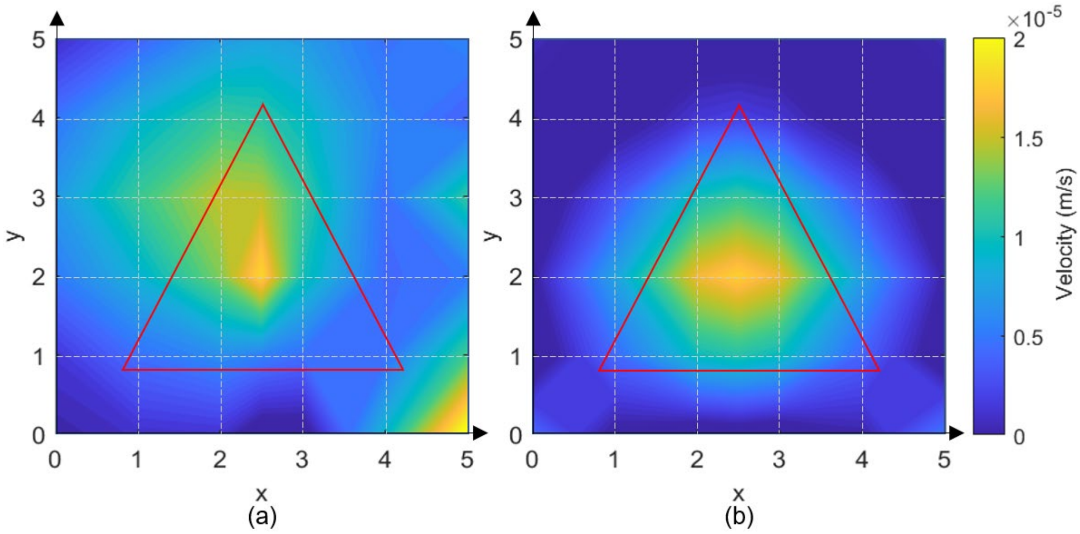

Figure 4.8 Velocity map of the tile with a triangle debonding area: (a) experiment and (b) simulation

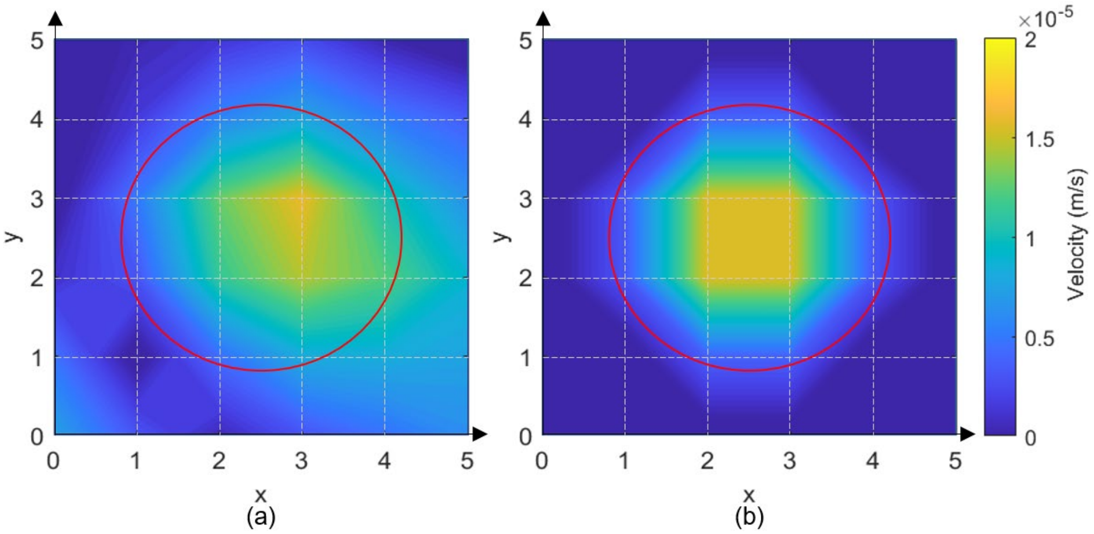

Figure 4.9 Velocity map of the tile with a circle debonding area: (a) experiment and (b) simulation

Compared with the square debonding area mentioned in Figure 4.7, the amplitudes of the triangle and circle are also smaller. This difference may be caused by the sizes of the different debonding areas: 4489 mm^2 for the square, 1943.79 mm^2 for the triangle, and 3525.65 mm^2 for the circle. The larger debonding area may result in a larger amplitude of vibration, causing the mapping to be clearer.

Similarly, the results for the tiles with half and corner debonding (shown in Figures 3.5(c) and (d)) are plotted in Figure 4.10 and Figure 4.11, respectively. These kinds of debonding have a substantial amplitude, with a relatively clear edge being plotted between the debonding and normal areas. The simulation results have better resolution compared with the experimental results. As mentioned above, these two kinds of debonding can be simplified into cantilever plates, which account for this distinction. The amplitude of this kind of model is more significant compared with the simply supported plate. Therefore, the debonding area in the velocity map is more apparent.

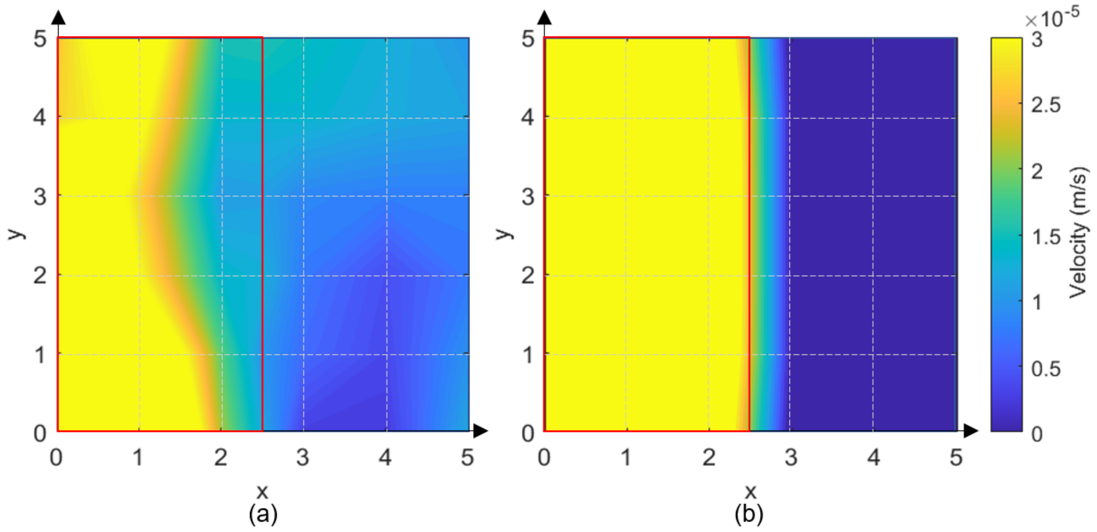

Figure 4.10 Velocity map of the tile with half debonding area: (a) experiment and (b) simulation

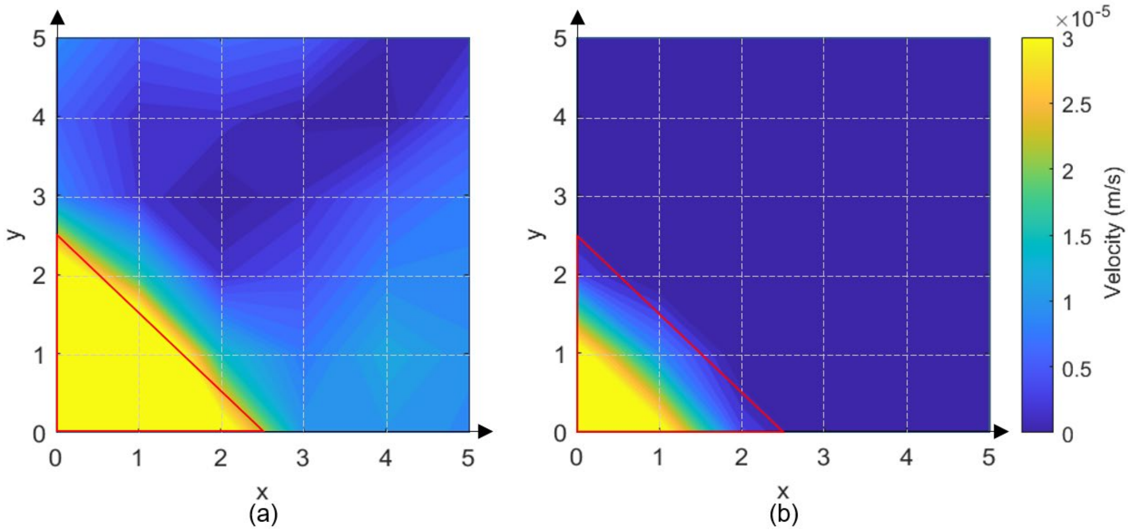

Figure 4.11 Velocity map of the tile with corner debonding area: (a) experiment (b) simulation

Generally, the simulation results have a better resolution than the experimental ones. This is because the numerical model is ideal, while the experimental model is not. For example, for the corner debonding as shown in Figure 4.11, six inspection points are found within the debonding area. As compared with the normal area, the resonance velocities in the debonding area are much larger in both the modelling and the experiment. By evaluation, the resonance velocities of all points in the debonding area are larger than 1.2×10^{-5} m/s. Therefore, 1.2×10^{-5} m/s is defined as a threshold to evaluate the inspection accuracy in both the experiment and the simulation. In this way, as shown in Figure 4.9, the debonding areas of the experimental result and the simulation result are defined as 1375.83 mm^2 and 972.31 mm^2, respectively, while the actual debonding area is 1176.13 mm^2. Therefore, the errors of the experiment and simulation results are -16.98 % and 17.33 % respectively. The errors are summarised in Table 4.3.

Table 4.3 Quantitative analysis of the accuracy

Debonding shape	Experiment error	Simulation error
Square	26.65%	16.41%
Triangle	48.36%	36.36%
Circle	25.16%	25.86%
Half	32.17%	10.51%
Corner	-16.98%	17.33%

As shown in Table 4.3, this study's experimental error varies from -16.98 % to 48.36 % for all debonding cases, while the simulation error varies from 10.51 % to 36.36 %.

4.4 Summary

In this chapter, an effective numerical model is developed to model the inspection process, which can identify the predefined debonding areas well. The finite element models of the tile, adhesive layer, and wave propagation medium (air) are established to simulate the activated vibration signals of tiles with different debonding areas, as in the experimental studies. The simulation results show a better inspection accuracy compared with experimental results, proving the effectiveness of the numerical model.

This numerical can be further developed to analyse other specimens, and powerfully improve the debonding signal database. The vibration signal generated by the numerical model can be used in deep learning networks to achieve a higher accuracy.

Chapter 5: Deep learning networks in non-contact inspection

In this chapter, a two-stage debonding shape-identifying method is established based on deep learning. The first step of this chapter is to build a vibration database. The database contains the debonding and normal signals collected from tiles with different debonding shapes. The deep learning (DL) networks can be trained with this database. Three deep learning (DL) networks are built and trained based on the database. In stage I, the 1st DL network is to identify debonding types from predefined geometries. In stage II, the extra DL network is used to determine whether the debonding shape in the tile to be inspected belongs to a known shape, while the 2nd DL network is used to screen out unknown debonding types for subsequent specific debonding evaluation. The results show that the two-stage method using the three networks is fast and effective in evaluating tile debonding with detailed information, providing a novel and practical approach for engineering applications. After recognising the unknown shape with the two-stage method, the unknown debonding shapes can also be added to the raw database to improve the accuracy of the prediction.

5.1 Methods and procedures

The inspection method for this chapter is as exact as shown in Chapter 3 and 4. Moulds are used to form the adhesive layers to control the sizes and shapes of the debonding areas, as shown in Figure 5.1(a)~(f). The size of the ceramic tile is the same as the tile shown in Figure 3.5. The outer wall specimen is selected as a concrete board (0.9×1.8×0.02m). The long side of the concrete board is placed on the ground. Then, these tiles are tiled onto the concrete board to simulate the actual condition.

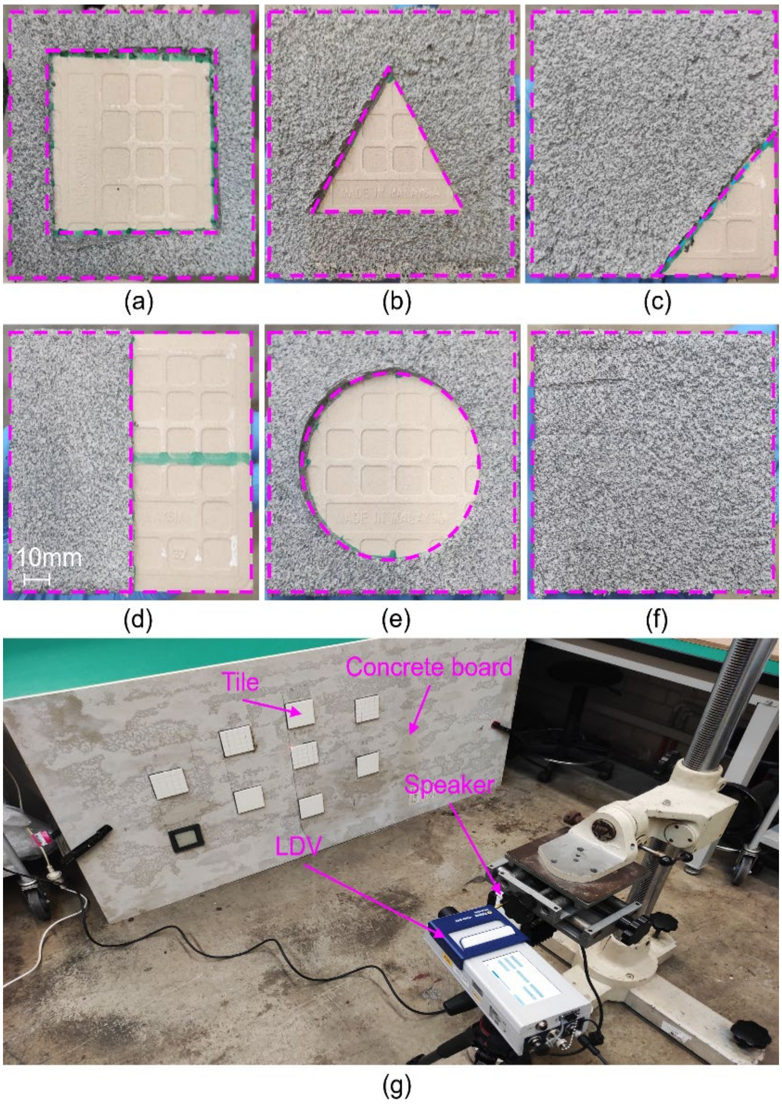

(a) (b) (c)
(d) (e) (f)
(g)

Figure 5.1 Tiles with different adhesive layer shapes and experiment setup

After the tiling procedure, the tile is inspected by an acoustic inspection method. The experimental setup of this method is shown in Figure 5.1(g). In this work, the sound source is selected as the Meyer MM-4XP, which is a directional acoustic transducer. The sound source is placed 1 m away from the tile. The tile is excited by the acoustic wave generated by the sound source. Then the velocity signals at each inspection point are recorded by an LDV (Polytec VibroGo VGO-200) remotely. A signal generator is used to generate vibration, and a direct current (D.C.) source is used to provide the direct current for the sound source.

The data are collected from an acoustic inspection experiment. The adhesive fixes the tile on a concrete wall. During the inspection, the speaker generates a pressure wave which is a burst acoustic signal, and then the pressure wave excites the tile. LDV equipment is used to record the vibration signal excited by the pressure wave on the surface of the tile. This method uses the widely used multitone burst (MTNB) signal to excite the whole surface of the tile[115, 117, 122].

Then, 36 inspection points are selected on the surface of the tile, as shown in Figure 3.7. An LDV is used to measure the velocity signals at these inspection points. Five experiments are conducted on each tile, and 1080 velocity signals are collected in total.

The velocity signal induced by the acoustic wave on every 36 points is recorded with corresponding coordinates and then processed. The signal collected by the LDV equipment is a time-domain signal. In practice, the equipment will also collect the noise during the experiment, and the recorded signal will also contain the signal before and after the exciting signal. As a result, filters on signals are required. The resonance frequency of the LDV equipment is very low [116], and the maximum frequency of the exciting signal is 4200Hz, so a low-pass filter and a high-pass filter are used to limit the signal frequency to 200~6000Hz. In the meantime, a time gate is used to limit the signal during the exciting period. The time domain signal after the filter and time gate is shown in Figure 3.8(a). The time domain signal can only describe the vibration in the time period. The frequency behaviour of the signal cannot be shown in the time domain. Therefore, the continuous wavelet transform (CWT) is used to plot the time-frequency scalogram image, describing the time and frequency distribution [170]. Finally, all 1080 CWT images are imported into the database.

Then, the DL networks are designed and trained. All the DL networks in this study have the same structure. They contain an input layer, five convolution layers, one dropout layer, three fully connected (FC) layers, one softmax layer, one classification layer, and an output layer. The inputs of these DL networks are the CWT images in the database, while the outputs of these networks are different. The outputs of the 1st DL network are debonding shapes and the classification probabilities. The outputs of the extra DL network also include debonding shapes and classification probabilities. By comparing the classification probabilities of the 1st and extra DL networks, the known and unknown debonding shapes are determined. The outputs of the 2nd DL network are debonding and normal. By assembling the debonding/normal conditions at each inspection point, the debonding maps are plotted. In the DL setup, the initial learning rate is used to control the divergence and convergence of the DL learning result. A larger initial learning rate can reduce the training time and the number of epochs of the DL network, but the result may also be divergent. This study determines the initial learning rate as 0.01 to balance the convergence and the efficiency.

5.2 Database building: CWT image

This study uses the continuous wavelet transform (CWT) to plot the time-frequency scalogram that shows the time and frequency signal distribution. The CWT of a signal f(t) can be defined as [182-185]:

$$CWT_f = \int_{-\infty}^{\infty} f(t)\overline{\zeta_{a,b}}(t)\, dt, \qquad a > 0, b \in \mathbb{R} \tag{5.1}$$

The number a is the scale factor that dilates or compresses the signal, and the number b is the translational factor that translates the times. The CWT is a convolution of the original signal with a scaled and translated version of the mother wavelet. The convolution automatically defines the scale factor a and the translational factor [186]. $\overline{\zeta_{a,b}}(t)$ is the complex conjugate of the mother wavelet $\zeta_{a,b}(t)$, which can be written as:

$$\zeta_{a,b}(t) = \frac{1}{|a|^{\frac{1}{2}}}\zeta\left(\frac{t-b}{a}\right) \tag{5.2}$$

If the CWT respects the condition of the admissibility shown in Equation (5.3), the CWT is invertible:

$$C_\zeta = \int_{-\infty}^{\infty} \frac{|\xi(v)|}{|v|} dv < \infty \tag{5.3}$$

Where ξ is the Fourier transform of ζ, and

$$\int_{-\infty}^{\infty} \zeta(x) dx = 0 \tag{5.4}$$

The CWT can produce a maximum value at the natural frequency of the original signal, which corresponds to the natural frequency's time zone. As a result, the CWT can isolate the natural frequency from the frequency domain and identify the time when the signal reaches the natural frequency in the time domain. Then the time and frequency features of the signal after CWT can be determined by drawing a time-frequency scalogram, as shown in Figure 5.2(b). The x-axis shows the time, the y-axis shows the frequency, and the different colours correspond to different velocity magnitudes.

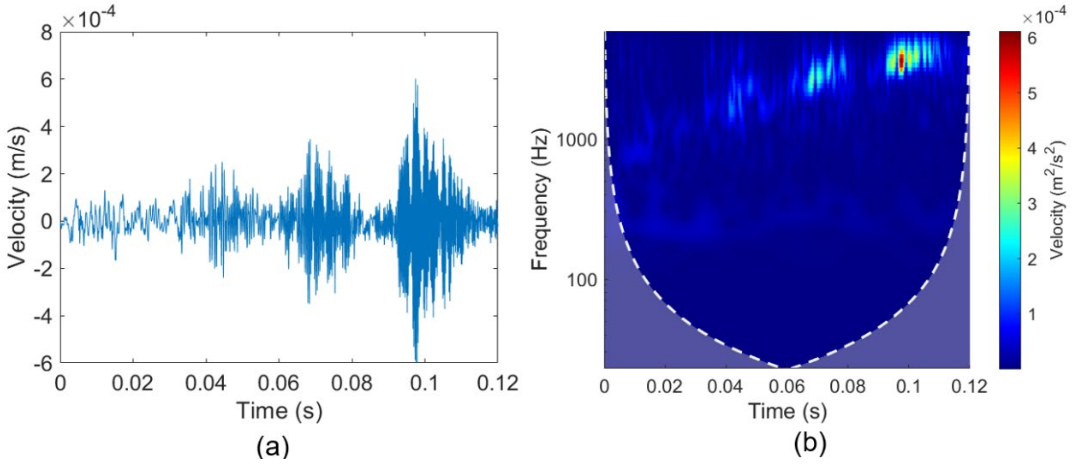

Figure 5.2 A representative to show (a) the time-domain signal and (b) the time-frequency scalogram at the inspection point (3,2)

During the CWT transform, the size of the scalogram image is set as 1280 × 1080 × 3 pixels (1280 pixels high, 1080 pixels wide, colour channel: RGB) to ensure the resolution. However, this size is too large for machine learning. The scalogram images are resized to 700 × 700 × 3 pixels so that computation resources can be reduced.

5.3 Two-stage debonding area identification method

The structure of this inspection method using DL is shown in Figure 5.3. In this method, thousands of vibration signals are transferred to time-frequency scalograms by CWT, then the scalograms collected from tiles with different debonding shapes are used to build a database. After that, in stage I, the 1st DL network is designed and trained to identify debonding types (different shapes). Then, in stage II, an extra DL network is trained to determine the classification probabilities of each shape. The scalograms collected from the inspection points on a tile to be inspected are set as the test group, and then the test group is input into the trained 1st DL network. The scalograms in the test group are classified into known/unknown groups based on the classification probabilities provided by the extra DL network. The classification procedure ends if the test scalogram is classified into the known shape. If the test scalogram is classified into an unknown shape, the 2nd DL network is designed and trained to identify conditions (debonding/normal). Then, 36 inspection points are deployed to the new tile to identify the debonding area. The number of inspection points is determined by balancing the inspection efficiency and inspection accuracy. The vibration signals are also transferred to the time-frequency scalograms by CWT. The scalograms collected at each point are defined as the test group of the 2nd DL network. Finally, each point is classified into debonding/normal, and the debonding area of this tile can be plotted. The newly identified debonding shape can also be added to the database to extend it and increase the prediction accuracy.

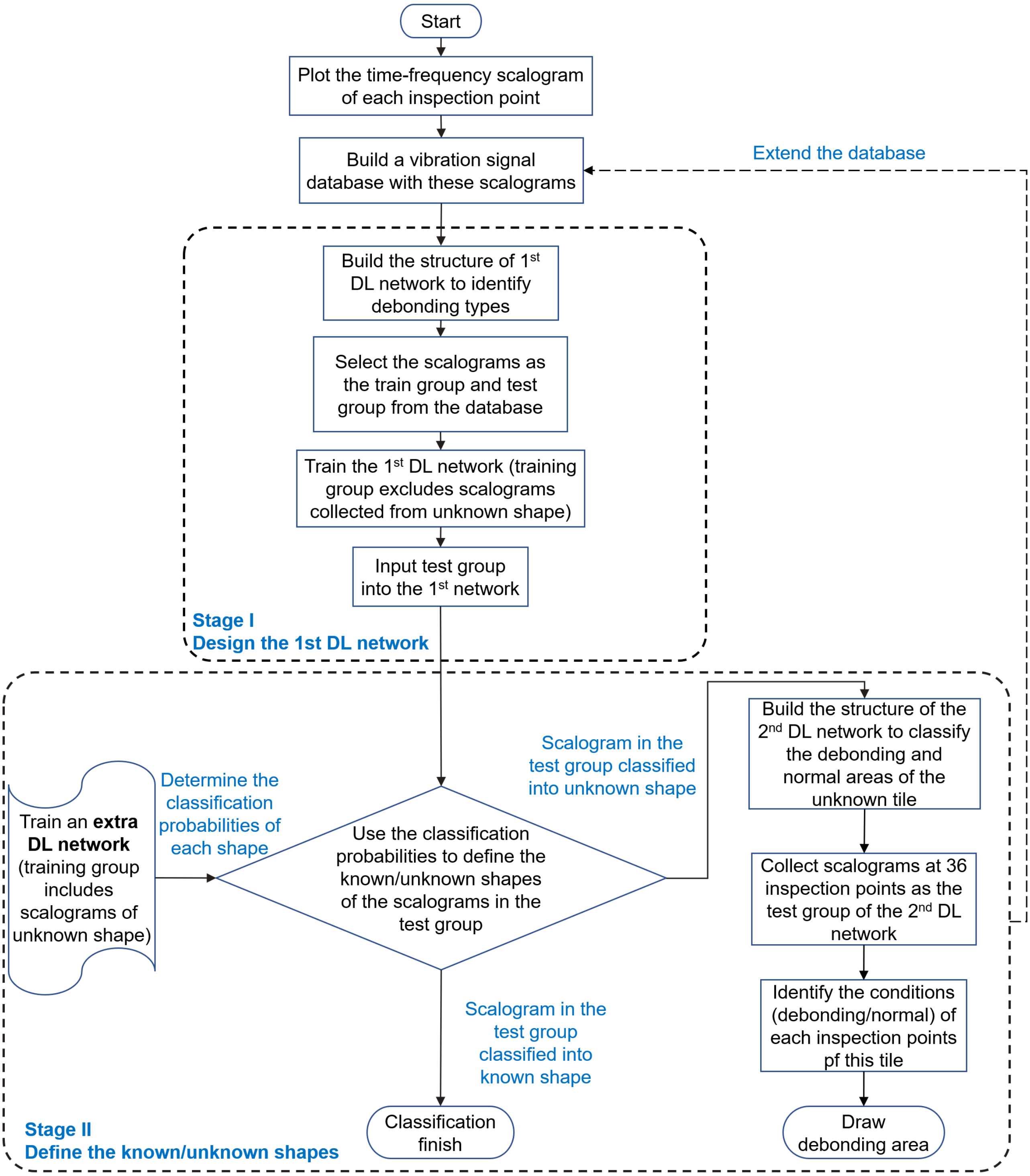

Figure 5.3 Flowchart for the fast non-contact inspection of tile debonding based on tuned acoustic wave and DL network

After resizing, the CWT scalograms are imported into the 1st DL network. The current database contains 1080 CWT scalograms. The proposed DL network is trained, then validated and tested. The scalograms are divided into training, validation, and testing groups. During the training, the validation keeps modifying the training character. 10% of 1080 scalograms are selected as the validation group to achieve stable performance, and 90% of 1080 scalograms are selected as the training group. The training group contains 972 scalograms, while the validation group contains 108 scalograms.

The tile can be considered as a symmetry object. Therefore, to reduce the inspection points and improve efficiency, the inspection points selected in the tile are inspection points 1, 2, 3, 8, 9, and 15, as shown in Figure 5.4, corresponding to 1/8 of the tile.

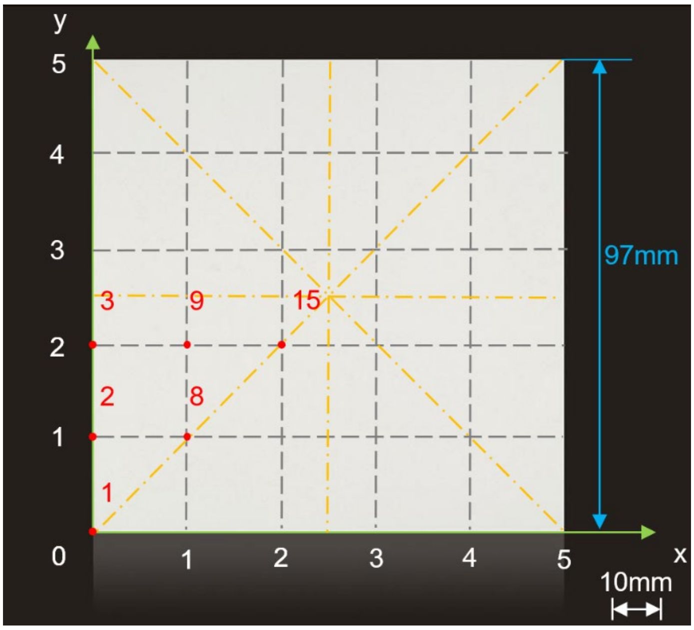

Figure 5.4 Inspection points selected for building the test group

In the 2nd DL network, the test group contains 36 scalograms collected at 36 inspection points on the tile with an unknown debonding shape.

In this study, one of the debonding groups is selected as an unknown shape. For example, the corner debonding group is moved out of the database and defined as an unknown shape, as shown in Figure 5.5. The test group contains two known shapes and one unknown shape, including circle debonding/normal, half debonding/normal, and corner debonding/normal. Eighteen time-frequency scalograms are selected as the test group in the 1st DL network. The three DL networks used in this study have different classification layers. For the 1st DL network and the extra DL network, the scalograms inputted will be classified into ten categories (square normal/debonding, triangle normal/debonding, half normal/debonding, circle normal/debonding, normal, unknown), including five known different debonding shapes (square, triangle, half, circle, normal) and one unknown debonding shape. For the 2nd DL network, the scalograms are divided into debonding and normal.

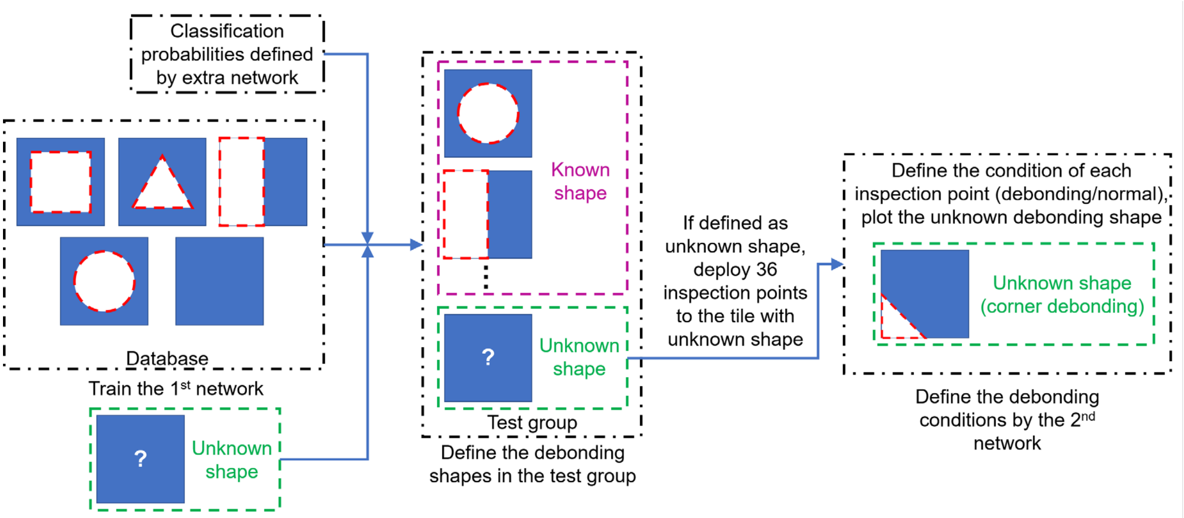

Figure 5.5 Schematic diagram of the specific inspection procedure

If a scalogram in the test group is defined as unknown in the 1st DL network, 36 inspection points should be deployed on the surface of the unknown tile. The scalograms collected from these inspection points are imported into the 2nd DL network. The 2nd DL network has exactly the same structure as the previous one. The only difference is the classification layer. In the classification layer, the scalograms on 36 inspection points are classified into two groups: debonding/normal. Then the debonding points are defined as 1, and the normal points are defined as 0, and the debonding shape can be plotted on a debonding map. After defining the debonding shape of the unknown tile, the signal can be classified and added to the database to extend it.

5.4 Structure of the deep learning network

The DL networks used in this study have the same structure. The structure of these DL networks is shown in Figure 5.6.

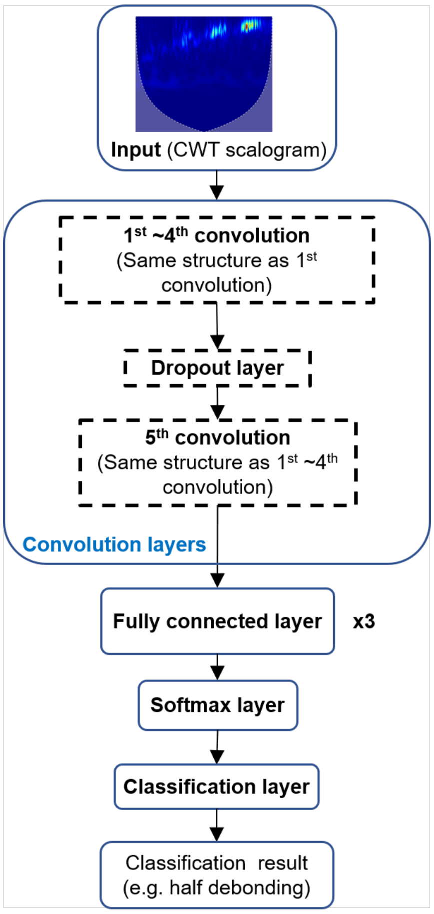

Figure 5.6 Structure of the convolution network for tile debonding inspection using the DL method

As shown in Figure 5.6, the DL network used in this study contains five convolutions. The input of the DL network is the CWT scalogram. Then the scalogram is passed to the first convolution. The structure of the convolution is shown in Figure 5.7.

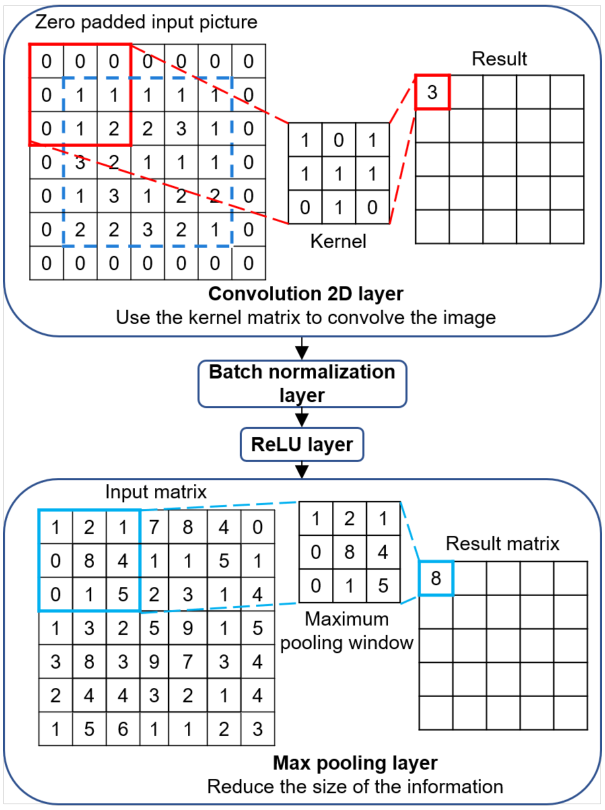

Figure 5.7 Structure of the convolution network

During the convolution, the size of the raw matrix (feature map) will be reduced. As a result, the Convolution 2D layer in the first convolution is set as “zero-padding” to maintain the size of the input feature map. As shown in Figure 5.7, an outer layer of zero values is added to the input scalogram image framed by the blue box. Then the scalogram image is divided into three channels (Red, Green, and Blue channels). Each channel has a specific kernel matrix. The parameters in the kernel matrix vary during the training procedure. Then the result matrix is passed to the Batch normalisation layer. This layer can enhance the stability of the network and shorten the training time. After the Batch normalisation layer, a non-linear activation function layer named Rectified Linear Unit (ReLU) layer is added to the network. This layer can map the linear output of the convolution layer to a non-linear output. Compared with linear activation, the features of the nonlinear activation function learned can be more complex [187]. The equation of ReLU can be written as:

$$f(s) = \begin{cases} s & \forall s > 0 \\ 0 & \forall s \leq 0 \end{cases} \tag{5.5}$$

As shown in Equation (5.5), if the input s is positive, the output remains the received input s. If the input s is negative, the output becomes zero. Compared with commonly used activation functions such as sigmoid, the ReLU function can process more gradient information across several layers deep [188].

All the convolutions ended with a max pooling layer. This layer can reduce the size of the information, improving computing efficiency. As shown in Figure 5.7, the size and stride of the maximum pooling window are predetermined. The maximum value within the window is extracted and then formed into a new matrix.

Then, in the 5th convolution, a dropout layer is placed before the 2D convolution layer, as shown in Figure 5.8. In the dropout layer, the input element is set to zero randomly based on a predetermined probability. This layer is used to prevent overfitting.

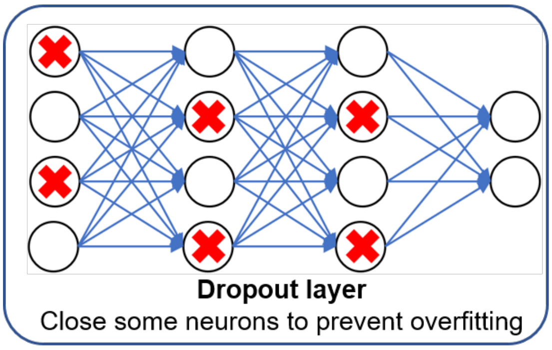

Figure 5.8 Structure of the dropout layer

After convolution, three FC layers are set in the network. The structure of each FC layer is shown in Figure 5.9.

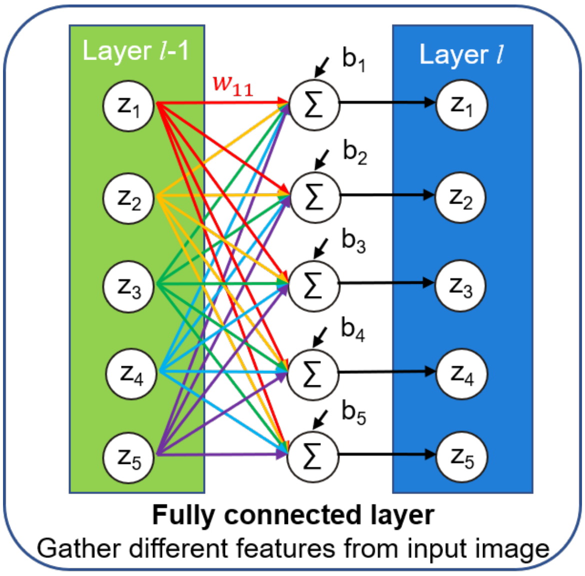

Figure 5.9 Structure of the FC layer

Every neuron in the FC layer is connected to all neurons in the previous layer [189]. A linear transformation is applied to the input through a weight matrix. The equation can be written as:

$$v^l = \sum_{j=1}^{m} c_i^{l-1} \omega_{ij}^{l-1} + d^{l-1} \tag{5.6}$$

where v is the output vector in the layer l, m is the number of neurons in the layer l-1, ω_{ij}^{l-1} is the connection weight between layer l-1 and layer l, c_i^{l-1} is the ith activated neuron value in the layer l-1, and d is the bias value in the layer l-1. In this network, three FC layers can gather different features from different positions in the raw picture. Feature maps generated by convolution layers are based on linear filters. Thus, the capability of solving nonlinear problems is lacking. Therefore, multi-FC layers are used to apply a non-linear transform to the features [190].

After the fully connected layer, a softmax layer is placed to generate the probability of each category. The equation can be written as:

$$softmax(y)_i = \frac{e^{y_i}}{\sum_{j=1}^{n} e^{y_j}} \tag{5.7}$$

Where y_1, y_2, … , y_n are the n outputs of the fully connected layer. As shown in Equation (5.7), all the probabilities are decimals between 0 and 1, and these decimal probabilities must add up to 1.

Finally, the input picture is classified into the category with the maximum probability in the classification layer. In the meantime, the classification layer also calculates the cross-entropy loss for classification, as shown in Equation (5.8).

$$loss = -\frac{1}{N}\sum_{n=1}^{N}\sum_{i=1}^{K} w_i r_{ni} \ln p_{ni} \tag{5.8}$$

Where N is the number of signals, K is the number of classification classes, w_i is the weight for category i, r_{ni} is the indicator for which the nth sample belongs to the ith class, and p_{ni} is the probability for signal n for category i, which is the output of the softmax layer. The cross-entropy loss describes the difference between the prediction and the target. The accuracy of the DL network will increase with the reduction of cross-entropy loss. The backpropagation in the DL network will reduce the cross-entropy loss by updating weights and biases in the DL network.

5.5 Debonding identification with a trained deep learning network

In this study, the classification probability is used to identify the known and unknown groups. As mentioned in Figure 5.6, before the classification layer, there is a softmax layer that can generate the classification probability of each category. The classification progress is generated based on these probabilities. The input will be classified into the category with the maximum classification probability. In a well-trained DL network, the maximum classification probabilities of each test input should be relatively high. However, if a scalogram collected from the unknown debonding shape is input into the trained network, since the features of the unknown scalogram are different from each known scalogram, different categories may have similar classification probabilities. As a result, the classification probability will disperse. Hence, the maximum classification probability will be reduced. Therefore, a probability threshold is required to distinguish known shapes from unknown ones.

At first, an extra DL network is trained. The structure of the extra DL network is exactly the same as the 1st DL network. The difference is in the test group. The test group only includes the known shape in the extra DL network. 10% of the scalograms in the database are selected as the validation group, 10% of the scalograms are selected as the test group, and 80% of the scalograms in the database are selected as the training group. The training result of the extra DL network is shown in Figure 5.10. The accuracy of this network is over 95%.

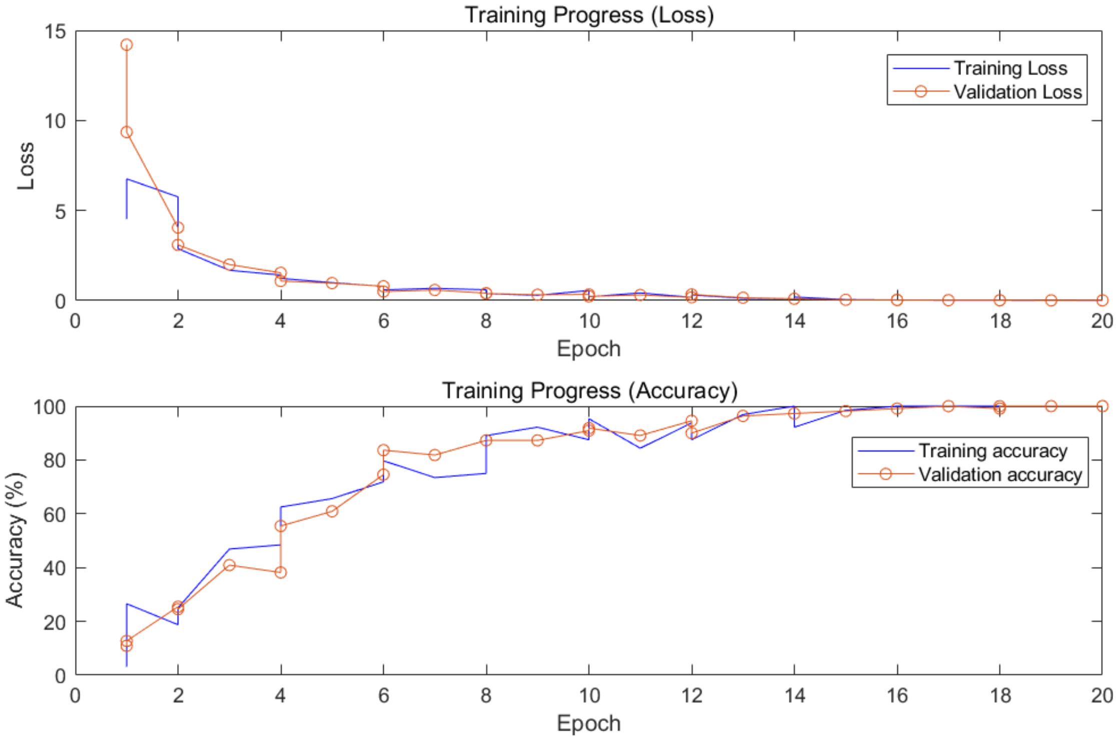

Figure 5.10 The accuracy and the loss of the DL network

After the training process, the predetermined test group is used to assess the trained network. In the DL network, the confusion chart is commonly used to assess training accuracy. The confusion chart of this network is shown in Figure 5.11. The left side corresponds to the true class, while the bottom side corresponds to the predicted class. As shown in Figure 5.11, scalograms are seldom misclassified.

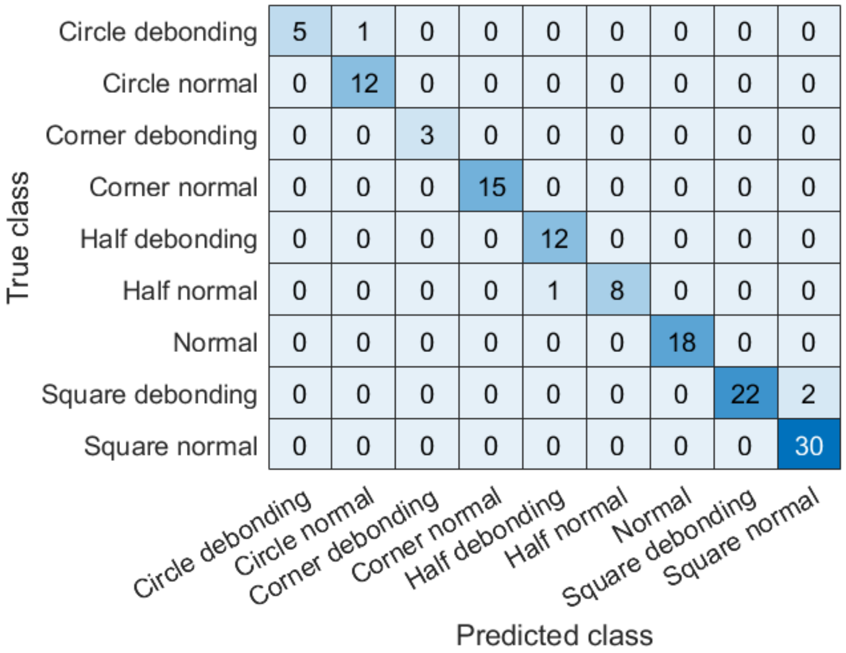

	Circle debonding	Circle normal	Corner debonding	Corner normal	Half debonding	Half normal	Normal	Square debonding	Square normal
Circle debonding	5	1	0	0	0	0	0	0	0
Circle normal	0	12	0	0	0	0	0	0	0
Corner debonding	0	0	3	0	0	0	0	0	0
Corner normal	0	0	0	15	0	0	0	0	0
Half debonding	0	0	0	0	12	0	0	0	0
Half normal	0	0	0	0	1	8	0	0	0
Normal	0	0	0	0	0	0	18	0	0
Square debonding	0	0	0	0	0	0	0	22	2
Square normal	0	0	0	0	0	0	0	0	30

Figure 5.11 Confusion chart

In practice, the debonding shape may be various and different from the predefined typical types as the known shape in this study. Therefore, it is also very necessary to identify the unknown debonding shape when subjected to practical applications. As shown in Figure 5.12(a), all the 120 maximum classification probabilities in the test group are over 98% in the extra DL network. Therefore, 98% is defined as a threshold to evaluate the known and unknown of the input scalogram. All the 20 classification probabilities in the test group in the 1st DL network are compared with the threshold. As shown in Figure 5.12(b), after setting the threshold, the test scalograms in the 1st DL network can be classified into the known group and the unknown group. Most of the corner debonding scalograms are defined as the unknown group, but one corner debonding scalogram is misclassified into the known group as well. The accuracy of the prediction is 94.4%.

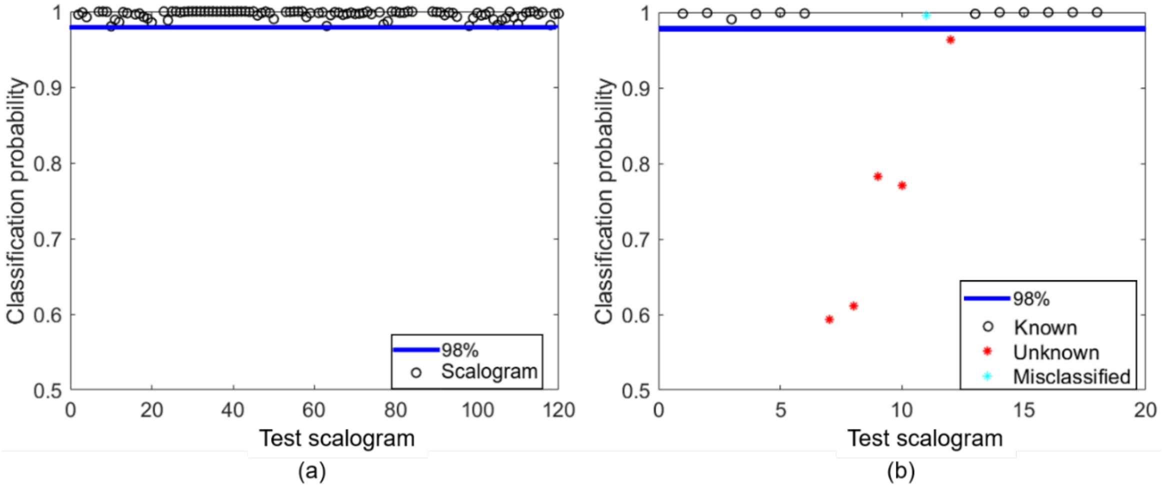

Figure 5.12 Classification probabilities versus test scalograms based on (a) the extra DL network and (b) 1st DL network

After defining the unknown group, 36 inspection points are deployed on the surface of the tile. These time-frequency scalograms collected at 36 inspection points on the tile with a corner debonding area are selected as the test group. Then the 2nd DL network is used to predict the signals collected from the tile with a corner debonding. The data processing progress is exactly the same as the previous method in the 1st DL network. The result of the simulation network is shown in Figure 5.13(a). The accuracy of this network is over 95%. The confusion chart of this network is shown in Figure 5.13(b). Only two points are misclassified.

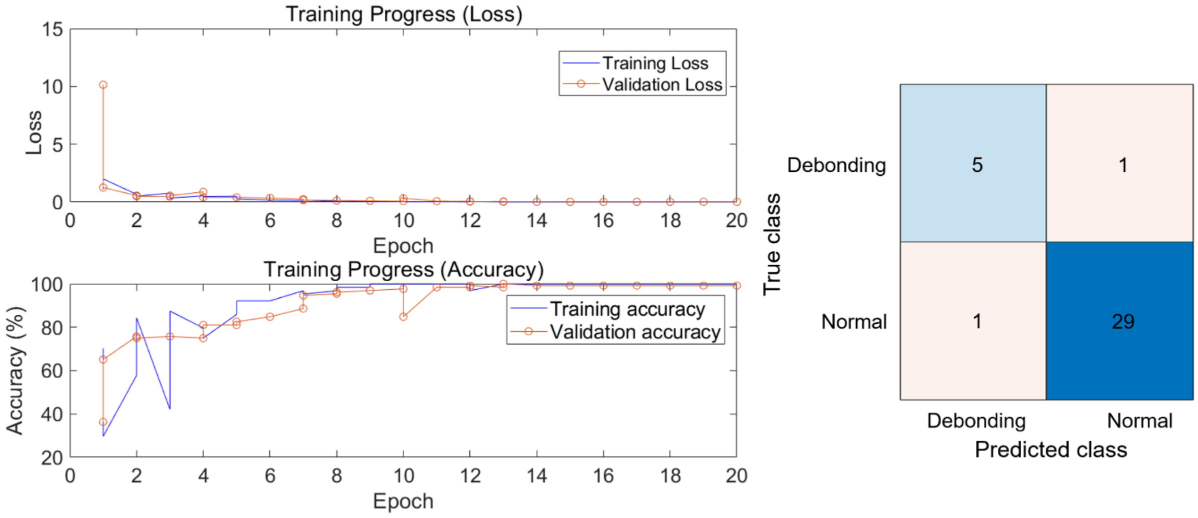

(a)

(b)

Figure 5.13 (a) The accuracy and the loss of the network (corner) (b) confusion chart (corner)

After training, the scalograms collected from the tile with the corner debonding area are classified into different types. The debonding point is defined as 1, and the normal point is defined as 0. Then the debonding conditions of 36 inspection points are plotted on a debonding map, which is shown in Figure 5.14.

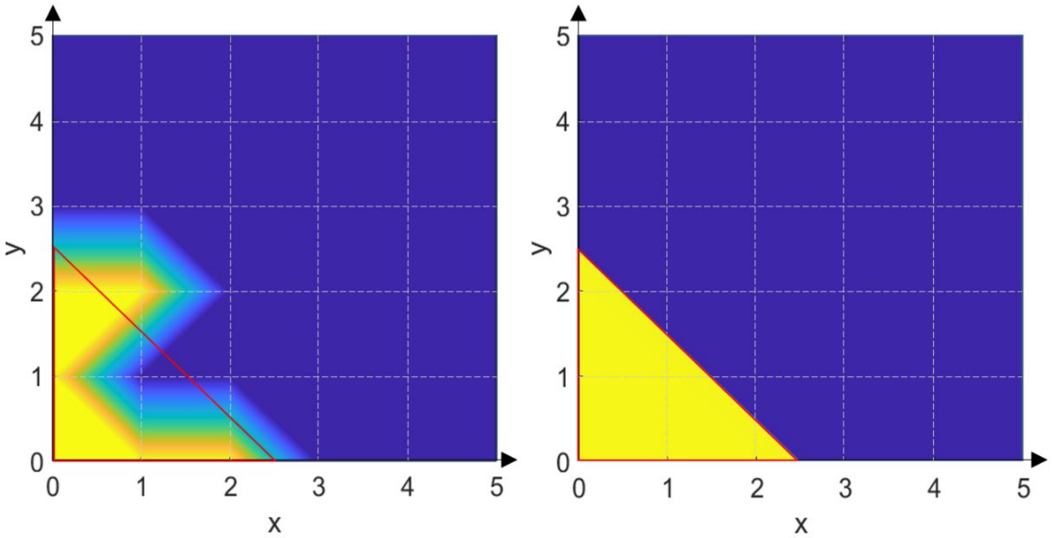

(a)

(b)

Figure 5.14 Debonding map of the tile with a corner debonding area between (a) the inspection result and (b) ideal result

Figure 5.14(b) is the expected ideal result. The debonding area is clearly shown. However, Figure 5.14(a) is the predicted result. Though the accuracy of the model is over 95%, the predicted result is still not clear enough, but this method can generally inspect the shape of the debonding area. In Figure 5.14, the debonding area of the ideal result is 1606.49 mm^2, while the debonding area of the predicted result is 1533.46 mm^2. Therefore, the prediction error is -4.857%.

Then the tile with half debonding area is also set as the test group to prove the effectiveness of this method. The accuracy is also over 95%, as shown in Figure 5.15(a). The confusion chart of this network is shown in Figure 5.15(b). Seven points are misclassified.

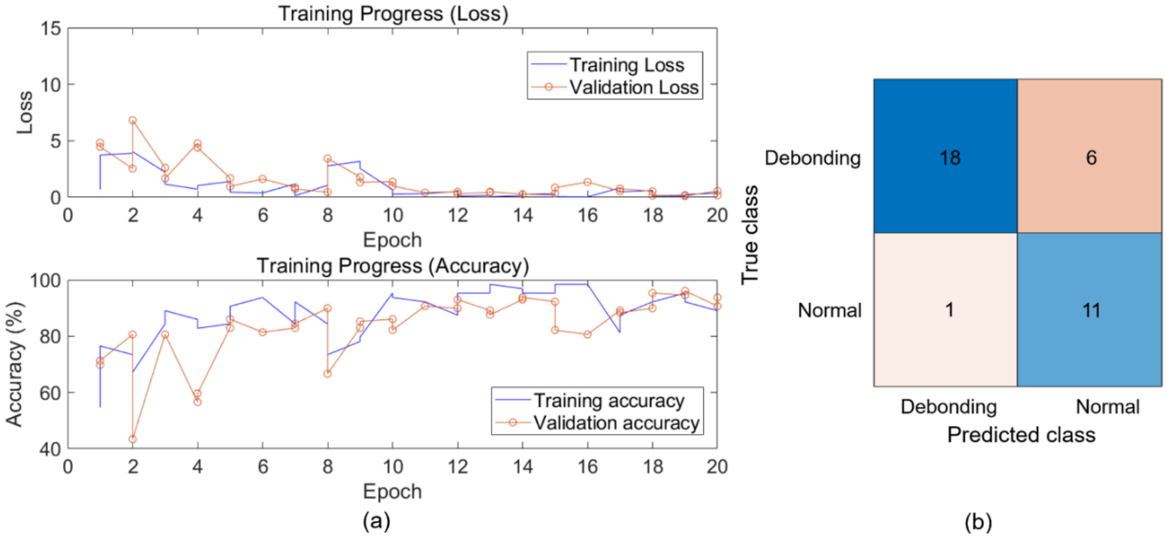

Figure 5.15 (a)The accuracy and the loss of the network (half) (b) confusion chart (half)

After training, the scalograms collected from the tile with half debonding area are classified into different types. Similar to the corner debonding, the debonding point is defined as 1, and the normal point is defined as 0. The debonding conditions of 36 inspection points are plotted on a debonding map. The results are shown in Figure 5.16. As shown in Figure 5.16, though 7 points are misclassified, the profile of the debonding shape can still be plotted. In Figure 5.16, the debonding area of the ideal result is 4704.5

mm^2, while the debonding area of the predicted result is 4629.82 mm^2. Therefore, the prediction error is 1.588%.

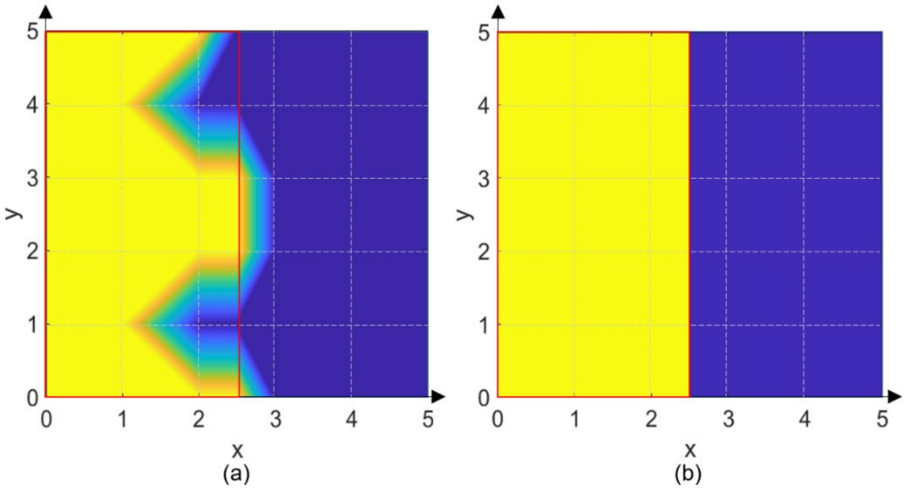

Figure 5.16 Debonding map of the tile with a half debonding area (a) predicted result (b) ideal result

Similarly, the circle debonding area, the triangle debonding area and the square debonding area are also set as unknown groups to test the feasibility of inspecting different debonding shapes with this method. The errors of these predictions are calculated by debonding area as mentioned above. The errors of the predictions in different debonding shapes are summarised in Table 5.1.

Table 5.1 Error analysis of different debonding shapes

Debonding shape	Prediction error
Square	30.38%
Triangle	29.75%
Circle	21.26%
Half	1.588%
Corner	-4.857%

As summarised in Table 5.1, the half-debonding area has the lowest predicted error.

5.6 Summary

In this chapter, a novel method for fast non-contact inspection of tile debonding based on tuned acoustic wave and a deep learning network is designed to identify the tiles' debonding, improving the inspection procedure's efficiency.

The vibration is excited by an acoustic wave of a sweeping frequency band, and a laser Doppler vibrometer collects the vibration signal. The databases are built by using time-frequency scalograms transferred from these vibration signals. A two-stage debonding shape-identifying method is established to identify the debonding type of the tile step by step. The 1st DL network and the extra DL network are developed to determine the known/unknown shape of the debonding area. The identifying accuracy is 100%. 36 inspection points will be deployed to the tiles identified as unknown debonding shapes, and the 2nd DL network will be developed to identify each inspection point's debonding/normal condition. Then the debonding area of the tile can be constructed into a contour map. The prediction error of the unknown debonding with different shapes is about 1%~31%. Based on the experiment, the classification result of this two-stage debonding shape-identifying method correlates well with the actual condition, proving the effectiveness of this method. The database can also be extended to decrease prediction errors.

This method is suitable and efficient for inspecting debonding tiles. Tiles with known shapes only require one inspection point. With more tiles to be inspected, the database can also be extended. These additional data can subsequently be used to train deep learning networks, enabling the two-stage method to progressively improve its detection accuracy during practical deployment. Nevertheless, it should be noted that a larger database inevitably requires more data samples, and the accuracy of the deep learning model remains contingent upon the size and diversity of the database. This method can be uploaded to an unmanned aerial vehicle (UAV) to inspect dozens of tiles at a time, which will be more efficient in monitoring tile debonding.

Chapter 6: Inspecting the loose slot wedge on the stator of a hydro-generator

As mentioned in previous chapters, the feasibility of the non-contact acoustic method has been demonstrated in inspecting tile debonding. The debonding area can be considered as a void within the adhesive layer, which means the approach can be extended to similar practical inspection tasks, such as the inspection of fittings or other bonded interfaces. As a result, the looseness of the slot wedge within the hydropower generator is extended to judge the feasibility of the non-contact acoustic method.

With the increasing public awareness of environmental issues, more and more research and applications are being conducted in the field of green energy. Hydropower generation represents the world's largest source of green energy, fulfilling nearly 16% of global electricity demand [191, 192]. The International Renewable Energy Agency suggests that 850 GW more energy generation capacity should be fulfilled by hydropower to limit global temperature increase below 2 °C [193]. Hydropower generation units (HGUs) convert the potential energy of flowing water into electrical energy [194]. The hydroelectric generator is the core component of all HGUs, and its operating condition directly determines the power supply capability of the hydropower station [195, 196].

Many hydro-generators have been in operation for decades, and their operating conditions have significantly deviated from the original design specifications [197]. These changes in operating conditions will result in defects within the generator. During operation, the alternating electromagnetic force induces vibration in the stator winding bars beneath the slot wedges. Continuous vibration can cause the stator slot wedges to gradually loosen. If the wedges do not remain tight within the stator slots, the coils and bars may also shift [198]. As a result, regular inspection and timely maintenance of the generator are indispensable. Previous studies have identified winding looseness as a primary cause of stator winding failures [85, 199, 200]. Looseness exacerbates vibration, accelerating the corrosion and wear of the insulation material on the winding bars, which can lead to serious accidents [201]. Many hydropower stations have incurred substantial maintenance costs and downtime for generator repairs, resulting in significant economic losses [202]. Thus, ensuring the tightness of stator wedges is critical for maintaining stable long-term operation. The timely detection of the stator wedge loosening is imperative [203].

Currently, the loosening detection primarily relies on contact-based methods. Experienced operators assess the severity of loosening by tapping the wedge with a hammer and interpreting the resulting sound [204]. However, this approach is subjective and depends heavily on the operator's skill. Consequently, automated inspection methods are being developed. Pistone et al. [205] designed an automated robotic vehicle that can move on ferromagnetic surfaces. Multiple plug-and-play sensors can be added to the vehicle to proceed with the inspection. Jeon et al. [206] developed a robotic vehicle with a robotic arm that loaded a wedge tightness test module. However, this method requires the rotor to be removed, as the robotic arm needs ample space to operate. Ekkachai et al.[207] proposed an inspection method using a robot that does not require rotor removal. Their robot employs a tapper head and an accelerometer sensor to detect loosening, with the acceleration signal amplitudes used for evaluation. Xie et al. [85] designed an offline detection system for inspecting wedge loosening when the generator is stopped, eliminating the need to disassemble the stator or rotor. An inspection robot taps the wedge, and the loosening condition is assessed by analysing the percussion sound signal.

Nevertheless, deploying contact inspection systems within the narrow confines of a generator is challenging. Moreover, the movement of the contact inspection equipment may also aggravate the loosening of the wedge. Therefore, the non-contact inspection method is developed. Various non-contact techniques exist to generate non-contact inspection, including mechanical, physical, electrical, chemical, and even visual inspection [35, 36]. Different approaches to non-contact inspections have their own advantages and limitations. Li et al. [208] analysed infrared monocular visual images of stator and rotor profiles to inspect the air gap between the stator core and rotor magnetic poles. However, this method assesses the overall stator core condition and cannot identify the loosening of specific wedges. Han et al. [209] monitored the condition of magnetic wedges by analysing negative-sequence information extracted from three-phase voltage and current data of the motor. Yet, this approach is only applicable to slot wedges made of magnetic materials.

To address these limitations, this study develops a non-contact inspection method utilising a tuned acoustic wave.

6.1 Inspection during outage maintenance of the hydro-generator

Traditional methods require direct contact. Although sound signals can be collected remotely using a microphone, the sound itself is generated by striking the slot wedge with an impact hammer [85], which still involves contact. In practice, the gap between the stator and rotor is typically only about 32 mm, making contact inspection difficult due to the limited space. Thus, a non-contact inspection method is necessary. In this study, the slot wedge is excited remotely using a directional speaker, and the vibration signal is collected remotely using a Laser Doppler Vibrometer (LDV). A schematic of this method is shown in Figure 6.1.

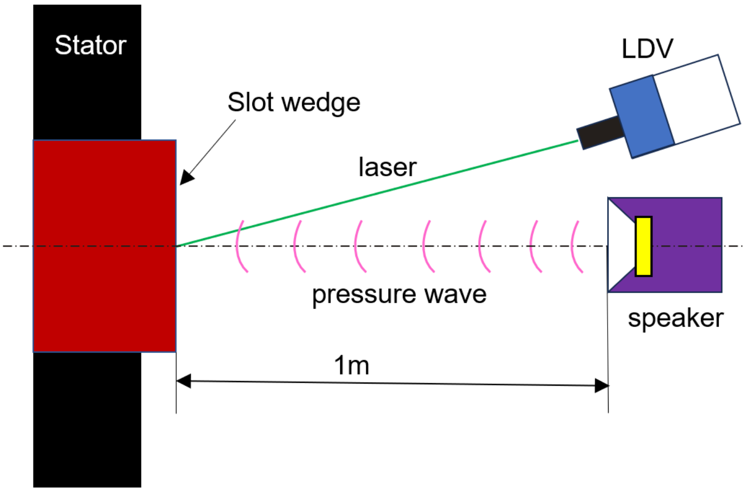

Figure 6.1 Sketch of the non-contact acoustic inspection method used in this study

During operation, a loose slot wedge may be partially ejected from the slots between the stator teeth, jeopardising the generator's longevity. Looseness alters the vibration mode of the wedge, resulting in different resonance frequencies compared to a normal wedge. This principle forms the basis for detection. The excitation signal is chosen as a frequency sweep to identify the resonance frequency, as shown in Figure 6.2. The sweep signal covers a frequency range of 200–4000 Hz, encompassing the first resonance mode. It consists of 20 different frequencies with a modulation interval of 200 Hz. Each frequency step lasts 60 ms, and the input amplitude to the speaker is 5 V.

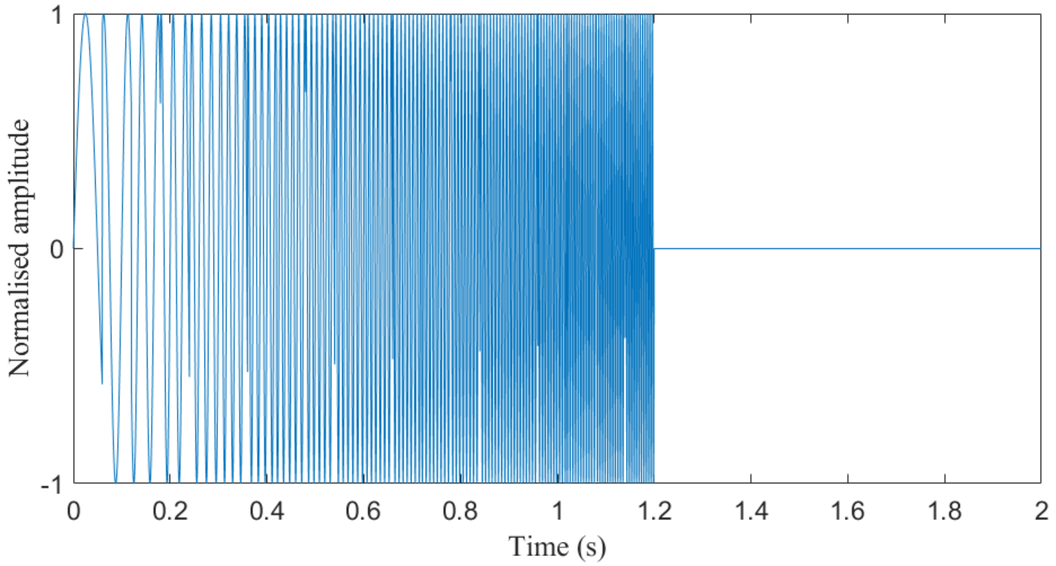

Figure 6.2 Waveform of the sweep signal

For the experiments, slot wedge samples were obtained from a generator provided by the Gezhouba Hydropower Station, as shown in Figure 6.3(a). An experienced technician classified and labelled the wedges as loose, normal, or intermediate (middle) by tapping them with an impact hammer. Nine slot wedges were analysed in total: three loose, three intermediate, and three normal.

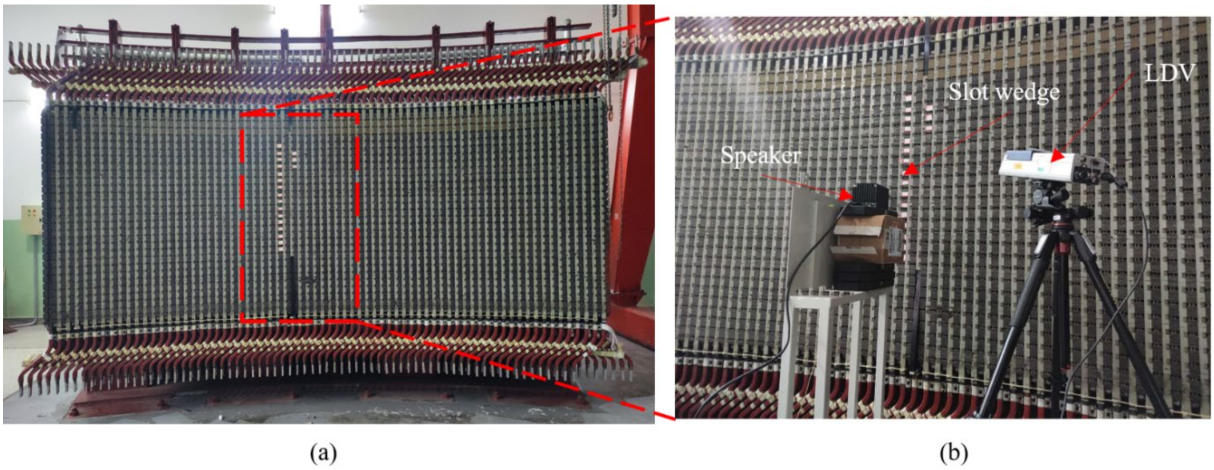

(a) (b)

Figure 6.3 (a)Slot wedges on the hydropower generator (b) Experiment setup

Then the experiment setup is shown in Figure 6.3(b). The slot wedge is excited by the sound wave that the directional sound speaker generates. The vibration signal on the surface of the slot wedge is collected and recorded by the LDV equipment.

6.2 Non-contact detection of loose slot wedge

In practice, signals are collected in a noisy environment where other equipment operation contributes background noise. Consequently, the vibration signals acquired by the LDV also contain noise.

To address this, an algorithm named Multi-Window Spectral Estimation (MWSE) is employed [85]. This method uses multiple orthogonal data windows to compute the direct spectrum of the sample data and then averages these spectra to obtain a final estimate. The accuracy of the MWSE method is higher than that of the periodogram method, and the variance of the raw signal is also reduced. The equation of the MWSE is given by:

$$S^{mt}(\omega) = \frac{1}{L}\sum_{k=0}^{L-1} S_k^{mt}(\omega) \quad k = 1,2,\cdots,L \tag{6.1}$$

Where L is the number of the window, $S_k^{mt}(\omega)$ is the spectrum of each orthogonal data window, and ω is the frequency. Compared with the traditional period graph method, this method reduces the variance from the raw data, and improves the accuracy. The raw signal collected by the LDV equipment is shown in Figure 6.4(a).

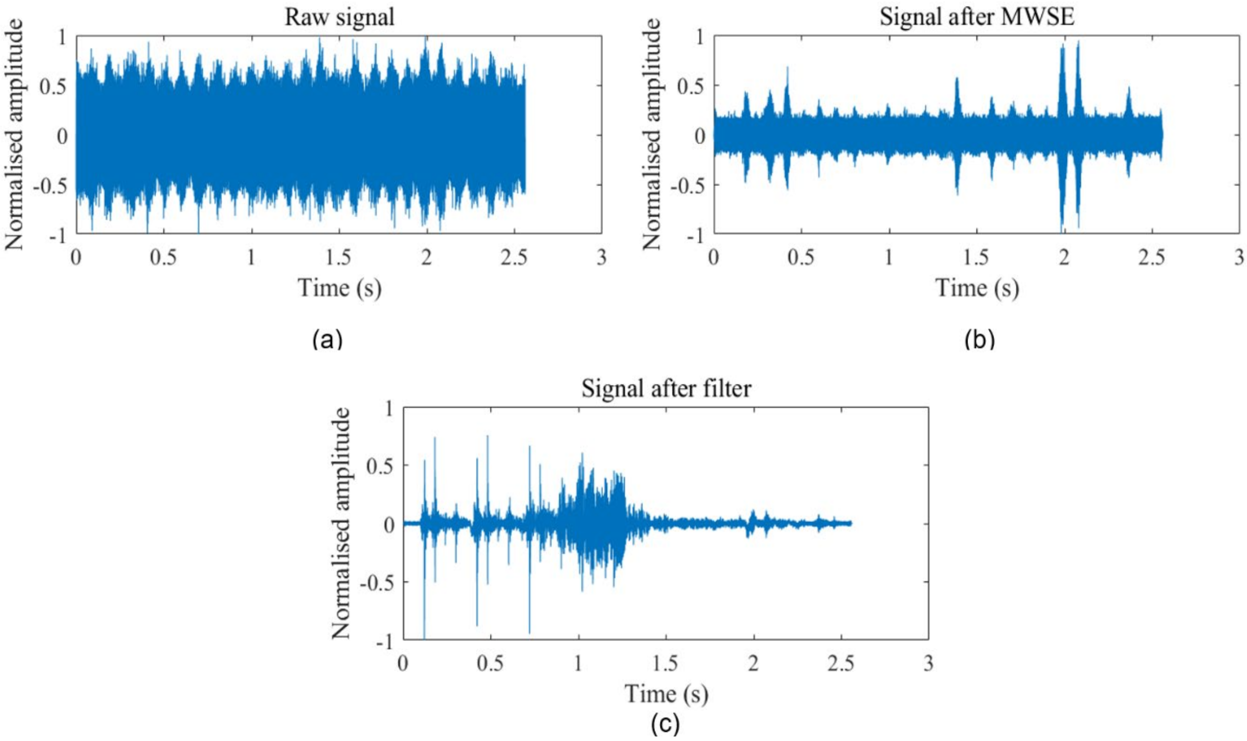

(a) (b) (c)

Figure 6.4 (a) Raw signal (b) Signal after MWSE (c) Signal after MWSE and filters

As shown in Figure 6.4(a) and (b), though the MWSE method removed most of the noise, there is still background noise and zero drift. Therefore, the high-pass and low-pass filters are required. The well-experienced operators can identify the looseness by the sound of a hammer knocking, which means the response frequencies of the slot wedge can be limited to the audible range of the human ear, which is 20~20kHz [210]. According to the previous study, the resonance frequencies of the slot wedge vary from 2000Hz to 8000Hz [211]. This study’s frequency range is correspondingly expanded to 0~10kHz to cover more information. Additionally, the speaker's frequency range in this study is 135Hz~17kHz. The frequency range is finally defined as 200Hz to 10kHz to protect the speaker. Then, a low-pass filter and a high-pass filter are used to limit the signal frequency to 200~6000Hz. Figure 6.4(c) shows the vibration signal after the filters.

In practice, the sampling time of the system is much longer than the duration of the burst signal to obtain a completely exciting signal. Therefore, the start time of the signal is not easy to identify. Therefore, the signal collected will contain the data without an exciting signal.

Therefore, the short-time energy entropy ratio is used to isolate the valid signal fragment from the raw signal. The vibration signals generated by the burst signal are generally continuous, non-stationary signals. In data processing, a 10-30 ms non-stationary signal can be considered as a stationary signal. Therefore, the Hamming window can be used to frame and window the raw vibration signal. The signal is divided into short-term signals by the Hamming window. The short-term energy EL_i of each short-term signal can be described as:

$$EL_i = \log\left(1 + \frac{\sum_{m=1}^{N} x_i^2(m)}{a}\right) \tag{6.2}$$

Where N is the length of the signal, xi(m) is the vibration signal of the i frame after the window is added, and a is a constant that alleviates the signal. The energy of the signal is mainly defined by the magnitude of the amplitude.

The short-term spectral entropy Hi of each frame of the percussion sound signal is defined as:

$$H_i = -\sum_{l=0}^{N/2} p_i(k) \log p_i(k) \tag{6.3}$$

Where $p_i(k)$ is the spectral probability density function, the equation of pi(k) can be written as:

$$p_i(k) = \frac{Y_i(k)}{\sum_{l=0}^{\frac{N}{2}} Y_i(l)} \quad k = 0,1,\dots,\frac{N}{2} \tag{6.4}$$

Here, $Y_i(k)$ is the discrete Fourier transform result of xi(m). , representing the energy spectrum of the frequency component of each spectral line.

Then the entropy ratio EEF_i is then calculated using Equation (6.5):

$$EEF_i = \sqrt{1 + \left|\frac{EL_i}{H_i}\right|} \tag{6.5}$$

Based on the entropy ratio, the start time of the effect signal can be defined. Using MATLAB to transfer the signal after filtering to the short-time energy entropy ratio, the result is shown in Figure 6.5. The maximum value of the entropy ratio is defined as Er_{max}. The raw signal contains a leading segment, which is considered to be a noise segment. The mean value of the lead segment is defined as e_{th}. The start time of the effect signal can be considered as an abrupt increase in the short-time energy entropy ratio. The threshold Det of the abrupt increase is defined as:

$$Det = Er_{max} - e_{th} \tag{6.6}$$

Then the judgement interval (T1~T2) is then selected using Equation (6.7):

$$\begin{cases} T_1 = 0.05Det + e_{th} \\ T_2 = 0.1Det + e_{th} \end{cases} \tag{6.7}$$

Finally, the FrameTime function in MATLAB is used to define the start time between T_1 and T_2. Similarly, the end time is also defined. The start time and the end time of the valid signal fragment are shown in red and blue lines respectively, in Figure 6.5.

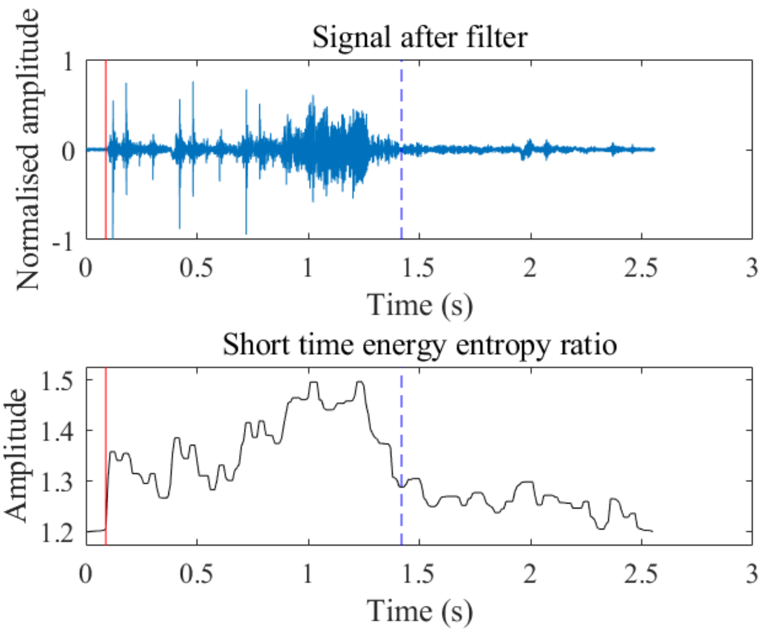

Figure 6.5 Isolate the valid signal fragment

The length of the valid signal fragment identified in Figure 6.5 is 1.36 seconds. This segment is then transformed from the time domain to the frequency domain using the Fast Fourier Transform (FFT). The result is presented in Figure 6.6.

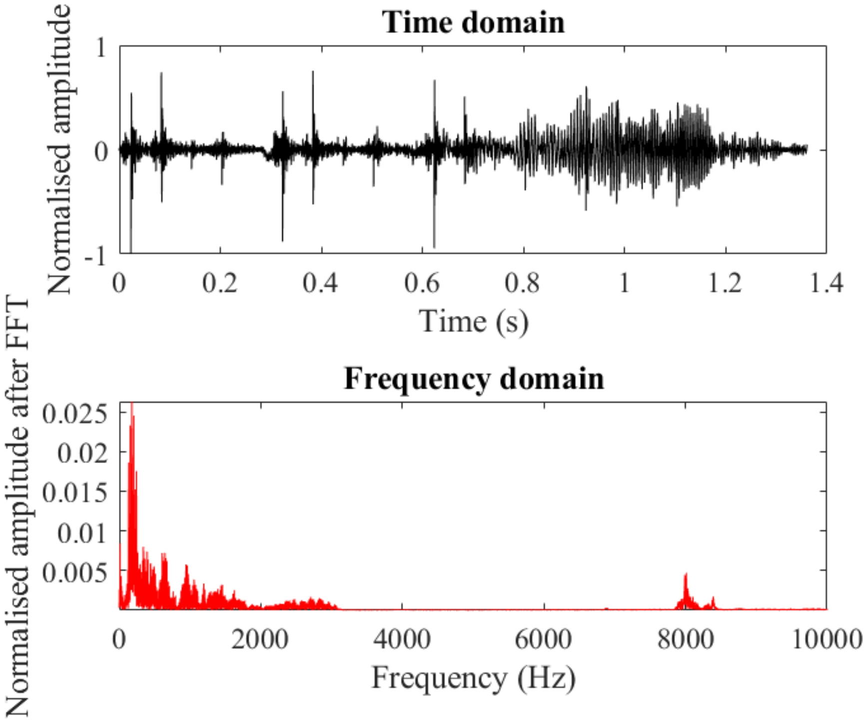

Figure 6.6 Time domain and frequency domain

6.3 Slot wedge condition identification

First, the repeatability of the experiment was assessed. As shown in Figure 6.7, five repeated experiments conducted at the same point (Point 10) show good consistency in both the time domain and frequency domain. However, some minor curve discrepancies remain in the time domain, whereas the frequency domain exhibits higher consistency. Therefore, the frequency domain is used for subsequent analysis to differentiate between loose and normal signals.

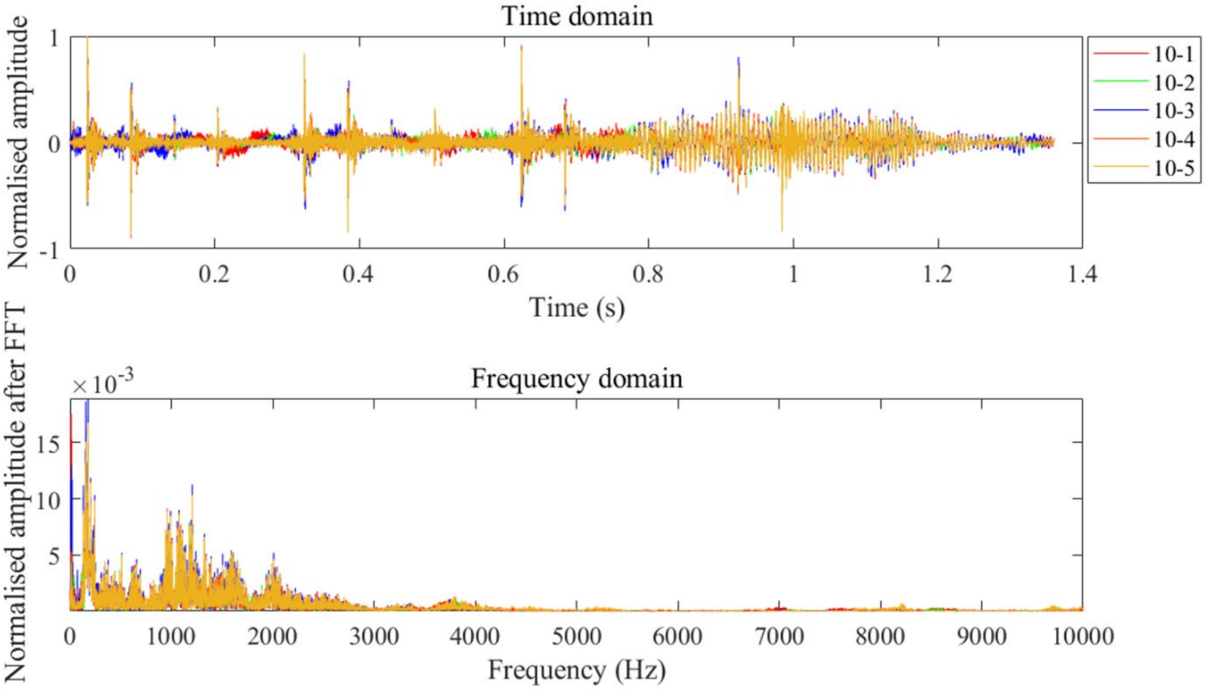

Figure 6.7 Five repeated experiments conducted at Point 10

The vibration amplitude is relatively small at frequencies above 3000 Hz, as observed in Figure 6.7. Consequently, the analysis frequency range is limited to 300–3000 Hz.

The traditional method of using a hammer to knock the sample is based on the change in the knocking sound. The loose wedge and the normal wedge have different responses to the knocking. Similarly, this method compares the resonance peak of the loose wedge and the normal wedge. As shown in Figure 6.8, the signal repeatability of the normal is very good. However, the signals of the middle wedge and the loose wedge are different. This is because the normal wedge can be considered a standard status, while the middle and loose wedges are not fixed statuses. Different degrees of debonding will result in different vibration waveforms.

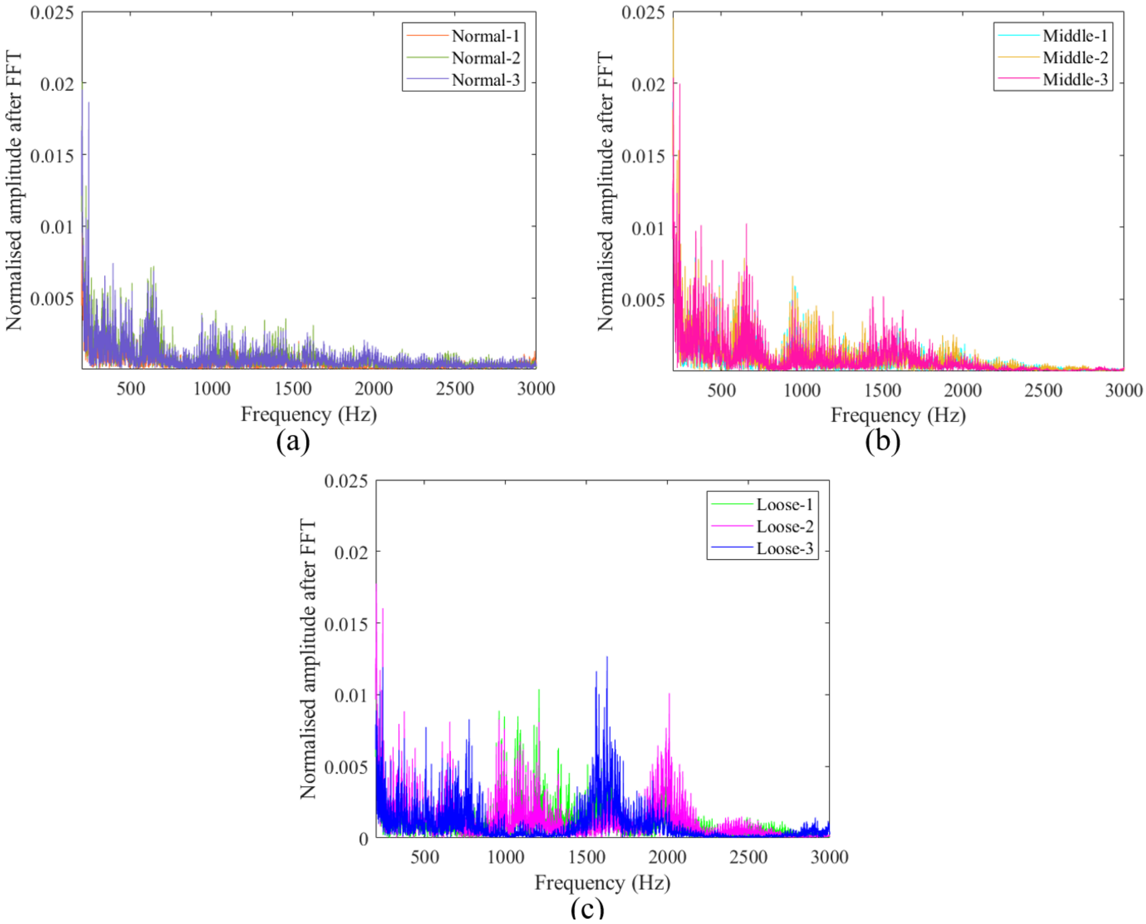

(a)

(b)

(c)

Figure 6.8 Signal repeatability (a) Normal (b) Middle (c) Loose

In this study, the frequency-domain signals collected from each slot wedge are compared. Although the waveforms for loose wedges vary, the differences between the signals from normal and loose wedges are evident, as shown in Figure 6.9(a). The differences are most pronounced in the frequency band between 900 Hz and 2100 Hz, while differences outside this range (below 900 Hz and above 2100 Hz) are less obvious. Therefore, the analysis band is further narrowed to 900–2100 Hz, as shown in Figure 6.9(b).

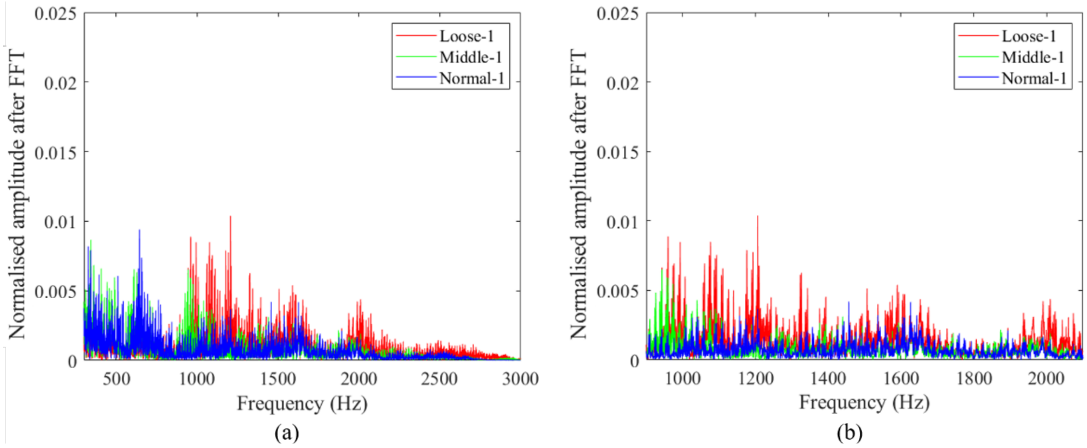

(a) (b)

Figure 6.9 Signal comparison (a) Frequency band 0~3000Hz (b) Frequency band 900~2100Hz

Although the waveforms for loose, middle, and normal wedges are distinct, quantitative frequency features are necessary for precise condition identification. To analyse the differences, the frequency peaks within the 900–2100 Hz band are examined. As shown in Figure 6.9, the primary differences in the signals occur around these peaks. The frequencies and amplitudes of these peaks are summarized in Tables 6.1 and 6.2, respectively.

Table 6.1 Frequency peak in the frequency band 900~2100 Hz

Number	Loose wedge	Middle wedge	Normal wedge
1	1207.3518	957.3521	1027.2049
2	2011.0276	944.1168	1024.2647
3	1627.2044	944.1168	1011.0285

Table 6.2 Normalised amplitude of frequency peak in the frequency band 900~2100 Hz

Number	Loose wedge	Middle wedge	Normal wedge
1	0.01032	0.004127	0.001951
2	0.006809	0.006516	0.003804
3	0.01268	0.005601	0.003944

As shown in Table 6.1, the peak frequencies vary. Generally, the resonance frequencies of normal wedges cluster around 1020 Hz, those of middle wedges around 950 Hz, and loose wedges exhibit a wider range from approximately 1000 Hz to 2000 Hz. This variation occurs because "looseness" is not a single defined condition; different degrees of loosening lead to different resonance frequencies. An initial classification attempt was made by defining thresholds based solely on resonance frequency: signals with peaks above 1200 Hz were classified as loose, those below 1000 Hz as middle, and those between 1000 Hz and 1200 Hz as normal. The classification result for all 63 signals, represented numerically (Loose=2, Middle=1, Normal=0), is summarized in Figure 6.10. As shown, this frequency-based approach resulted in numerous misclassifications, indicating that resonance frequency alone is not a reliable classifier.

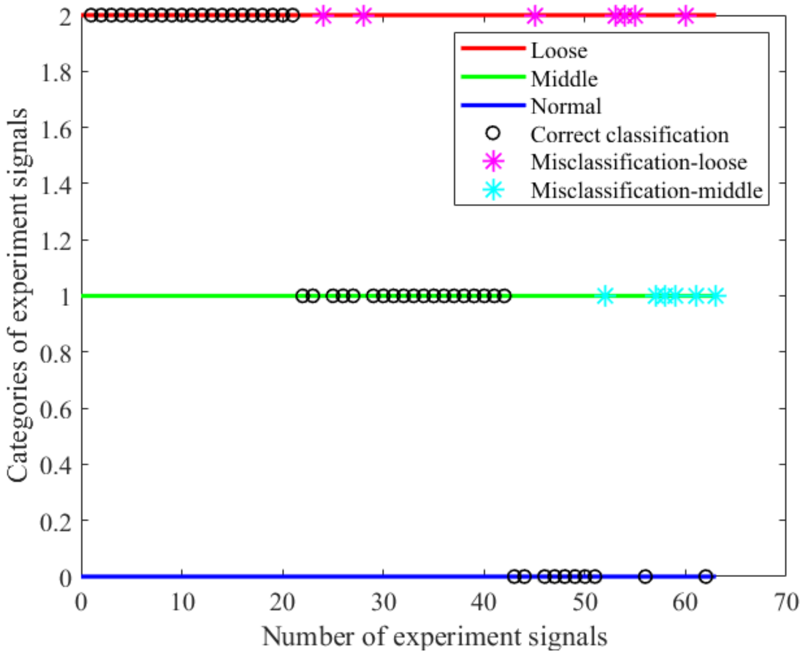

Figure 6.10 Classify the signals with frequencies

As summarised in Table 6.2, the loose wedges have a significantly higher maximum vibration amplitude compared with middle and normal wedges, while the differences between middle and normal are not very significant.

The threshold value can be defined as 0.0042 and 0.0068. If the average amplitude is lower than 0.0041, the wedge will be defined as normal. If the average amplitude is between 0.0068 and 0.0041, the wedge will be defined as middle. If the average amplitude is higher than 0.0068, the wedge will be defined as loose. Using these thresholds, all 63 signals are separated into three categories. Using the same method mentioned above, set the loose as 2, the middle as 1, and the normal as 0. The classification result is summarised in Figure 6.11.

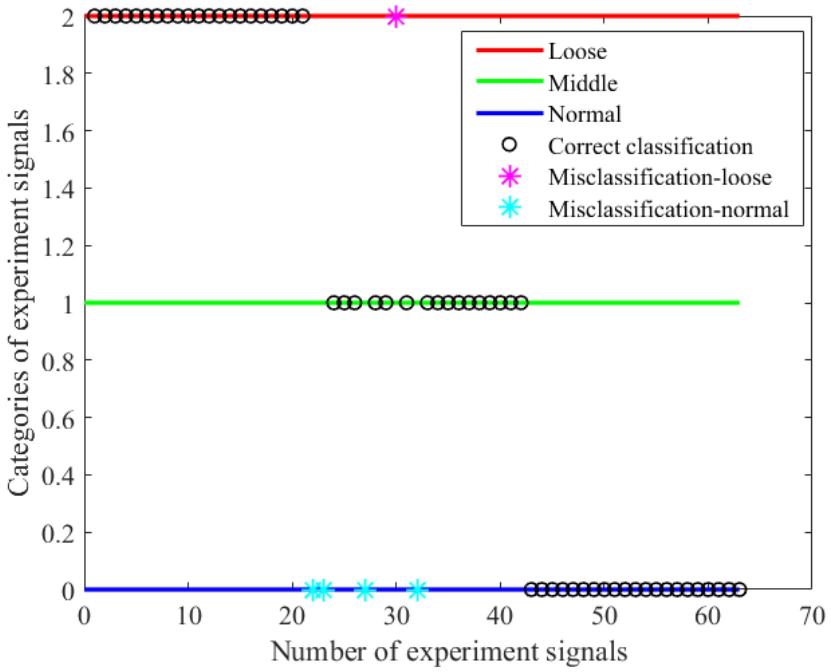

Figure 6.11 Classify the signals with the frequency amplitude threshold

Figure 6.11 shows that all loose and normal signals were correctly classified. However, some of the middle signals are misclassified into loose or normal signals. One of the middle signals is misclassified as the loose signal, and four of the middle signals are misclassified. The recognition accuracy is 92.06%. The accuracies of the normal and loose wedges are 100%, while the accuracy of the middle wedge is only 76.19%. Compared with traditional contact inspection, this method can identify the loose wedge clearly, while the accuracy of the middle wedge is not high. According to Xie's [85] research, the accuracy of all their methods is over 90%, which is relatively higher than that of this method.

According to their study, the recognition accuracy can reach 98.33%. The accuracy of Xie’s method is 6% higher than that of this method. However, as to the accuracy of the middle wedge, Xie’s model also has a relatively lower accuracy. For the middle wedge, the accuracy is 95%, which is 19% higher than that of this method. Both Xie’s method and this method can identify the loose and normal wedge, while for the middle wedge, both methods may misclassify the signal. It is because the conditions of the wedge are identified by a well-experienced worker that the operation errors may occur.

However, Xie's methods require direct contact. The knocking procedure may worsen the tightness. The operation of the contact method also requires the movement of the whole system. After inspecting a slot wedge, all the experiment equipment should be moved to the next slot wedge, which will require a relatively long time to deploy the whole system. As to the non-contact inspection method, after inspecting a slot wedge, the inspection system will not move, all the operation procedures are to change the position of the inspection point by tuning the angle of the LDV equipment, which will lead to a relatively short operating time. The advantages and disadvantages of the contact method and this method are summarised in Table 6.3.

Table 6.3 Advantages and disadvantages of contact and non-contact method

Requirement	Contact method	Non-contact method
Direct contact	Yes	No
Worsening the tightness	Possible	No
Move the inspection equipment frequently	Yes	No
Experienced operator	Yes	No

Accuracy	High	Acceptable
Time	Relatively long	Relatively short

Deep Learning (DL) is commonly used to enhance classification accuracy. As mentioned in Chapter 5, to fully utilise the features in the signal, this study also employs Continuous Wavelet Transform (CWT) to generate time-frequency representations (scalograms). The frequency band is 900~2100Hz. The CWT image of a loose slot is shown in Figure 6.12.

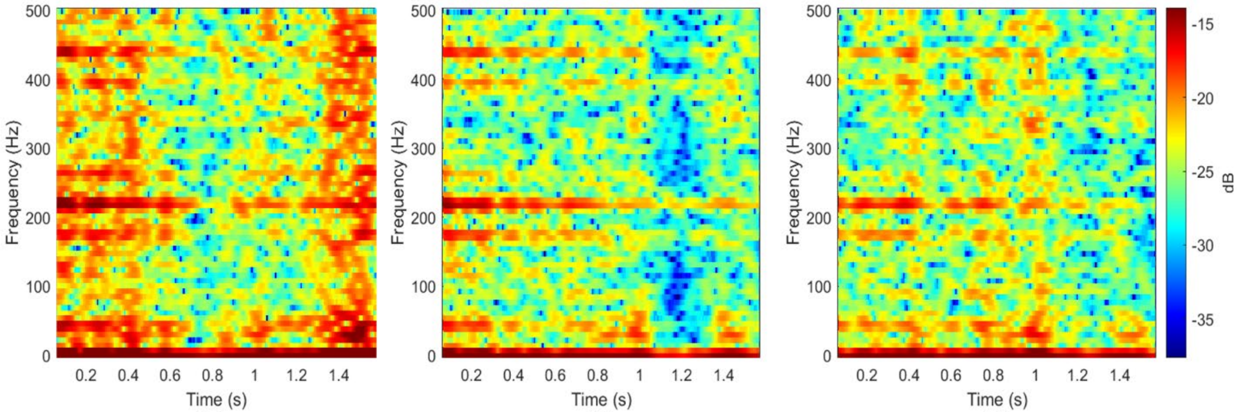

(a) (b) (c)

Figure 6.12 Time-frequency scalogram at (a) loose wedge (b) middle wedge (c) normal wedge

The structure of the DL network is exactly the same as that in Chapter 5. This DL network contains an input layer, five convolution layers, one dropout layer, three fully connected (FC) layers, one softmax layer, one classification layer, and an output layer. The inputs to the DL network are the CWT time-frequency scalograms, and the outputs are the three condition labels: loose, middle, and normal.

In this study, there are 14 points to be inspected, and 7 inspections are conducted at each point. Therefore, there are only 98 signals in total. The training group contains 80 time-frequency scalograms, the validation group contains 9 time-frequency scalograms, while the test group contains 9 time-frequency scalograms. For a DL network, this database is relatively small. However, the differences between the scalograms for different conditions (e.g., Figure 6.12) are quite distinct. Consequently, the classification results were excellent. The result of the classification network is shown in Figure 6.13(a). The accuracy of this network is about 100%. The confusion matrix in Figure 6.13(b) confirms that no samples in the test set were misclassified.

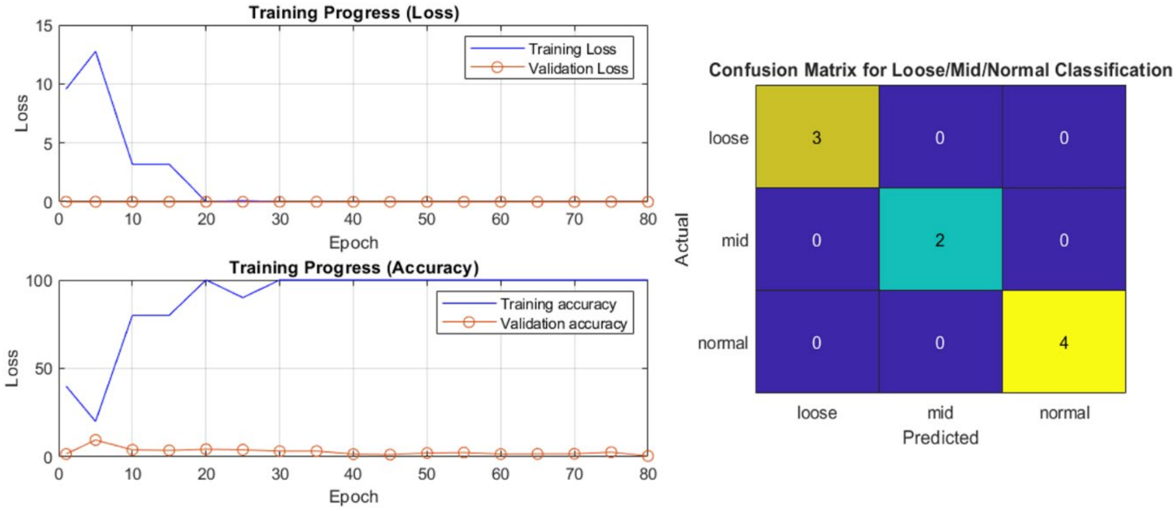

(a) (b)

Figure 6.13 (a) The accuracy and the loss of the network (b) confusion chart

This study demonstrates a powerful non-contact technique for detecting slot wedge looseness in hydro-generator stators. In the future, collecting more signals will allow the establishment of a larger database, enabling the use of DL for highly efficient and robust signal processing.

6.4 Summary

This chapter presented a non-contact acoustic inspection method for detecting looseness in stator slot wedges. A directional sound speaker was used as a remote acoustic source to excite the slot wedge, and the resulting vibration signal was collected remotely using a Laser Doppler Vibrometer (LDV). The acquired signal was processed using the Multi-Window Spectral Estimation (MWSE) algorithm and filtering to reduce background noise. The valid part of the signal was isolated using the short-time energy entropy ratio. By analysing this valid signal segment, the condition of the slot wedge could be identified as loose, middle, or normal. Using an amplitude-threshold approach, the identification accuracy for normal and loose wedges reached 100%, though the accuracy for middle wedges was lower (76.19%). By employing a deep learning network with CWT time-frequency scalograms as input, the classification accuracy for all three conditions achieved 100% on the available dataset.

This method has the potential for further development to inspect a large number of slot wedges simultaneously. The directional speaker could excite multiple wedges, and the responses could be collected using multiple LDV units. Furthermore, the current method can be enhanced with deep learning to increase its accuracy and robustness. The vibration signals gathered in this study form the foundation for a database that correlates signal features with specific loosening conditions. Training DL models on an expanded version of this database will facilitate efficient and accurate classification of slot wedge conditions, ultimately improving the maintenance strategies for hydro-generators

Chapter 7: Detection of tile debonding using mechanical excitation

As reviewed in Chapter 2, current studies have shown that most of the contact inspections are conducted using impact hammers. Although corresponding sensors have been developed to record the vibration signals and reduce the influence of operator subjectivity, these methods still require experienced workers to interpret the generated vibration signals. Furthermore, a thorough understanding of the signal processing involved in this NDI method is still lacking. Additionally, the accelerometers mounted on the specimen can influence its resonance frequency. Therefore, comprehensive experimental investigations are conducted in this chapter to explore a contact acoustic method for building tile inspection, to quantify the debonding location within the tile-adhesive-substrate system, and to study the effects of Digital Damage Fingerprints (DDF) and Artificial Neural Networks (ANN) in signal processing.

Debonding areas of tiles were detected using contact acoustic inspection. This involved first knocking the tile with an impact hammer to generate a vibration signal, then using a microphone to collect the vibro-acoustic signals during the knocking procedure. The collected vibration signals were processed using algorithms based on the Continuous Wavelet Transform (CWT) and Digital Damage Fingerprints (DDF), which mimic the working procedure of the human ear. Finally, the features from debonding and normal areas were gathered and compared by an ANN, enabling the localization of debonding areas. The relationships between normal and debonding areas were further discussed by examining the features within different signals.

7.1 Principle of inspection based on mechanical excitation

As mentioned in Chapter 2.2, knocking inspection using a hammer is one of the oldest and most widely used methods based on mechanical excitation. Different fixing conditions result in different knocking sound signals. Experienced operators can identify debonding conditions by recognizing different sounds, which essentially involves identifying different vibration frequencies within the human hearing range of 20 Hz to 20 kHz. This method has been used, for example, to inspect tiles on the Sydney Opera House, as shown in Figure 7.1. The operator climbed the roof of the Sydney Opera House and knocked on the tiles to inspect their condition. Ranzi et al. [212] developed a composite method to inspect the tiles on the Sydney Opera House. Their method uses a dynamic force sensor on the impact hammer to measure the applied force, an infrared thermometer to record the surface temperature of the tile, and a microphone to capture the sound generated during the tap test. The signals are classified by experienced operators and imported into a database, with evaluation criteria calibrated against engineering judgment. However, this method relies heavily on experienced operators and engineers, does not fully utilize the gathered signals, and lacks efficient data processing. In this study, data processing techniques such as CWT and DDF are used to modify the raw signals, and an ANN is employed for signal classification.

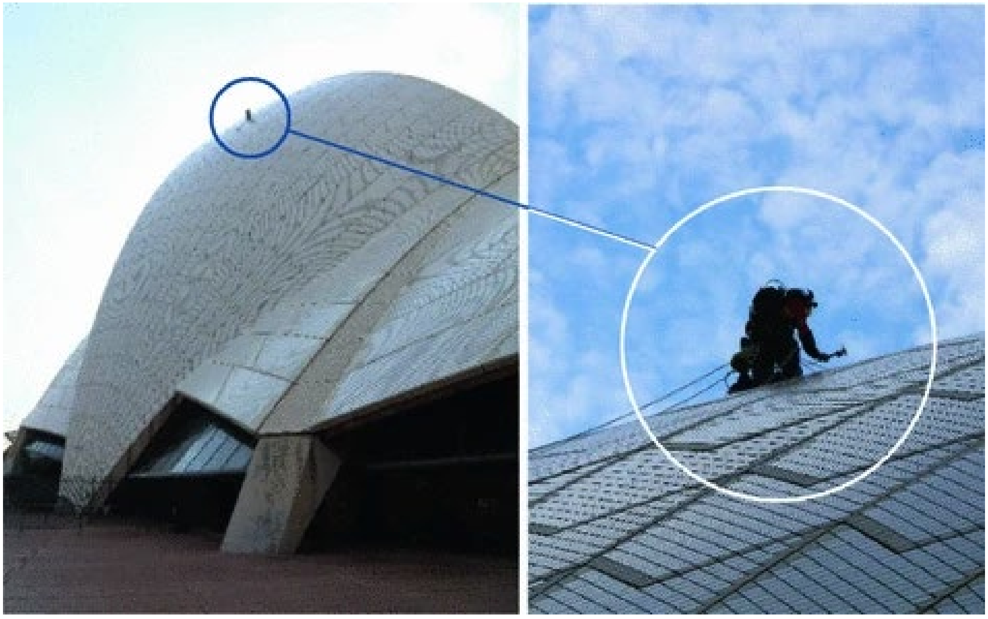

Figure 7.1 Operator performing the tap testing of tiles on the Sydney Opera House [212]

This study employs an impact hammer as an actuator and a microphone to record the sound signal, following a contact inspection approach. A schematic of the contact acoustic inspection method used in this chapter is presented in Figure 7.2. The tile is attached directly to cement to simulate the tile lid on the Sydney Opera House. The tile size is 97 × 97 mm. Parts of the cement are removed to simulate debonding areas. The microphone is positioned 80 mm from the tile. The initial height of the impact hammer is fixed at 10 mm to control the knocking energy. When the impact hammer strikes an inspection point, the tile is excited, generating a sound wave that is detected and recorded by the microphone.

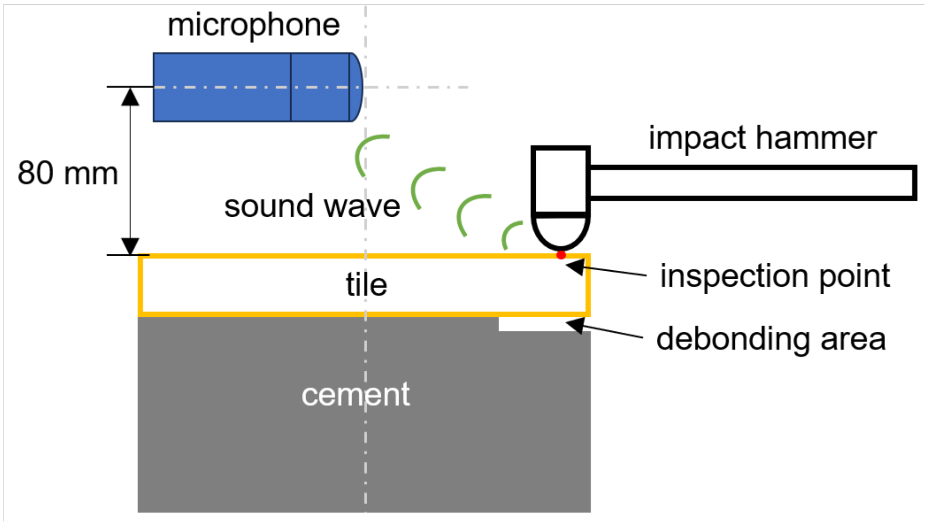

Figure 7.2 Sketch-up of the contact acoustic inspection method

After the experiment, the noise reduction procedure is conducted on the signals collected, and then the signals are transferred to the time-frequency domain to show the details of the time and frequency distribution. After that, the features in the time-frequency domain are gathered by DDF, and then an ANN is designed and trained to classify the debonding shapes.

7.2 Experiment setting

The experiment setup is shown in Figure 7.3. The specimens simulate the tile lids on the roof of the Sydney Opera House. The tile lid is fixed on an experiment table, and an impact hammer is used to knock the tile. A microphone collects the knocking sound. The position and height of the impact hammer are fixed to control the knock energy and sound path. A laptop is used to record and process the data.

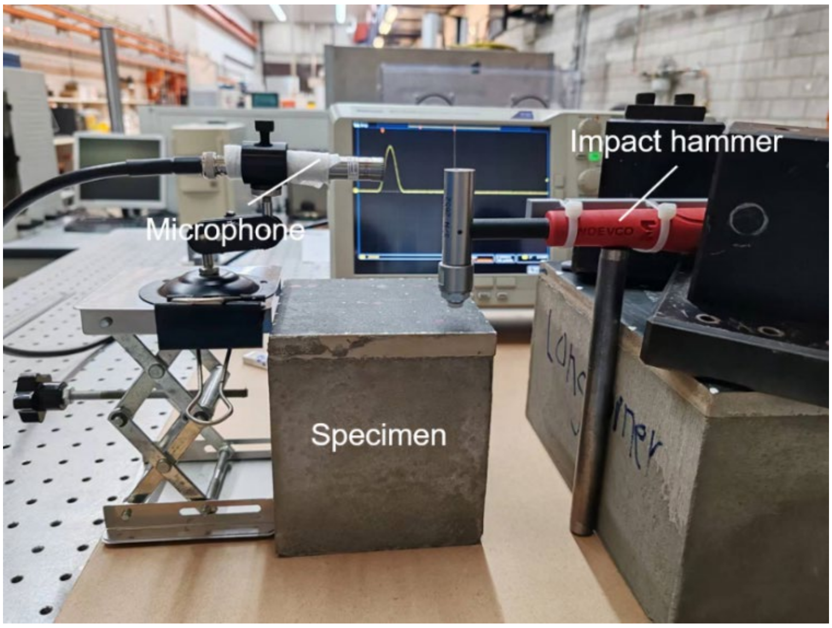

Figure 7.3 Experiment setup

As mentioned in Chapter 3.4, the tiles used in the Sydney Opera House were made by Höganäs with a thickness of 14 mm. These tiles are significantly thicker than commonly used tiles (3 mm thicker). The thickness of the precast concrete lid is 120 mm, and the size of the tile lid specimen in Figure 7.3 is 120 × 120 × 134 mm. The specimens of this part are exactly the same as in Chapter 3.4.

The impact hammer is fitted with a stacked multilayer high-quality piezoelectric force transducer that can generate a stable impact [213]. It is a popular excitation source in contact inspection for its low cost, ease of use, and simple structure [214, 215]. This method introduces no unwanted mass loading to the structure under test, making it an ideal excitation source.

The impact hammer used in this study is ENDEVCO MODEL 2302-10. This impact hammer has replaceable tips to suit different specimen materials. This study uses plastic and aluminium tips to inspect the specimen tile, as shown in Figure 7.4.

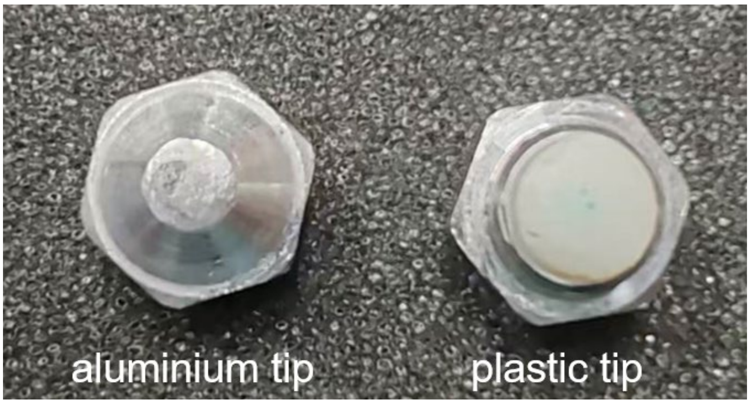

Figure 7.4 Aluminium and plastic tips of the impact hammer

The microphone is a typical sound recording system. It can convert acoustic energy into electrical energy [216]. When a sound wave propagates through a medium, the pressure and the density will deviate from the static value, resulting in sound pressure [217]. The sound pressure will generate a micro displacement on the diaphragm inside the microphone, and then, the displacement is converted into an electrical signal with a voltage (V) unit. The microphone used in this study is a PCB 378B02 prepolarised free-field condenser microphone. The compatible signal input module is the NI NI-9250C series sound and vibration input module.

In the experiment part, five inspection points are determined on the top surface of the specimens. The locations of the inspection points are shown in Figure 7.5.

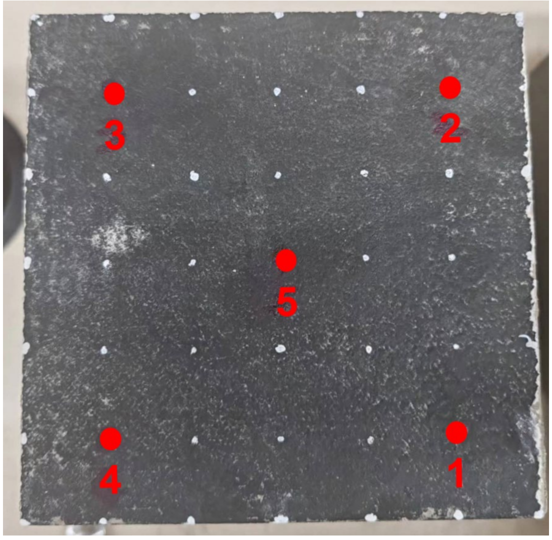

Figure 7.5 Location of inspection point

The positions of the impact hammer and microphone are fixed, as shown in Figure 7.6. Traditional contact inspection relies on experienced workers, and the knocking energy may vary. As mentioned in Chapter 2.2.1, the traditional method used an impact hammer with accelerometers to analyse the specimen. In this study, the knocking sound is used to analyse the specimen. Therefore, the knocking energy and the sound wave path are controlled. The distance between the tips of the impact hammer and the top surface of the specimen is 10 mm, while the distance between the microphone and the top surface of the specimen is 80 mm. The horizontal distance between the microphone and the inspection point is 65mm. The plastic tip and the aluminium tip are used to generate the knock signal of the specimen, respectively.

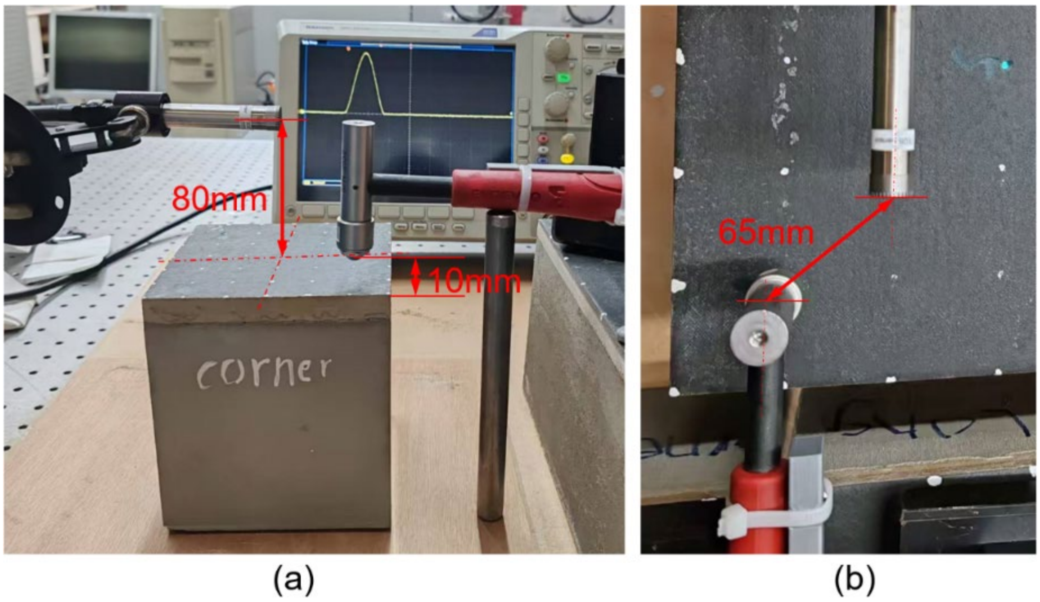

Figure 7.6 (a) Vertical distance between impact hammer, microphone and specimen (b) horizontal distance between impact hammer and microphone

7.3 Data processing

The signal collected by the microphone is a time-domain sound wave, where the x-axis represents time and the y-axis represents voltage. However, other equipment in the laboratory also generates sound waves, meaning the signal contains both valid information and background noise. Therefore, noise reduction is essential. Additionally, the time-domain signal alone does not reveal the frequency distribution. Transforming the signal into a time-frequency scalogram displays the energy distribution in both time and frequency domains. This study uses both the time domain and the time-frequency scalogram to analyse signal features.

7.3.1 Noise reduction

Noise reduction is a crucial step in signal processing. A commonly used noise reduction method compares several processes' spectral densities. Researchers use spectral densities to explore if there are any similar stochastic mechanisms in some observed time series [218-220]. The traditional periodogram method to calculate power spectral density attempts to model a stationary time series in the raw signal, then compares, classifies and clusters two or several time series [221-224]. However, the stationarity assumption is not satisfied in many situations, especially for periodically rhythmic processes [218]. Similar to Chapter 6, the Multi-Window Spectral Estimation (MWSE) is used to reduce the noise in this study. After the noise reduction procedure, the raw signal and the signal after noise reduction at inspection point 5 are summarised in Figure 7.7(a) and (b), respectively.

Furthermore, the valid fragments of knocking signals should also be captured. The microphone collects a relatively long signal to contain the knocking signal. As a result, the signal comprises invalid parts. This study uses the amplitude voice endpoint detection and short-term energy methods to determine the knocking signal.

Knocking signals are generally continuous non-stationary signals with significantly higher amplitude than other parts of the signal. In signal processing, a signal with an over 10-30 ms stationary stage can be defined as stationary [225].

Therefore, this study uses a Hamming window with a 20 ms width to frame and window the signal. The amplitude method compares the amplitude in each frame. If the absolute value of the amplitude varies by more than 0.025 in a frame, the frame is determined as the origin of the knocking signal, and then the duration of the knocking signal is determined. The duration of the knocking signal is defined as 0.07s, and then the valid knocking signal is plotted with a red dashed line in Figure 7.7(b).

The voice energy will also increase with this feature. The short-term energy method is a common means of effectively distinguishing voice signals. Hamming window effectively reduces the percussion leakage of the sound signal spectrum [226, 227]. For the percussion signal, the sample data can be defined as x(n), the signal after the Hamming window can be defined as $x_i(m)$, and the signal length can be defined as N. Then, the corresponding amplitude of short-term energy can be defined as:

$$AMP_i = \sum_{m=1}^{N} x_i^2(m) \tag{7.1}$$

Then, the short-term energy can be defined as EL_i:

$$EL_i = \log_{10}\left(1 + \frac{AMP_i}{a}\right) \tag{7.2}$$

Where a is a constant. When the peak AMP_i changes abruptly, a larger constant a can alleviate the EL_i, and then the noise in the speech can be distinguished. The normalised energy is summarised in Figure 7.7(c). The percussion signal has significantly higher energy, so the duration of the knocking part is defined with a red line in Figure 7.7(c). Then the knocking signal is identified with the two methods mentioned above, as shown in Figure 7.7(d).

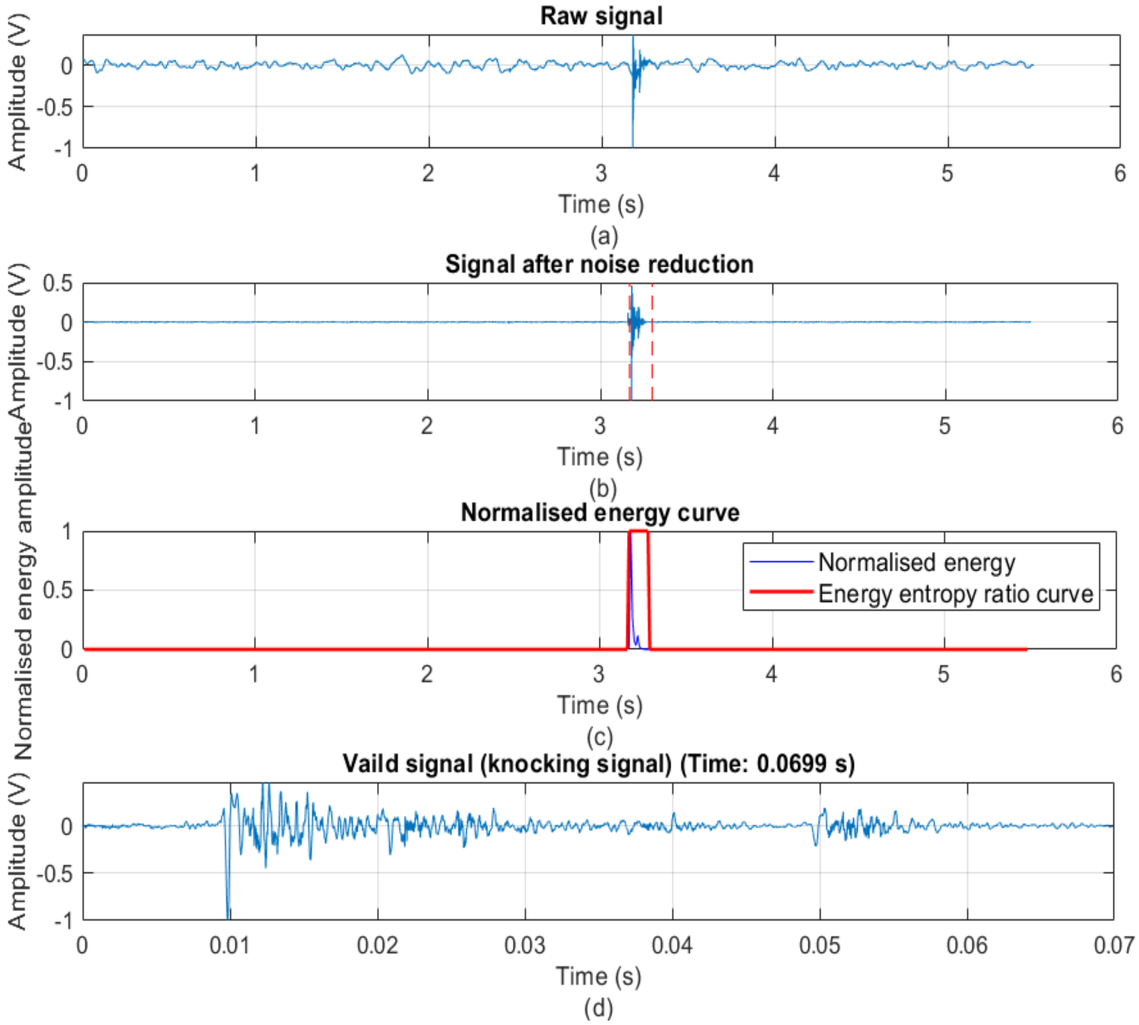

Figure 7.7 (a)Raw sound signal (b) Noise reduction: MWSE (c) valid signal gathered in energy curve by energy entropy ratio (d) valid signal

7.3.2 Signal processing: CWT

The real signal comprises a set of different elementary waveforms. Wavelet transform is a method that can decompose the real signal and then analyse the elementary waveforms by examining the wavelet coefficients [228, 229]. This study uses the CWT to gather the time and frequency features in the signal after the noise reduction procedure.

As mentioned in Chapter 5.2, the CWT of a signal x(t)is defined as:

$$X(a,b) = \frac{1}{|a|^{\frac{1}{2}}} \int_{-\infty}^{\infty} x(t)\bar{\psi}\left(\frac{t-b}{a}\right) dt \tag{7.3}$$

where a is a positive real number, and b is a real number. a is the scale factor that dilates or compresses the signal, and b is the translational factor that translates the signal. Equation (7.3) defines a continuous function ψ(t) (continuous in both the time and frequency domains) as the mother wavelet. ψ(t) can generate the daughter wavelets, translated and scaled versions of the mother wavelet.

Using MATLAB, the CWT scalogram of the knocking signal at inspection point 3 is plotted in Figure 7.8. The x-axis shows the time, the y-axis shows the frequency, and the different colours correspond to different velocity magnitudes.

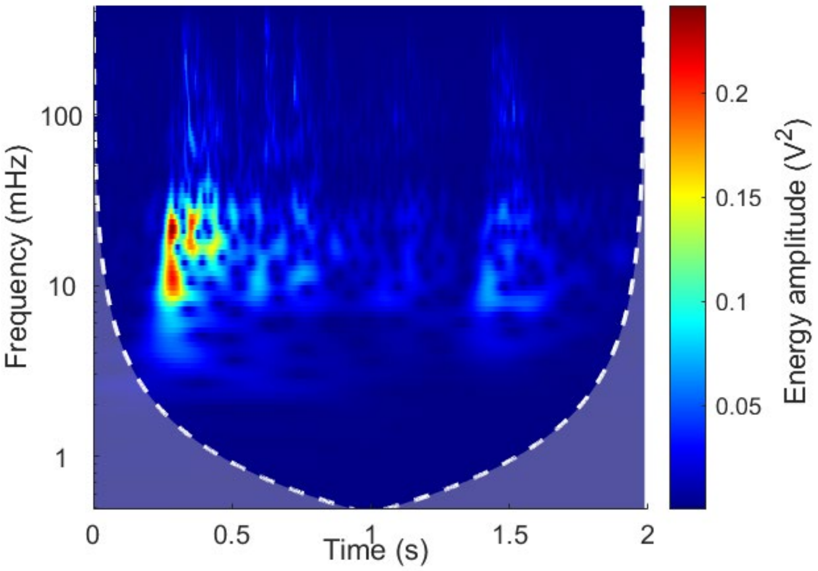

Figure 7.8 Time-frequency scalogram at the inspection point 3

Then, the time-domain and the time-frequency scalogram of the valid knocking signal are used to gather the DDF features.

7.3.3 DDF identification

Though the noise in the raw knocking signal has been removed, the challenge of debonding identification is to define and extract features appropriately from valid signals. Therefore, a faithful description of the valid signal is essential. Su and Ye [230] established an effective concept named DDF to quantitatively describe the features in the valid knocking signal.

A characteristic point is defined as a local extremum—a point in the filtered time-domain signal or the time-frequency scalogram whose absolute amplitude (or energy magnitude) is simultaneously greater or less than its immediate neighbours [230-232]. The corresponding amplitude or energy is the characteristic amplitude. The characteristic points and their amplitude are defined as principal components for the signal. The principal components from the signal collected at inspection point 3 are gathered by MATLAB, as shown in Figure 7.9.

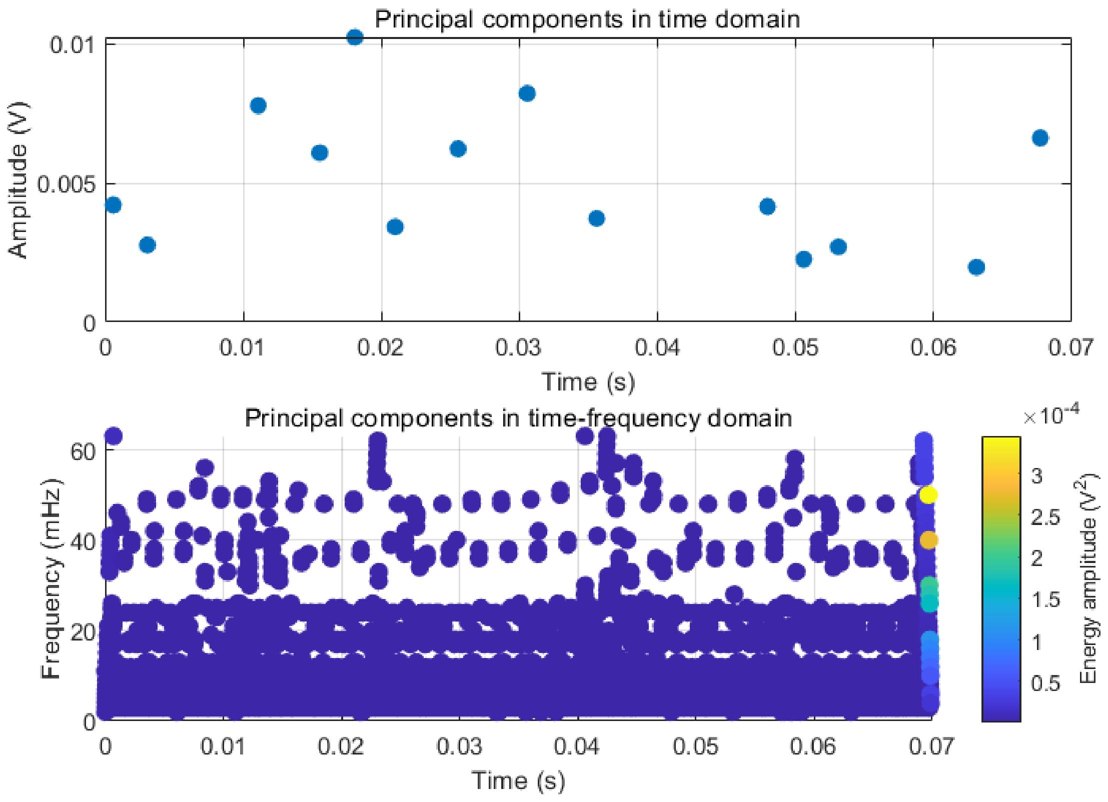

Figure 7.9 Principal components at the inspection point 3

As shown in Figure 7.9, the characteristic points with the concerned period as well as the characteristic amplitudes in the time-domain signal, and the characteristic points for each energy concentration in the energy spectrum are extracted. In the time domain, the number of characteristic points varies from 14 to 30, while the number of those in the time-frequency domain varies from 3200 to 5000.

Subsequently, feature vectors are constructed to represent these principal components: [time, amplitude] pairs for the time domain and [time, frequency, amplitude] triplets for the time-frequency domain. These feature vector pairs are the inputs of the ANN.

7.3.4 Identify the debonding area

As mentioned in Chapter 3.3.3, the principal components of the time domain and time-frequency domain signals are summarised in two feature vector pairs. Since the 1980s, the artificial neural network (ANN) has been increasingly utilised in signal processing, classification, pattern recognition, and system identification [233-235]. This technique developed a parallel computational model to simulate the human brain mechanism, which endowed the ANN with advantages in parallelism, robustness and adaptability [229]. In this study, the principal components gathered by DDF are used to train the ANN.

The fundamental operation of a neuron in an ANN is described by Equation (7.4). Each neuron in a layer is connected to all neurons in the previous layer [189]. A linear transformation is applied to the input through a weight matrix, which can be written as:

$$v^l = \sum_{j=1}^{m} \omega_{ij}^{l-1} T_i^{l-1} + b^{l-1} \tag{7.4}$$

Where v^l is the output vector in the layer l, m is the number of neurons in the layer l-1, ω_{ij}^{l-1} is the connection weight between layer l-1 and layer l, T_i^{l-1} is the ith activated neuron value in the layer l-1, and b is the bias value in the layer l-1. The sketch of the ANN used in this study is summarised in Figure 7.10. A feedforward neural network with several hidden neural processing layers was developed.

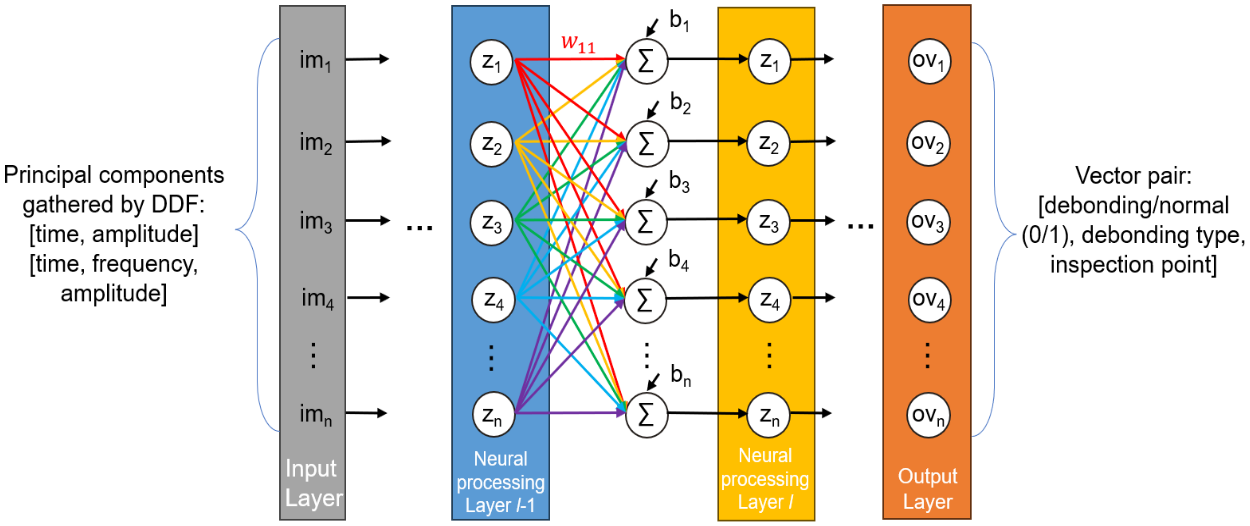

Figure 7.10 Architecture of the artificial neural network (ANN) used in this study

In this study, the ANN contains three hidden layers. The first hidden layer contains 128 neurons, the second contains 96 neurons, and the third contains 32 neurons.

As mentioned above, the time-frequency domain signal obviously contains more characteristic points than the time domain signal. To avoid padding the DDF signals with zeros, 10 sets of time data and corresponding crest amplitudes in the time-domain signal, and 10 sets of time and frequency data, as well as corresponding energy crest amplitudes in the time-frequency domain, are selected from the signal. As shown in Figure 7.10, the inputs of this ANN at each inspection point are 10 [time, amplitude] feature vector pairs and 10 [time, Frequency, amplitude] feature vector pairs. Each inspection point contains 12 knocking signals gathered by a microphone in the experiment. By considering these five inspections, a total of 600 feature vector pairs were extracted from the specimen. 480 feature vector pairs are selected as the training group, 60 feature vector pairs are selected as the validation group, and 60 feature vector pairs are selected as the test group. The output of the trained ANN is selected as a vector pair [debonding/normal (0/1), debonding type, inspection point]. For example, the output vector of a DDF signal collected at inspection point 3 in the corner debonding specimen is [0, corner debonding, 3].

The prediction results for one selected inspection point on a debonding specimen (corner debonding inspection point 4) are summarised in Table 7.1.

Table 7.1 Prediction result for a single trial at inspection point 4 (corner debonding specimen)

Item	True	Predict
Debonding/normal	1	1
Debonding type	Corner debonding	Normal
Position	4	3

As shown in Table 7.1, the model correctly predicted the presence of debonding (Debonding/Normal), but misclassified the debonding type and the inspection point location. The overall prediction accuracies across all trials, using impact hammers with plastic and aluminium tips (based on 10 feature sets per domain), are summarized in Table 7.2.

Table 7.2 Overall prediction accuracy using 10 feature sets per domain

Item	Plastic tip	Aluminium tip
Debonding/normal	72.22%	77.78%
Debonding type	19.44%	33.33%
Position	11.11%	25.00%

As summarised in Table 7.2, the impact hammer with an aluminium tip has a higher prediction accuracy, but the prediction accuracy is too low to be considered as an effective prediction method. The prediction accuracies of the debonding type and the position are relatively lower than the debonding/normal prediction.

This low accuracy of the prediction accuracy is caused by several reasons. Firstly, the inputs of the ANN are 10 feature sets, which contains relatively limit features. The inputs vectors only contain 10 maximum feacture vectors of the raw signal. As a result, a lagrer feature vector which contains 30 sets of time data and corresponding crest amplitudes in the time-domain signal, and 30 sets of time and frequency data, as well as corresponding energy crest amplitudes in the time-frequency domain, are selected from the signal. The accuracies are summarised in Table 7.3.

Table 7.3 Prediction accuracy comparison using 10 versus 30 feature sets per domain

Item	Plastic tip (10 sets)	Plastic tip (30 sets)	Aluminium tip (10 sets)	Aluminium tip (30 sets)
Debonding/normal	72.22%	75.00%	77.78%	83.33%
Debonding type	19.44%	22.22%	33.33%	36.11%
Position	11.11%	66.67%	25.00%	27.78%

The prediction accuracy generally improved with the increase in the number of feature sets used for training, as evidenced in Table 7.3. Notably, the accuracy for locating the inspection point increased substantially for the plastic-tipped hammer when 30 feature sets were used. These results suggest that building a larger and more comprehensive feature database could enhance the performance of the ANN model. The accuracy for detecting the presence of debonding remains the most robust outcome. However, the prediction accuracy is still relatively low. This is because only 4 inspection points are used to inspect the tile. If the debonding appears at point 4, the point 1~3 remain normal. In the meantime, in corner debonding and half debonding, the normal point also has similar data. A similar situation may confuse the ANN in identifying the position. The present study has demonstrated that prediction accuracy increases as more data become available, and the underlying concept of the method has been validated accordingly. To achieve satisfactory prediction performance, it is possible that a very large volume of data, potentially on the order of trillions of samples, may be required. As the database continues to expand, a more refined analytical solution can be expected. By deploying a denser array of inspection points, a debonding map could potentially be generated with higher confidence based primarily on the debonding/normal predictions at each point.

7.4 Summary

This chapter presents a contact inspection method that utilizes mechanical excitation through an impact hammer and acoustic recording via a microphone. The sound signal generated by striking the tile was recorded and processed. Key steps in the process included noise reduction using MWSE, valid signal segmentation, time-frequency analysis through the Continuous Wavelet Transform (CWT), and feature extraction using Digital Damage Fingerprints (DDF). The extracted DDF features were then fed into an Artificial Neural Network (ANN) to classify the tile's condition (debonding or normal), identify the type of debonding, and locate the inspection point.

Experimental results showed that the choice of impact hammer tip material influenced prediction accuracy, with the aluminum tip generally outperforming the plastic tip. The fundamental task of distinguishing between debonding and normal areas achieved significantly higher accuracy compared to the more detailed tasks of classifying the type of debonding and pinpointing the location. Increasing the number of feature sets used for training generally led to improved model performance, highlighting the potential benefits of using larger datasets. Future work should focus on expanding the database to include more inspection points and characteristic features, further enhancing the ANN's robustness and accuracy. The proposed methodology shows promise for integration into automated systems for large-scale inspection applications.

Chapter 8: Conclusions and outlook

8.1 Conclusion remarks

This study conducted non-destructive inspection (NDI) on tile (both normal and thick) and slot wedge specimens (from a hydro-generator stator) using both contact and non-contact methods, along with corresponding data processing techniques. The efficacy of these inspection methods was detailed through simulations and experiments. Various noise reduction techniques were applied to the signals to suppress background noise. Machine learning methods, including Artificial Neural Networks (ANN) and Deep Learning (DL), were employed to summarise and predict damage, thereby enhancing the efficiency and accuracy of the NDI results. The key findings are summarised as follows:

In the experimental study of non-contact inspection, an acoustic method based on Laser Doppler Vibrometer (LDV) was evaluated. A directional speaker was used to excite the tile specimen, while an LDV captured the resulting vibration signals. A multitone burst (MTNB) signal generated by the speaker swept a pre-designed frequency band to induce resonance with high vibration amplitude in the tile. Building on experience from contact acoustic inspection, a higher density of inspection points (36 points) was deployed to improve inspection effectiveness. A contour map of the debonding area was plotted based on the resonance amplitudes at these points, accurately delineating the debonding profile. Inspection results on debonding areas of different shapes demonstrated the method's quantitative capability for tile debonding detection. Furthermore, studies on thicker tiles confirmed that increased tile thickness does not significantly affect inspection accuracy, indicating the potential for applying this method to other types of specimens.

In the numerical study of the non-contact acoustic inspection method, an effective model was established to analyse the interaction between sound waves and tile vibration. The numerical model comprised a pre-defined sound wave, a tile, an adhesive layer, and the sound propagation medium (air). Material properties for the tile and adhesive were determined through experimental characterisation. Boundary conditions in the model were set to replicate the actual experimental setup. The debonding area was plotted using the same method as in the experimental study above. Compared to experimental results, the numerical model provided superior resolution, detailing the debonding profile and demonstrating its potential for analysing debonding morphology in tile specimens.

In research aimed at improving inspection efficiency using deep learning networks, the experimental setup mirrored the non-contact acoustic method described earlier. After data acquisition, three deep learning networks were developed and trained to enhance inspection accuracy. Time-domain signals collected by the LDV were converted into Continuous Wavelet Transform (CWT) images to capture time-frequency details. These CWT images were then used to train the networks. The approach follows a two-stage process: the first network determines whether the input

CWT image matches a known debonding shape in the database. If a match is found, the classification is complete with 100% accuracy. If not, inspection points are deployed across the specimen, and a second deep learning network identifies the condition at each point to plot the debonding shape on a contour map. The prediction accuracy for unknown debonding shapes ranged from 69% to 99%. The classification results of this two-stage method aligned well with the actual conditions, confirming its effectiveness. The database can be expanded by incorporating CWT images of new debonding shapes, which would further reduce prediction errors.

By extending this non-contact acoustic inspection method, the loosening of slot wedges on a hydro-generator stator can also be detected. The experimental setup was identical to the tile inspection method. The signal, gathered by the LDV and excited by a pre-defined frequency band generated by a directional sound speaker, was processed using Multi-Window Spectral Estimation (MWSE) for noise reduction. An entropy ratio was then applied to isolate the valid signal component. The signals were classified into three conditions: loose, medium, and normal. The classification accuracy for normal and loose conditions was 100%. With the assistance of a deep learning (DL) network, all three conditions were classified with 100% accuracy.

In the contact inspection study, an acoustic method based on Digital Damage Fingerprints (DDF) and ANN was developed to identify debonding areas. An impact hammer and a microphone were used to analyse tile debonding on the Sydney Opera House systematically. This method demonstrated significant potential for debonding detection. The impact hammer provided consistent knocking energy, while the microphone captured sound signals with a high signal-to-noise ratio at each inspection point. The MWSE algorithm was applied for noise reduction, and the DDF algorithm was used to extract features from the valid segments of the time and time-frequency domain signals collected at five inspection points. These features were used to train a machine learning model, and a trained Artificial Neural Network (ANN) was subsequently employed to predict the debonding type and position. The inspection demonstrated considerable accuracy. Further investigation revealed that both the hammer tip material and the database size had an impact on the prediction results. An aluminum tip achieved higher prediction accuracy than a plastic tip, and increasing the number of characteristic points also improved accuracy.

8.2 Future work

Based on the current work, acoustic inspection methods are highly effective for damage detection. While significant insights have been gained and both contact and non-contact methods have yielded satisfactory results, several areas still require further investigation to advance the field of structural health monitoring. The data processing algorithms for both methods are crucial to their overall performance.

For the non-contact acoustic method, additional noise reduction algorithms and deep learning architectures could be explored to further suppress noise and extract more discriminative features from vibration signals. The accuracy of the numerical model should be enhanced, and simulated vibration data could be incorporated into the training database to improve the performance of deep learning networks. Furthermore, given the lightweight nature of the non-contact system and the fact that tiles are often installed at high elevations, the inspection system could be mounted on an unmanned aerial vehicle (UAV) to automate inspections and eliminate the need for workers to perform high-altitude operations.

For slot wedge detection, more sophisticated classification algorithms should be applied to improve the accuracy of identifying the "medium" condition. Additionally, a larger database of vibration signals should be compiled by collecting more data via the impact hammer and the microphone.

For the contact acoustic method, a more extensive dataset of knocking signals should be acquired. The feature extraction algorithms and machine learning models could be refined to enhance inspection performance. Meanwhile, since the overall system is compact, it could be integrated onto a small robotic platform to enable automated detection of inspection points.

References

[1] C. Zhong, et al., Evaluating trends, profits, and risks of global cities in recent urban expansion for advancing sustainable development. Habitat International, 2023. 138: p. 102869. DOI: https://doi.org/10.1016/j.habitatint.2023.102869.

[2] W.-L. Hsu, et al., Discussion on the Material Factors for Falling of Face Tile. Sensors and Materials, 2019. 31(3): p. 1071-1081.

[3] B.L. Luk, L.K. Liu, and A.A. Collie, Climbing service robots for improving safety in building maintenance industry. Bioinspiration and Robotics: Walking and Climbing Robots, 2007, IntechOpen.

[4] N.S.W. Safework, Falling objects, https://www.safework.nsw.gov.au/hazards-a-z/falling-objects, 2015 (accessed 16 September 2022).

[5] O. Bergamo, et al., In-situ NDT testing procedure as an integral part of failure analysis of historical masonry arch bridges. Engineering Failure Analysis, 2015. 57: p. 31-55.

[6] N. Xie, et al., A numerical study on the influence of composite wrinkle defect geometry on compressive strength. Materials & Design, 2018. 140: p. 7-20.

[7] R.L. Beilharz, Tile Applications in Public Buildings. A Collection of Papers Presented at the 95th Annual Meeting and the 1993 Fall Meeting of the Materials & Equipment/Whitewares Manufacturing: Ceramic Engineering and Science Proceedings. 1994. p. 441-449. DOI: https://doi.org/10.1002/9780470314340.ch47.

[8] M. Romero and J.M. Pérez, Relation between the microstructure and technological properties of porcelain stoneware. A review. Materiales de Construcción, 2015. 65(320): p. e065. DOI: 10.3989/mc.2015.05915.

[9] C.Y. Yiu, D.C.W. Ho, and S.M. Lo, Weathering effects on external wall tiling systems. Construction and Building Materials, 2007. 21(3): p. 594-600. DOI: https://doi.org/10.1016/j.conbuildmat.2005.11.002.

[10] F. Tong, S.K. Tso, and X.M. Xu, Tile-wall bonding integrity inspection based on time-domain features of impact acoustics. Sensors and Actuators A: Physical, 2006. 132(2): p. 557-566. DOI: https://doi.org/10.1016/j.sna.2005.12.035.

[11] M.A. Arenas, et al., PVD hard coatings on ceramic tiles for aesthetic applications: surface characterisation and corrosion properties. Ceramics International, 2022. 48(15): p. 21794-21802. DOI: https://doi.org/10.1016/j.ceramint.2022.04.163.

[12] E. Sánchez, et al., Porcelain tile: Almost 30 years of steady scientific-technological evolution. Ceramics International, 2010. 36(3): p. 831-845. DOI: https://doi.org/10.1016/j.ceramint.2009.11.016.

[13] A.E.F.d.S. Almeida and E.P. Sichieri, Experimental study on polymer-modified mortars with silica fume applied to fix porcelain tile. Building and Environment, 2007. 42(7): p. 2645-2650. DOI: https://doi.org/10.1016/j.buildenv.2006.07.002.

[14] F. Tahmasebinia, et al., Numerical Analysis of the Creep and Shrinkage Experienced in the Sydney Opera House and the Rise of Digital Twin as Future Monitoring Technology. Buildings, 2019. 9(6): p. 137.

[15] M. Dondi, et al., Resource efficiency versus market trends in the ceramic tile industry: Effect on the supply chain in Italy and Spain. Resources, Conservation and Recycling, 2021. 168: p. 105271. DOI: https://doi.org/10.1016/j.resconrec.2020.105271.

[16] M. Dondi, M. Raimondo, and C. Zanelli, Clays and bodies for ceramic tiles: Reappraisal and technological classification. Applied Clay Science, 2014. 96: p.

91-109. DOI: https://doi.org/10.1016/j.clay.2014.01.013.

[17] F. Andreola, et al., Rheological behaviour and mechanical properties of porcelain stoneware bodies containing Italian clay added with bentonites. Ceramics International, 2009. 35(3): p. 1159-1164. DOI: https://doi.org/10.1016/j.ceramint.2008.05.017.

[18] A. Wetzel, et al., Influence of shrinkage and water transport mechanisms on microstructure and crack formation of tile adhesive mortars. Cement and Concrete Research, 2012. 42(1): p. 39-50. DOI: https://doi.org/10.1016/j.cemconres.2011.07.007.

[19] A. Wetzel, et al., Long-term study on failure mechanisms of exterior applied tilings. Construction and Building Materials, 2012. 37: p. 335-348. DOI: https://doi.org/10.1016/j.conbuildmat.2012.07.072.

[20] T. Mahaboonpachai, T. Matsumoto, and Y. Inaba, Investigation of interfacial fracture toughness between concrete and adhesive mortar in an external wall tile structure. International Journal of Adhesion and Adhesives, 2010. 30(1): p. 1-9. DOI: https://doi.org/10.1016/j.ijadhadh.2009.06.005.

[21] R. Li, et al., Wind Effects on Roofs with High-Profile Tiles: Experimental Study. Journal of Architectural Engineering, 2014. 20(4): p. B4014002. DOI: 10.1061/(ASCE)AE.1943-5568.0000156.

[22] D. Clark, A. McPherson, and R. Van Dissen, Long-term behaviour of Australian stable continental region (SCR) faults. Tectonophysics, 2012. 566-567: p. 1-30. DOI: https://doi.org/10.1016/j.tecto.2012.07.004.

[23] D. Giardini, et al., The GSHAP global seismic hazard map. Annals of Geophysics, 1999. 42(6).

[24] D. Henderson and J. Ginger, Role of Building Codes and Construction Standards

in Windstorm Disaster Mitigation. The Australian Journal of Emergency Management, 2008. 23(2): p. 40-46.

[25] S. Australia, AS 4055:2021: Wind loads for housing. 2021: Sydney, Australia.

[26] D.J. Smith, F.J. Masters, and A.G. Chowdhury, Investigating a wind tunnel method for determining wind-induced loads on roofing tiles. Journal of Wind Engineering and Industrial Aerodynamics, 2016. 155: p. 47-59. DOI: https://doi.org/10.1016/j.jweia.2016.05.006.

[27] S. Australia, AS/NZS 1170.2:2011 Structural design actions, Part 2: Wind actions. 2011: Sydney, Australia.

[28] A. Troccoli, et al., Long-Term Wind Speed Trends over Australia. Journal of Climate, 2012. 25(1): p. 170-183. DOI: https://doi.org/10.1175/2011JCLI4198.1.

[29] H. Guo, M. Xu, and Q. Hu, Changes in near-surface wind speed in China: 1969–2005. International Journal of Climatology, 2010. 31: p. 349-358.

[30] Y. Jiang, et al., Changes in wind speed over China during 1956–2004. Theoretical and Applied Climatology, 2010. 99: p. 421-430.

[31] Y. Zhang, et al., Numerical simulation on damage behaviors of tile-mortar interface induced by mortar shrinkage and temperature cycles. Engineering Failure Analysis, 2023. 148: p. 107169. DOI: https://doi.org/10.1016/j.engfailanal.2023.107169.

[32] C. Pereira, J. de Brito, and J.D. Silvestre, Contribution of humidity to the degradation of façade claddings in current buildings. Engineering Failure Analysis, 2018. 90: p. 103-115. DOI: https://doi.org/10.1016/j.engfailanal.2018.03.028.

[33] A. Wetzel, R. Zurbriggen, and M. Herwegh, Spatially resolved evolution of

adhesion properties of large porcelain tiles. Cement and Concrete Composites, 2010. 32(5): p. 327-338. DOI: https://doi.org/10.1016/j.cemconcomp.2010.02.002.

[34] C.-T. Liao, Study on Exterior Wall Tile Degradation Conditions of High-rise Buildings in Taoyuan City. Journal of Asian Architecture and Building Engineering, 2018. 17(3): p. 549-556. DOI: 10.3130/jaabe.17.549.

[35] C. Wong. Physical, mechanical, chemical and visual tests for tile failure investigation: case study. in IV WORLD CONGRESS ON CERAMIC TILE QUALITY. Castellón (España). Cámara Oficial de Comercio, Industria y Navegación. 1996.

[36] R. Montero, et al., Past, present and future of robotic tunnel inspection. Automation in Construction, 2015. 59: p. 99-112. DOI: https://doi.org/10.1016/j.autcon.2015.02.003.

[37] C. Amann, et al., A review on process-induced distortions of carbon fiber reinforced thermosets for large-scale production. Production Engineering, 2017. 11(6): p. 665-675. DOI: 10.1007/s11740-017-0772-1.

[38] S. Han, et al., Non-destructive testing and structural health monitoring technologies for carbon fiber reinforced polymers: a review. Nondestructive Testing and Evaluation, 2024. 39(4): p. 725-761. DOI: 10.1080/10589759.2024.2324149.

[39] M.R. Jolly, et al., Review of non-destructive testing (NDT) techniques and their applicability to thick walled composites. Procedia CIRP, 2015. 38: p. 129-136.

[40] D. McCann and M. Forde, Review of NDT methods in the assessment of concrete and masonry structures. NDT & E International, 2001. 34(2): p. 71-84.

[41] J. Martin, et al., Accuracy of NDE in bridge assessment. Engineering structures,

1998. 20(11): p. 979-984.

[42] I. Papa, V. Lopresto, and A. Langella, Ultrasonic inspection of composites materials: Application to detect impact damage. International Journal of Lightweight Materials and Manufacture, 2021. 4(1): p. 37-42. DOI: https://doi.org/10.1016/j.ijlmm.2020.04.002.

[43] G. Dobie, et al., A Noncontact Ultrasonic Platform for Structural Inspection. IEEE Sensors Journal, 2011. 11(10): p. 2458-2468. DOI: 10.1109/JSEN.2011.2138131.

[44] E. Eren and S. Kurama, Defect detection in porcelain tiles using ultrasound, in Nondestructive Testing of Materials and Structures. 2013, Springer. p. 381-386.

[45] E. La Malfa Ribolla, et al., Ultrasonic inspection for the detection of debonding in CFRP-reinforced concrete. Structure and Infrastructure Engineering, 2018. 14(6): p. 807-816.

[46] G. Mathers. Ultrasonic Examination Part 1. 2021 [cited 2021; Available from: https://www.twi-global.com/technical-knowledge/job-knowledge/ultrasonic-examination-part-1-127.

[47] R. Ali and Y.-J. Cha, Attention-based generative adversarial network with internal damage segmentation using thermography. Automation in Construction, 2022. 141: p. 104412. DOI: https://doi.org/10.1016/j.autcon.2022.104412.

[48] C. Laofor and V. Peansupap, Defect detection and quantification system to support subjective visual quality inspection via a digital image processing: A tiling work case study. Automation in Construction, 2012. 24: p. 160-174. DOI: https://doi.org/10.1016/j.autcon.2012.02.012.

[49] C.-C. Cheng, T.-M. Cheng, and C.-H. Chiang, Defect detection of concrete structures using both infrared thermography and elastic waves. Automation in

Construction, 2008. 18(1): p. 87-92.

[50] V. Pagliarulo, et al., Impact damage investigation on composite laminates: comparison among different NDT methods and numerical simulation. Measurement Science and Technology, 2015. 26(8): p. 085603.

[51] M. Moradi and M.S. Safizadeh, Numerical and Experimental Simulation of Thermography for Detection of Debonding in Repaired Aluminum by Carbon/Epoxy Patch. 2019.

[52] S. Gholizadeh, A review of non-destructive testing methods of composite materials. Procedia Structural Integrity, 2016. 1: p. 50-57. DOI: https://doi.org/10.1016/j.prostr.2016.02.008.

[53] I.M. Daniel, S. Wooh, and J. Lee, Defect and damage characterization in composite materials, in Review of Progress in Quantitative Nondestructive Evaluation. 1987, Springer. p. 1195-1202.

[54] C. Andrade, et al., The Use of Electrical Resistivity as NDT Method for the Specification of the durability of Reinforced Concrete. Centro de Seguridad y Durabilidad Estructural y de Materiales, Toulouse, 2009.

[55] Y. Yang, et al., An improved direct stiffness calculation method for damage detection of beam structures. Structural Control and Health Monitoring, 2013. 20(5): p. 835-851.

[56] J.D. Achenbach, Structural health monitoring–What is the prescription? Mechanics Research Communications, 2009. 36(2): p. 137-142.

[57] A.L. Wu, J.N. Yang, and C.H. Loh, A finite-element based damage detection technique for nonlinear reinforced concrete structures. Structural Control and Health Monitoring, 2015. 22(10): p. 1223-1239.

[58] J.L. Davis and A.P. ANNAN, Ground-penetrating radar for high-resolution

mapping of soil and rock stratigraphy 1. Geophysical prospecting, 1989. 37(5): p. 531-551.

[59] P. Swanson and J. Rettkowski, Damage Delineation in Structures Using Laser Vibrometry And Remote Excitation, N.I.o.O.S.a. Health, Editor. 2004, Spokane Research Laboratory: 315E. Montgomery Ave. Spokane, WA 99207, USA.

[60] T. Sugimoto, et al., Non-Contact Acoustic Inspection Method using Air-borne sound for Concrete Structures, in 11th European Conference on Non-Destructive Testing (ECNDT 2014). 2014: Prague, Czech Republic.

[61] S. Mustapha, et al., Assessment of debonding in sandwich CF/EP composite beams using A0 Lamb wave at low frequency. Composite structures, 2011. 93(2): p. 483-491.

[62] T. Yu, et al., Remote defect detection of FRP-bonded concrete system using acoustic-laser and imaging radar techniques. Construction and Building Materials, 2016. 109: p. 146-155.

[63] A. Smirnov, N.V. Ababkov, and A. Glinka, The Estimation of Long-Range Internal Stress Fields by Spectral-Acoustic Method. Advanced Materials Research, 2014. 1013: p. 121-126. DOI: 10.4028/www.scientific.net/AMR.1013.121.

[64] Z. Li, et al., Internal Stress Monitoring of In-Service Structural Steel Members with Ultrasonic Method. Materials, 2016. 9(4): p. 223.

[65] H.D. Ilkhechi and M.H. Samimi, Applications of the Acoustic Method in Partial Discharge Measurement: A Review. IEEE Transactions on Dielectrics and Electrical Insulation, 2021. 28(1): p. 42-51. DOI: 10.1109/TDEI.2020.008985.

[66] V.T. Rathod, A Review of Acoustic Impedance Matching Techniques for Piezoelectric Sensors and Transducers. Sensors, 2020. 20(14): p. 4051.

[67] Nordson. Imaging Modes. 2021; Available from:

https://www.nordson.com/en/divisions/sonoscan/support/imaging-modes.

[68] T. D’orazio, et al., Automatic ultrasonic inspection for internal defect detection in composite materials. NDT & E International, 2008. 41(2): p. 145-154.

[69] C. Özdemir, et al., A Review on Migration Methods in B-Scan Ground Penetrating Radar Imaging. Mathematical Problems in Engineering, 2014. 2014(1): p. 280738. DOI: https://doi.org/10.1155/2014/280738.

[70] B. Sheeba and P. Myvizhi, INDUSTRIAL APPLICATIONS OF A, B AND C SCAN MODE. International Journal of Pure and Applied Mathematics, 2018. 119(12): p. 3861-3872.

[71] A. Saini, et al., 3D ultrasonic imaging of surface-breaking cracks using a linear array. Ultrasonics, 2022. 125: p. 106790. DOI: https://doi.org/10.1016/j.ultras.2022.106790.

[72] W. Yao, Z. Li, and M. Qi, Damage process detection of a ceramic tile system by acoustic emission. Experimental mechanics, 2000. 40(3): p. 265-270.

[73] R. Mohammadkhani, et al., Improving Depth Resolution of Ultrasonic Phased Array Imaging to Inspect Aerospace Composite Structures. Sensors (Basel), 2020. 20(2). DOI: 10.3390/s20020559.

[74] B.M. Blandford and D.A. Jack, High resolution depth and area measurements of low velocity impact damage in carbon fiber laminates via an ultrasonic technique. Composites Part B: Engineering, 2020. 188. DOI: 10.1016/j.compositesb.2020.107843.

[75] J.S. Clausen and A. Knudsen. Nondestructive testing of bridge decks and tunnel linings using Impulse Response. in Proceedings of 10th ACI International Conference on Recent Advances in Concrete Technology, Seville, SP-261-19. 2009.

[76] R. Martini, et al., Advances on the use of non-destructive techniques for mechanical characterization of stone masonry: GPR and sonic tests. Procedia Structural Integrity, 2017. 5: p. 1108-1115.

[77] R. Dvořák and L. Topolář, Effect of Hammer Type on Generated Mechanical Signals in Impact-Echo Testing. Materials, 2021. 14(3): p. 606.

[78] S. Mary and J.C. Nicholas, Impact-Echo Method. Concrete International. 10(4).

[79] N.J. Carino. Impact echo: The fundamentals. in Proceedings of the International Symposium Non-Destructive Testing in Civil Engineering (NDT-CE), Berlin, Germany. 2015.

[80] K. Fujikake, B. Li, and S. Soeun, Impact response of reinforced concrete beam and its analytical evaluation. Journal of structural engineering, 2009. 135(8): p. 938-950.

[81] V. Meruane, et al., Damage Detection in Steel–Concrete Composite Structures by Impact Hammer Modal Testing and Experimental Validation. Sensors, 2022. 22(10): p. 3874.

[82] A. Shukla and J.-H. Koo. Detection of debonding in a tile-based thermal protection system via change in stiffness using continuation methods. in Health Monitoring and Smart Nondestructive Evaluation of Structural and Biological Systems V. 2006. International Society for Optics and Photonics.

[83] M. Saadatmorad, et al., Pearson Correlation and Discrete Wavelet Transform for Crack Identification in Steel Beams. Mathematics, 2022. 10(15): p. 2689.

[84] P. Castellini, M. Martarelli, and E.P. Tomasini, Laser Doppler Vibrometry: Development of advanced solutions answering to technology's needs. Mechanical Systems and Signal Processing, 2006. 20(6): p. 1265-1285. DOI: https://doi.org/10.1016/j.ymssp.2005.11.015.

[85] X. Xie, et al., A Stator Slot Wedge Loosening Offline Detection System Based on an Intelligent Maintenance Robot of a Large Hydro Generator. Machines, 2022. 10(8): p. 655.

[86] Y. He, et al., Laser ultrasonic imaging of submillimeter defect in a thick waveguide using entropy-polarized bilateral filtering and minimum variance beamforming. Mechanical Systems and Signal Processing, 2023. 186: p. 109863. DOI: https://doi.org/10.1016/j.ymssp.2022.109863.

[87] D.E. Chimenti, Review of air-coupled ultrasonic materials characterization. Ultrasonics, 2014. 54(7): p. 1804-1816. DOI: https://doi.org/10.1016/j.ultras.2014.02.006.

[88] L. Xie, et al., Optical methods of laser ultrasonic testing technology in the industrial and engineering applications: A review. Optics & Laser Technology, 2024. 176: p. 110876. DOI: https://doi.org/10.1016/j.optlastec.2024.110876.

[89] A. Zarei and S. Pilla, Laser ultrasonics for nondestructive testing of composite materials and structures: A review. Ultrasonics, 2024. 136: p. 107163. DOI: https://doi.org/10.1016/j.ultras.2023.107163.

[90] P. Liu, et al., Fatigue crack detection using dual laser induced nonlinear ultrasonic modulation. Optics and Lasers in Engineering, 2018. 110: p. 420-430. DOI: https://doi.org/10.1016/j.optlaseng.2018.05.025.

[91] Z. Zhou, et al., Application of laser ultrasonic technique for non-contact detection of structural surface-breaking cracks. Optics & Laser Technology, 2015. 73: p. 173-178. DOI: https://doi.org/10.1016/j.optlastec.2015.04.026.

[92] Z. Wan, et al., Laser ultrasonic detection for defects of LAM components based on variable time window intensity mapping with adaptive 2σ thresholds. Photoacoustics, 2024. 6(39). DOI: https://doi.org/10.1016/j.pacs.2024.100638.

[93]W Xu, et al., Utilization and advancement of laser ultrasound testing in assessment of aerospace composite characteristics: A review. Chinese Journal of Aeronautics, 2025.38(12). DOI: https://doi.org/10.1016/j.cja.2025.103789.

[94] B. Masserey, L. Aebi, and E. Mazza, Ultrasonic surface crack characterization on complex geometries using surface waves. Ultrasonics, 2006. 44: p. e957-e961. DOI: https://doi.org/10.1016/j.ultras.2006.05.059.

[95] F. Hernandez-Valle, B. Dutton, and R.S. Edwards, Laser ultrasonic characterisation of branched surface-breaking defects. NDT & E International, 2014. 68: p. 113-119. DOI: https://doi.org/10.1016/j.ndteint.2014.08.009.

[96] V. Zarubin, et al., A refraction-corrected tomographic algorithm for immersion laser-ultrasonic imaging of solids with piecewise linear surface profile. Applied Physics Letters, 2018. 112(21). DOI: https://doi.org/10.1063/1.5030586.

[97] C. Pei, et al., Fully noncontact measurement of inner cracks in thick specimen with fiber-phased-array laser ultrasonic technique. NDT & E International, 2020. 113: p. 102273. DOI: https://doi.org/10.1016/j.ndteint.2020.102273.

[98] K. Li, et al., Intelligent Evaluation of Crack detection with Laser Ultrasonic technique. IOP Conference Series: Earth and Environmental Science, 2020. 514(2): p. 022014. DOI: https://doi.org/10.1088/1755-1315/514/2/022014.

[99] E. Blomme, D. Bulcaen, and F. Declercq, Air-coupled ultrasonic NDE: experiments in the frequency range 750kHz–2MHz. NDT & E International, 2002. 35(7): p. 417-426. DOI: https://doi.org/10.1016/S0963-8695(02)00012-9.

[100] D.E. Chimenti and C.M. Fortunko, Characterization of composite prepreg with gas-coupled ultrasonics. Ultrasonics, 1994. 32(4): p. 261-264. DOI: https://doi.org/10.1016/0041-624X(94)90004-3.

[101] W.M.D. Wright and D.A. Hutchins, Air-coupled ultrasonic testing of metals using

broadband pulses in through-transmission. Ultrasonics, 1999. 37(1): p. 19-22. DOI: https://doi.org/10.1016/S0041-624X(98)00034-1.

[102] G. Waag, L. Hoff, and P. Norli, Air-coupled ultrasonic through-transmission thickness measurements of steel plates. Ultrasonics, 2015. 56: p. 332-339. DOI: https://doi.org/10.1016/j.ultras.2014.08.021.

[103] T.H. Gan, et al., High-resolution, air-coupled ultrasonic imaging of thin materials. IEEE Transactions on Ultrasonics, Ferroelectrics, and Frequency Control, 2003. 50(11): p. 1516-1524. DOI: https://doi.org/10.1109/TUFFC.2003.1251135.

[104] R. Stoessel, et al., Air-coupled ultrasound inspection of various materials. Ultrasonics, 2002. 40(1): p. 159-163. DOI: https://doi.org/10.1016/S0041-624X(02)00130-0.

[105] A. Römmeler, et al., Air coupled ultrasonic inspection with Lamb waves in plates showing mode conversion. Ultrasonics, 2020. 100: p. 105984. DOI: https://doi.org/10.1016/j.ultras.2019.105984.

[106] R. Kažys, et al., Air-coupled ultrasonic investigation of multi-layered composite materials. Ultrasonics, 2006. 44: p. e819-e822. DOI: https://doi.org/10.1016/j.ultras.2006.05.112.

[107] B. Han, et al., A generic time-frequency analysis-based signal processing and imaging approach for air-coupled ultrasonic testing. NDT & E International, 2024. 144: p. 103101. DOI: https://doi.org/10.1016/j.ndteint.2024.103101.

[108] H. Mortada, et al., Noncontact nondestructive ultrasonic techniques for manufacturing defects monitoring in composites: a review. Structural Health Monitoring, 2024. 23(3): p. 1969-1997. DOI: https://doi.org/10.1177/14759217231184589.

[109] K. Ng, I. Ghafoor, and P. Tse, A novel laser-based duffing oscillator system to

identify weak ultrasonic guided wave signals related to rail defects. Optics and Lasers in Engineering, 2022. 157: p. 107111. DOI: https://doi.org/10.1016/j.optlaseng.2022.107111.

[110] M.K. Yücel, et al. Pulse-compression based iterative time-of-flight extraction of dispersed Ultrasonic Guided Waves. in 2015 IEEE 13th International Conference on Industrial Informatics (INDIN). 2015. DOI: https: //doi.org/10.1109/INDIN.2015.7281840.

[111] J. Goossens, et al., Surface acoustic wave depth profiling of a functionally graded material. Journal of Applied Physics, 2007. 102(5).

[112] B. Yilmaz, et al., Air-Coupled, Contact, and Immersion Ultrasonic Non-Destructive Testing: Comparison for Bonding Quality Evaluation. Applied Sciences, 2020. 10(19): p. 6757.

[113] K. Luo, et al., Rapid damage reconstruction imaging of composite plates using non-contact air-coupled Lamb waves. NDT & E International, 2024. 143: p. 103047. DOI: https://doi.org/10.1016/j.ndteint.2024.103047.

[114] X. Jiang, et al., Defect Detection in Solid Timber Panels Using Air-Coupled Ultrasonic Imaging Techniques. Applied Sciences, 2024. 14(1): p. 434.

[115] T. Sugimoto, et al., High-speed noncontact acoustic inspection method for civil engineering structure using multitone burst wave. Japanese Journal of Applied Physics, 2017. 56(7S1): p. 07JC10.

[116] K. Katakura, et al., Study on detectable size and depth of defects in noncontact acoustic inspection method. Japanese Journal of Applied Physics, 2014. 53(7S): p. 07KC15. DOI: https://doi.org/10.7567/JJAP.53.07KC15.

[117] T. Sugimoto, et al. Efficiency Improvement of Outer Wall Inspection by Noncontact Acoustic Inspection Method using Sound Source Mounted Type

UAV. in 2019 IEEE International Ultrasonics Symposium (IUS). 2019. IEEE.

[118] T. Sugimoto, et al. Outer wall inspection using acoustic irradiation induced vibration from UAV for noncontact acoustic inspection method. in 2018 IEEE International Ultrasonics Symposium (IUS). 2018. IEEE.

[119] T. Sugimoto, et al., Study on movement measurement for internal defects in concrete structures by noncontact acoustic inspection method using correlation processing. Japanese Journal of Applied Physics, 2024. 63(4): p. 04SP45. DOI: https://doi.org/10.35848/1347-4065/ad3476.

[120] Y. Nakagawa, et al., Research on improvement of defect detection accuracy by resonance judgment for noncontact acoustic inspection method by acoustic irradiation-induced vibration. Japanese Journal of Applied Physics, 2022. 61(SG): p. SG1035. DOI: https://doi.org/10.35848/1347-4065/ac51bd.

[121] R. Akamatsu, et al., Proposal of non contact inspection method for concrete structures using high-power directional sound source and scanning laser doppler vibrometer. Japanese Journal of Applied Physics, 2013. 52(7S): p. 07HC12.

[122] Y. Zhao, Y. Chen, and L. Ye, A non-contact inspection method of tile debonding using tuned acoustic wave and laser doppler vibrometer. Journal of Sound and Vibration, 2023. 564: p. 117875. DOI: https://doi.org/10.1016/j.jsv.2023.117875.

[123] A. Niccolai, et al., Machine Learning-Based Detection Technique for NDT in Industrial Manufacturing. Mathematics, 2021. 9(11): p. 1251.

[124] G. D’Angelo and F. Palmieri, Knowledge elicitation based on genetic programming for non destructive testing of critical aerospace systems. Future Generation Computer Systems, 2020. 102: p. 633-642. DOI: https://doi.org/10.1016/j.future.2019.09.007.

[125] H. Sun, et al., Development of frequency-mixed point-focusing shear horizontal guided-wave EMAT for defect inspection using deep neural network. IEEE Transactions on Instrumentation and Measurement, 2020. 70: p. 1-14.

[126] J. Ye, S. Ito, and N. Toyama, Computerized ultrasonic imaging inspection: From shallow to deep learning. Sensors, 2018. 18(11): p. 3820.

[127] R. Qaddoura, et al., A Multi-Layer Classification Approach for Intrusion Detection in IoT Networks Based on Deep Learning. Sensors, 2021. 21(9): p. 2987.

[128] J. Yang and J. Ma, Feed-forward neural network training using sparse representation. Expert Systems with Applications, 2019. 116: p. 255-264. DOI: https://doi.org/10.1016/j.eswa.2018.08.038.

[129] E.L. van den Brandhof, et al., Chapter Two - Machine learning basic concepts for the movement disorders specialist, in International Review of Movement Disorders, A. Sánchez Ferro and M.H.G. Monje, Editors. 2023, Academic Press. p. 21-47. DOI: https://doi.org/10.1016/bs.irmvd.2023.04.004.

[130] M. Kubat, An Introduction to Machine Learning. 2017: Springer International Publishing.

[131] S. Uhlig, et al., A review of synthetic and augmented training data for machine learning in ultrasonic non-destructive evaluation. Ultrasonics, 2023. 134: p. 107041. DOI: https://doi.org/10.1016/j.ultras.2023.107041.

[132] I. Virkkunen, et al., Augmented Ultrasonic Data for Machine Learning. Journal of Nondestructive Evaluation, 2021. 40(1): p. 4. DOI: https://doi.org/10.1007/s10921-020-00739-5.

[133] J. Rhim and S.W. Lee, A neural network approach for damage detection and identification of structures. Computational Mechanics, 1995. 16(6): p. 437-443.

DOI: https://doi.org/10.1007/BF00370565.

[134] A.R. Baker and C.G. Windsor, The classification of defects from ultrasonic data using neural networks: The Hopfield method. NDT International, 1989. 22(2): p. 97-105. DOI: https://doi.org/10.1016/0308-9126(89)90862-6.

[135] F.W. Margrave, et al., The use of neural networks in ultrasonic flaw detection. Measurement, 1999. 25(2): p. 143-154. DOI: https://doi.org/10.1016/S0263-2241(98)00075-X.

[136] K. Hornik, Approximation capabilities of multilayer feedforward networks. Neural Networks, 1991. 4(2): p. 251-257. DOI: https://doi.org/10.1016/0893-6080(91)90009-T.

[137] K. Hornik, M. Stinchcombe, and H. White, Multilayer feedforward networks are universal approximators. Neural Networks, 1989. 2(5): p. 359-366. DOI: https://doi.org/10.1016/0893-6080(89)90020-8.

[138] B.J. Wolf and S.M. van Netten, 7.08 - Biophysics of the Lateral Line and Applications, in The Senses: A Comprehensive Reference (Second Edition), B. Fritzsch, Editor. 2020, Elsevier: Oxford. p. 116-132. DOI: https://doi.org/10.1016/B978-0-12-809324-5.24163-1.

[139] G. Harman and S. Kulkarni, Statistical Learning Theory as a Framework for the Philosophy of Induction, in Philosophy of Statistics, P.S. Bandyopadhyay and M.R. Forster, Editors. 2011, North-Holland: Amsterdam. p. 833-847. DOI: https://doi.org/10.1016/B978-0-444-51862-0.50027-7.

[140] J.F. Chen, Q.H. Do, and H.N. Hsieh, Training artificial neural networks by a hybrid PSO-CS Algorithm. Algorithms, 2015. 8(2): p. 292-308. DOI: https://doi.org/10.3390/a8020292.

[141] A.A. Heidari, et al., Ant Lion Optimizer: Theory, Literature Review, and

Application in Multi-layer Perceptron Neural Networks, in Nature-Inspired Optimizers: Theories, Literature Reviews and Applications, S. Mirjalili, J. Song Dong, and A. Lewis, Editors. 2020, Springer International Publishing: Cham. p. 23-46. DOI: https://doi.org/v10.1007/978-3-030-12127-3_3.

[142] Y.S. Park and S. Lek, Chapter 7 - Artificial Neural Networks: Multilayer Perceptron for Ecological Modeling, in Developments in Environmental Modelling, S.E. Jørgensen, Editor. 2016, Elsevier. p. 123-140. DOI: https://doi.org/10.1016/B978-0-444-63623-2.00007-4.

[143] K.Y. Chan, et al., Deep neural networks in the cloud: Review, applications, challenges and research directions. Neurocomputing, 2023. 545: p. 126327. DOI: https://doi.org/10.1016/j.neucom.2023.126327.

[144] S. Mouloodi, et al., Feedforward backpropagation artificial neural networks for predicting mechanical responses in complex nonlinear structures: A study on a long bone. Journal of the Mechanical Behavior of Biomedical Materials, 2022. 128: p. 105079. DOI: https://doi.org/10.1016/j.jmbbm.2022.105079.

[145] J. Cervantes, et al., A comprehensive survey on support vector machine classification: Applications, challenges and trends. Neurocomputing, 2020. 408: p. 189-215. DOI: https://doi.org/10.1016/j.neucom.2019.10.118.

[146] E. Tong, et al., Application of machine learning in modeling the quality of acoustic environments: A review. Environmental Modelling & Software, 2025. 193: p. 106658. DOI: https://doi.org/10.1016/j.envsoft.2025.106658.

[147] F. Al Thobiani, et al., A hybrid PSO and Grey Wolf Optimization algorithm for static and dynamic crack identification. Theoretical and Applied Fracture Mechanics, 2022. 118: p. 103213. DOI: https://doi.org/10.1016/j.tafmec.2021.103213.

[148] L.V. Ho, et al., An efficient stochastic-based coupled model for damage identification in plate structures. Engineering Failure Analysis, 2022. 131: p. 105866. DOI: https://doi.org/10.1016/j.engfailanal.2021.105866.

[149] S. Czarnecki, Non-destructive Evaluation of the Bond Between a Concrete Added Repair Layer with Variable Thickness and a Substrate Layer Using ANN. Procedia Engineering, 2017. 172: p. 194-201. DOI: https://doi.org/10.1016/j.proeng.2017.02.049.

[150] M. Bonagura and L. Nobile, Artificial Neural Network (ANN) Approach for Predicting Concrete Compressive Strength by SonReb. SDHM Structural Durability and Health Monitoring, 2021. 15(2): p. 125-137. DOI: https://doi.org/10.32604/sdhm.2021.015644.

[151] H.-L. Minh, et al., A new metaheuristic optimization based on K-means clustering algorithm and its application to structural damage identification. Knowledge-Based Systems, 2022. 251: p. 109189. DOI: https://doi.org/10.1016/j.knosys.2022.109189.

[152] B. Barros, et al., Design and testing of a decision tree algorithm for early failure detection in steel truss bridges. Engineering Structures, 2023. 289: p. 116243. DOI: https://doi.org/10.1016/j.engstruct.2023.116243.

[153] N. Prakash, et al., Learning defects from aircraft NDT data. NDT & E International, 2023. 138: p. 102885. DOI: https://doi.org/10.1016/j.ndteint.2023.102885.

[154] T. Tao and Z. Li, A review of deep learning application in transmission line defect detection. Electric Power Systems Research, 2026. 250: p. 112193. DOI: https://doi.org/10.1016/j.epsr.2025.112193.

[155] A. Ayman, et al., Feature learning for bearing prognostics: A comprehensive

review of machine/deep learning methods, challenges, and opportunities. Measurement, 2025. 245: p. 116589. DOI: https://doi.org/10.1016/j.measurement.2024.116589.

[156] G.E. Hinton, S. Osindero, and Y.-W. Teh, A Fast Learning Algorithm for Deep Belief Nets. Neural Computation, 2006. 18(7): p. 1527-1554. DOI: 10.1162/neco.2006.18.7.1527.

[157] R. Girshick, et al. Rich Feature Hierarchies for Accurate Object Detection and Semantic Segmentation. in 2014 IEEE Conference on Computer Vision and Pattern Recognition. 2014. DOI: https://doi.org/10.1109/CVPR.2014.81.

[158] M. Cai, et al., Deep Learning-Based Defect Identification in Hydraulic Structures: A Comprehensive Review. KSCE Journal of Civil Engineering, 2025: p. 100410. DOI: https://doi.org/10.1016/j.kscej.2025.100410.

[159] P. Sharma, S. Agarwal, and S.K. Sawhney, Performance - Based measures of physical function in young male adults: An association with body mass index. Indian Journal of Public Health Research and Development, 2017. 8(3): p. 310-316. DOI: https://doi.org/10.5958/0976-5506.2017.00206.6.

[160] S. Cong and Y. Zhou, A review of convolutional neural network architectures and their optimizations. Artificial Intelligence Review, 2023. 56(3): p. 1905-1969. DOI: https://doi.org/10.1007/s10462-022-10213-5.

[161] J. Gu, et al., Recent advances in convolutional neural networks. Pattern Recognition, 2018. 77: p. 354-377. DOI: https://doi.org/10.1016/j.patcog.2017.10.013.

[162] K. He, et al., Spatial Pyramid Pooling in Deep Convolutional Networks for Visual Recognition. IEEE Transactions on Pattern Analysis and Machine Intelligence, 2015. 37(9): p. 1904-1916. DOI: https://doi.org/10.1109/TPAMI.2015.2389824.

[163] L. Alzubaidi, et al., Review of deep learning: concepts, CNN architectures, challenges, applications, future directions. Journal of Big Data, 2021. 8(1): p. 53. DOI: https://doi.org/10.1186/s40537-021-00444-8.

[164] D.H. Hubel and T.N. Wiesel, Receptive fields, binocular interaction and functional architecture in the cat's visual cortex. The Journal of Physiology, 1962. 160(1): p. 106-154. DOI: https://doi.org/10.1113/jphysiol.1962.sp006837.

[165] B. Zada and R. Ullah, Pashto isolated digits recognition using deep convolutional neural network. Heliyon, 2020. 6(2). DOI: https://doi.org/10.1016/j.heliyon.2020.e03372.

[166] S. Yuan, L. Wang, and G. Peng, Neural network method based on a new damage signature for structural health monitoring. Thin-Walled Structures, 2005. 43(4): p. 553-563.

[167] D.U. Sung, et al., Impact Monitoring of Smart Composite Laminates Using Neural Network and Wavelet Analysis. Journal of Intelligent Material Systems and Structures, 2000. 11: p. 180 - 190.

[168] S. Sikdar, D. Liu, and A. Kundu, Acoustic emission data based deep learning approach for classification and detection of damage-sources in a composite panel. Composites Part B: Engineering, 2022. 228: p. 109450. DOI: https://doi.org/10.1016/j.compositesb.2021.109450.

[169] X. Ma, et al., Acoustic Emission Based Fault Detection of Substation Power Transformer. Applied Sciences, 2022. 12(5): p. 2759.

[170] R. Wang, et al., A Non-Contact Fault Diagnosis Method for Rolling Bearings Based on Acoustic Imaging and Convolutional Neural Networks. IEEE Access, 2020. 8: p. 132761-132774. DOI: 10.1109/ACCESS.2020.3010272.

[171] I. Ghafoor, et al., Non-contact detection of railhead defects and their classification

by using convolutional neural network. Optik, 2022. 253: p. 168607. DOI: https://doi.org/10.1016/j.ijleo.2022.168607.

[172] H. Herold and W. Burghausen. Modification of ceramic tile adhesive with redispersible polymer powders. in World congress on ceramic tile quality. 1998.

[173] L. Roman, et al. The influence of grout thickness on the adherence of ceramic tiling systems. in Proceedings of the 6th World Congress on Cerami Tile Quality. 2000. QUALICER Castellón.

[174] S.W. Smith, et al., The Scientist and Engineer's Guide to Digital Signal Processing By Steven W. Smith, Ph. D.

[175] J.W. Cooley and J.W. Tukey, An Algorithm for the Machine Calculation of Complex Fourier Series. Mathematics of Computation, 1965. 19(90): p. 297-301. DOI: https://doi.org/10.2307/2003354.

[176] P. Hale and S. and Macdonald, The Sydney Opera House: An Evolving Icon. Journal of Architectural Conservation, 2005. 11(2): p. 7-22. DOI: https://doi.org/10.1080/13556207.2005.10784942.

[177] A. Croker. Respecting the Vision: Sydney Opera House - a Conservation Management Plan. 2017 [cited 2023 7 August]; Available from: https://www.sydneyoperahouse.com/sites/default/files/collaborodam_assets/soh-cmp-interactive-1.pdf.

[178] G. Warburton, The vibration of rectangular plates. Proceedings of the Institution of Mechanical Engineers, 1954. 168(1): p. 371-384.

[179] A.W. Leissa, Vibration of plates. Vol. 160. 1969: Scientific and Technical Information Division, National Aeronautics and Space Administration, Washington DC.

[180] M. Long, 2 - Fundamentals of Acoustics, in Architectural Acoustics (Second

Edition), M. Long, Editor. 2014, Academic Press: Boston. p. 39-79. DOI: https://doi.org/10.1016/B978-0-12-398258-2.00002-7.

[181] J. De Clerck, Experimental Techniques, Rotating Machinery, and Acoustics, Volume 8: Proceedings of the 33rd IMAC, A Conference and Exposition on Structural Dynamics, 2015. 2015: Springer.

[182] L. Navarro, G. Courbebaisse, and M. Jourlin, Chapter Two - Logarithmic Wavelets, in Advances in Imaging and Electron Physics, P.W. Hawkes, Editor. 2014, Elsevier. p. 41-98. DOI: https://doi.org/10.1016/B978-0-12-800265-0.00002-3.

[183] A. Grossmann and J. Morlet, Decomposition of Hardy Functions into Square Integrable Wavelets of Constant Shape. SIAM Journal on Mathematical Analysis, 1984. 15(4): p. 723-736. DOI: https://doi.org/10.1137/0515056.

[184] L. Debnath, Wavelets and signal processing. 2003: Springer Science & Business Media.

[185] M. Duval-Destin, M.A. Muschietti, and B. Torresani, Continuous Wavelet Decompositions, Multiresolution, and Contrast Analysis. SIAM Journal on Mathematical Analysis, 1993. 24(3): p. 739-755. DOI: https://doi.org/10.1137/0524045.

[186] L. Liu and H. Hsu. Inversion and normalization of time-frequency transform. in 2011 International Conference on Multimedia Technology. 2011. DOI: https://doi.org/10.1109/ICMT.2011.6002490.

[187] J.M. Machado, et al., Automatic void content assessment of composite laminates using a machine-learning approach. Composite Structures, 2022. 288: p. 115383.

[188] W. Haoxiang and S. Smys. Overview of configuring adaptive activation functions for deep neural networks-a comparative study. in Journal of Ubiquitous

Computing and Communication Technologies (UCCT). 2021.

[189] N. Aloysius and M. Geetha. A review on deep convolutional neural networks. in 2017 international conference on communication and signal processing (ICCSP). 2017. IEEE.

[190] M. Lin, Q. Chen, and S. Yan, Network in network. arXiv preprint arXiv:1312.4400, 2013. DOI: https://doi.org/10.48550/arXiv.1312.4400.

[191] I.H. Association, Hydropower sector climate resilience guide. International Hydropower Association: London, UK, 2019.

[192] A. Wasti, et al., Climate change and the hydropower sector: A global review. Wiley Interdisciplinary Reviews: Climate Change, 2022. 13(2): p. e757.

[193] A. Wasti, et al., Climate change and the hydropower sector: A global review. WIREs Climate Change, 2022. 13(2): p. e757. DOI: https://doi.org/10.1002/wcc.757.

[194] A.P. Daga, et al., Vibration monitoring of a hydroelectric power generation unit: Improved indicators of rotor health based on orbital analysis. Mechanics & Industry, 2022. 23: p. 15.

[195] M. Pandey, et al., Mechanistic Model of an Air Cushion Surge Tank for Hydro Power Plants. Energies, 2022. 15(8): p. 2824.

[196] H. Tian, L. Yang, and P. Ji, Intelligent Analysis of Vibration Faults in Hydroelectric Generating Units Based on Empirical Mode Decomposition. Processes, 2023. 11(7): p. 2040.

[197] X. Liu, Y. Luo, and Z. Wang, A review on fatigue damage mechanism in hydro turbines. Renewable and Sustainable Energy Reviews, 2016. 54: p. 1-14. DOI: https://doi.org/10.1016/j.rser.2015.09.025.

[198] N. Dehlinger and G. Stone, Surface partial discharge in hydrogenerator stator

windings: Causes, symptoms, and remedies. IEEE Electrical Insulation Magazine, 2020. 36(3): p. 7-18. DOI: https://doi.org/10.1109/MEI.2020.9063559.

[199] X. Peng, et al., Laboratory Studies of a New Stator Slot Wedge Tester for HV Generators. IEEE Transactions on Energy Conversion, 2009. 24(1): p. 146-152. DOI: https://doi.org/10.1109/TEC.2008.2008881.

[200] S.P. Dahal, M. Dahal, and B. Silwal. Historical Data Based Monitoring of Hydro Generator Using Machine Learning. in 2022 14th International Conference on Software, Knowledge, Information Management and Applications (SKIMA). 2022. DOI: https://doi.org/10.1109/SKIMA57145.2022.10029567.

[201] M. Liese and M. Brown, Design-dependent slot discharge and vibration sparking on high voltage windings. IEEE transactions on Dielectrics and Electrical Insulation, 2008. 15(4): p. 927-932.

[202] K. Kumar and R.P. Saini, A review on operation and maintenance of hydropower plants. Sustainable Energy Technologies and Assessments, 2022. 49: p. 101704. DOI: https://doi.org/10.1016/j.seta.2021.101704.

[203] Y. Hao, et al., Application of ultrasonic pulse-echo method to insulation condition diagnosis for large generators. IEEE transactions on dielectrics and electrical insulation, 2005. 12(1): p. 104-113.

[204] M. Warren and C.I. Butterworth, A Preventive Maintenance Program for Hydroelectric Generator Windings. IEEE Transactions on Power Apparatus and Systems, 1968. PAS-87(5): p. 1283-1288. DOI: https://doi.org/10.1109/TPAS.1968.292219.

[205] A. Pistone, et al., Reconfigurable inspection robot for industrial applications. Procedia Manufacturing, 2019. 38: p. 597-604. DOI:

https://doi.org/10.1016/j.promfg.2020.01.075.

[206] B. Jeon, et al., Visual navigation system for generator stator wedge inspection mobile robot. Electronics Letters, 2022. 58(20): p. 756-758. DOI: https://doi.org/10.1049/ell2.12592.

[207] K. Ekkachai, et al., Development of the generator inspection vehicle and the inspection equipment. Journal of Field Robotics, 2022. 39(7): p. 1033-1053. DOI: https://doi.org/10.1002/rob.22086.

[208] C. Li, et al. Research on Air Gap Monitoring Technology of Hydro-Generator Based on Infrared Monocular Visual Image Analysis. in 2023 5th Asia Energy and Electrical Engineering Symposium (AEEES). 2023. DOI: https://doi.org/10.1109/AEEES56888.2023.10114318.

[209] S. Han, et al., In-Service Monitoring of Stator-Slot Magnetic Wedge Condition for Induction Motors. IEEE Transactions on Industry Applications, 2016. 52(4): p. 2900-2910. DOI: https://doi.org/10.1109/TIA.2016.2539128.

[210] C. Milinusic. The Inaudible World: Measuring Sounds Perceived by Non-Human Life. in Audio Engineering Society Convention 152. 2022. Audio Engineering Society.

[211] X. Xie, et al., Research on Non-destructive Intelligence Detection of Tightness of Stator Slot Wedges of Large Hydro-generator. 2023.

[212] G. Ranzi, O. Vallati, and I. Cashen. A Methodology for the Inspection and Monitoring of the Roof Tiles and Concrete Components of the Sydney Opera House. 2018. Cham: Springer International Publishing.

[213] J.H. Tong, T.T. Wu, and C.K. Lee, Fabrication of a Piezoelectric Impact Hammer and Its Application to the In-situ Nondestructive Evaluation of Concrete. Japanese Journal of Applied Physics, 2002. 41(11R): p. 6595. DOI:

https://doi.org/10.1143/JJAP.41.6595.

[214] Z. Pang, et al., A Novel Intelligent Rebound Hammer System Based on Internet of Things. Micromachines (Basel), 2023. 14(1). DOI: https://doi.org/10.3390/mi14010148.

[215] H.R. Kumavat, N. Chandak, and D. Jadhav. Experimental investigation on relationships between rebound index and compressive strength of cement concrete specimen influenced by physical factors. in 2020 Advances in Science and Engineering Technology International Conferences (ASET). 2020. DOI: https://doi.org/10.1109/ASET48392.2020.9118246.

[216] J. Eargle, Chapter 1 - A Short History of the Microphone, in The Microphone Book (Second Edition), J. Eargle, Editor. 2004, Focal Press: Oxford. p. 1-6. DOI: https://doi.org/10.1016/B978-0-240-51961-6.50005-5.

[217] A.J. Zuckerwar, Acoustical Measurement, in Encyclopedia of Physical Science and Technology (Third Edition), R.A. Meyers, Editor. 2003, Academic Press: New York. p. 91-115. DOI: https://doi.org/10.1016/B0-12-227410-5/00008-9.

[218] M.R. Mahmoudi, et al., On comparing and clustering the spectral densities of several almost cyclostationary processes. Alexandria Engineering Journal, 2020. 59(4): p. 2555-2565. DOI: https://doi.org/10.1016/j.aej.2020.03.043.

[219] D.S. Coates and P.J. Diggle, TESTS FOR COMPARING TWO ESTIMATED SPECTRAL DENSITIES. Journal of Time Series Analysis, 1986. 7(1): p. 7-20. DOI: https://doi.org/10.1111/j.1467-9892.1986.tb00482.x.

[220] C. Jentsch and M. Pauly, A note on using periodogram-based distances for comparing spectral densities. Statistics & Probability Letters, 2012. 82(1): p. 158-164. DOI: https://doi.org/10.1016/j.spl.2011.09.014.

[221] J. Timmer, et al., A test for a difference between spectral peak frequencies.

Computational Statistics & Data Analysis, 1999. 30(1): p. 45-55. DOI: https://doi.org/10.1016/S0167-9473(98)00106-6.

[222] J. Caiado, N. Crato, and D. Peña, A periodogram-based metric for time series classification. Computational Statistics and Data Analysis, 2006. 50(10): p. 2668-2684. DOI: https://doi.org/10.1016/j.csda.2005.04.012.

[223] P. De Souza and P.J. Thomson, LPC Distance Measures and Statistical Tests with Particular Reference to the Likelihood Ratio. IEEE Transactions on Acoustics, Speech, and Signal Processing, 1982. 30(2): p. 304-315. DOI: https://doi.org/10.1109/TASSP.1982.1163867.

[224] E.A. Maharaj, Clusters of time series. Journal of Classification, 2000. 17(2): p. 297-314. DOI: https://doi.org/10.1007/s003570000023.

[225] J. Semmlow, Chapter 10 - Stochastic, Nonstationary, and Nonlinear Systems and Signals, in Circuits, Signals and Systems for Bioengineers (Third Edition), J. Semmlow, Editor. 2018, Academic Press. p. 449-489. DOI: https://doi.org/10.1016/B978-0-12-809395-5.00010-2.

[226] G. Aggarwal, S.P. Gochhayat, and L. Singh, Chapter 10 - Parameterization techniques for automatic speech recognition system, in Machine Learning and the Internet of Medical Things in Healthcare, K.K. Singh, et al., Editors. 2021, Academic Press. p. 209-250. DOI: https://doi.org/10.1016/B978-0-12-821229-5.00010-0.

[227] E. Lai, 6 - Finite impulse response filter design, in Practical Digital Signal Processing, E. Lai, Editor. 2003, Newnes: Oxford. p. 98-144. DOI: https://doi.org/10.1016/B978-075065798-3/50006-0.

[228] A. Graps, An introduction to wavelets. IEEE Computational Science and Engineering, 1995. 2(2): p. 50-61. DOI: https://doi.org/10.1109/99.388960.

[229] B.K. Alsberg, A.M. Woodward, and D.B. Kell, An introduction to wavelet transforms for chemometricians: A time-frequency approach. Chemometrics and Intelligent Laboratory Systems, 1997. 37(2): p. 215-239. DOI: https://doi.org/10.1016/S0169-7439(97)00029-4.

[230] Z. Su and L. Ye, Digital Damage Fingerprints (DDF) and its application in quantitative damage identification. Composite Structures, 2005. 67(2): p. 197-204. DOI: https://doi.org/10.1016/j.compstruct.2004.09.033.

[231] Dong Wang, Lin Ye, and Ye Lu, A Probabilistic Diagnostic Algorithm for Identification of Multiple Notches Using Digital Damage Fingerprints (DDFs). Journal of Intelligent Material Systems and Structures, 2009. 20(12): p. 1439-1450. DOI: https://doi.org/10.1177/1045389X09338323.

[232] Z. Su and L. Ye, A fast damage locating approach using digital damage fingerprints extracted from Lambwave signals. Smart materials and structures, 2005. 14(5): p. 1047.

[233] R. Sun, D. Ma, and G. Pan, Post-training quantization for efficient ANN-SNN conversion. Neural Networks, 2025. 191: p. 107832. DOI: https://doi.org/10.1016/j.neunet.2025.107832.

[234] R.A. Cardoso, et al., ANN vs. theoretical models for predicting crack path in fretting fatigue. International Journal of Fatigue, 2025. 199: p. 109075. DOI: https://doi.org/10.1016/j.ijfatigue.2025.109075.

[235] T.K. Gupta and K. Raza, Chapter 7 - Optimization of ANN Architecture: A Review on Nature-Inspired Techniques, in Machine Learning in Bio-Signal Analysis and Diagnostic Imaging, N. Dey, et al., Editors. 2019, Academic Press. p. 159-182. DOI: https://doi.org/10.1016/B978-0-12-816086-2.00007-2.